Immunogenicity of gold nanoshell/silica core nanoplasmonics and photothermal induced-cell death

Hai T. Nguyen

A dissertation

submitted in partial fulfillment of the

requirements for the degree of

Doctor of Philosophy

University of Washington

2012

Reading Committee:

Hong Shen, (Chair)

Dan Schwartz

Buddy Ratner

Program Authorized to Offer Degree:

Chemical Engineering

University of Washington

Abstract

Immunogenicity of gold nanoshell/silica core nanoplasmonics and photothermal induced-cell death

Hai T. Nguyen

Chair of the Supervisory Committee:

Assistant Professor Hong Shen

Chemical Engineering

Cancer is one of the three leading causes of death in industrialized nations. Conventional therapies, including surgical removal, chemotherapy, and radiation provide increasingly effective methods for the treatment of various types of cancer. The invasiveness and side effects of these treatment methods can potentially be minimized with new thermal ablation therapies. Gold nanoshell enabled photothermal therapy is one thermal ablation strategy with promising initial evidence as a minimally invasive, simple, multifunctional treatment that can both detect and remove tumors efficiently, and have recently reached the clinical trial stage.

In this thesis, we characterize the intracellular damage that occurs during the photothermal ablation of cancer cells with varying treatment parameters, and model the corresponding localized temperature profiles to explain the thermal damage on a local level that occurs to proteins, DNA/RNA, and lipid membranes.

In addition, Immunological implications to nanoshell enabled photothermal therapy are addressed. Injection of nanoshells require circulation in the bloodstream and deposition in the tumor through the enhanced permeability and retention(EPR) effect. Nanoshells also accumulate in various organs where detection and processing by immune cells such as macrophages can lead to inflammation. Activation of the inflammasome complex, a signaling pathway in response to particulate sensing is assessed by the quantification of secreted proinflammatory cytokines.

Finally, immune responses associated with the sensing and clearance of dying cells following nanoshell enabled photothermal therapy are evaluated for determining the generation of an inflammatory environment in the tumor that would generate an anti-tumor immune response to enhance tumor regression and rechallenge.

TABLE OF CONTENTS

List of Figures

List of Tables

Acknowledgements

To begin, I would like to thank Hong Shen for providing me with the opportunity to pursue my studies under her guidance. The work was a constant challenge, and the ultimately rewarding outcome was achieved through perseverance on both our parts over the years. Her patience and direction kept me on course to finish this degree.

Many thanks also to the members who have served on my committee, Dave Castner, Buddy Ratner, Dan Schwartz, Hong Qian, and Larry Ricker.

I would also like to acknowledge the members of the Shen group, who have all provided me with assistance in one way or another throughout my years here, your contributions have been invaluable.

Lastly, my parent Sinh and Luong, and my sister Vy, who's love has kept me going, and their belief in me that got me here in the first place. Finally, all the friends I've met along the way for providing the support every graduate student needs to make it through a Ph.D.

A. Chapter 1: Introduction

Since the introduction of nanoshells, specifically nanoparticles consisting of silica core covered in a thin shell of gold, in 1998 by the Halas group[1], nanoshells have emerged as a quickly expanding research area with increasingly promising applications. The tunable optical properties of the nanoshells due to the geometry of the structure resulting in high plasmon resonances, which can be explained by Mie theory[2], make them a popular subject of interest in various research fields, both theoretical and experimental. By varying the core size to shell thickness ratio, the optical resonance of the nanoshell can be tuned from the visible to the infrared region(700-1100nm)[1], with the near infrared(NIR) region being the most frequently targeted region due to the optical transparency of tissue[3].

Gold nanoshells have a broad spectrum of applications due to their unique tunable plasmon resonance. The most well-known application of gold nanoshells is for use in laser induced photothermal therapy, particularly for targeting cancer cells due to their passive accumulation at vascularized tumors. Both *in vitro*[4-8] and *in vivo*[9-12] applications have been studied, and are often coupled with bioimaging[9, 13]. In addition, applications for enhanced fluorescence of nearby dye molecules[14], biosensing applications used for blood immunoassays[15], surface enhance raman spectroscopy(SERS)[16, 17] and infrared absorption(SEIRA) spectroscopy[16, 18].

Paper	Hirsch *et al* 2003[10]	O'Neal *et al* 2004[11]	Gobin *et al* 2007[9]	Zaman *et al* 2007[19]	Stern *et al* 2008[12]	Diagaradjane *et al* 2008[20]
Application	NEPTT	NEPTT	NEPTT & Imaging	Imaging	NEPTT	Mild Hyperthermia NEPTT
Mice Type	CB17-Prkd C SCID/J Mice	5-6 week female albino BALB/cAnNHsd mice 15-20g	BALBc mice	6-8 week Swiss athymic mice	6-8 week athymic mice	6-8 week swiss immunocompromised male nude mice 20-25g
Cell Innoculation Type	Canine TVT	CT-26 murine colon carcinoma	CT-26 murine colon carcinoma	rat C6-glioma	Human prostate PC-3	Human colorectal cancer HCT 116
Innoculation Volume	~0.25ml	50µl	25µl	Not stated	100µl	50µl
Cell Number	Unstated	$1.5X10^5$ cells	$1.5X10^5$ cells	$1x10^6$ cells/µl	$2x10^6$ cells	$2x10^6$ cells
Tumor Size At Treatment	~1cm	0.3-0.55cm	0.5cm	1cm	~40mm^3	0.7-0.8cm
Innoculation Location	SC Hind legs	SC right flank	SC right flank	SC right flank	SC right + left flank	SC right thigh
Tumor Growth Time	6 weeks	8-16 days	10 days	Not stated	Not stated	No stated
NS Quantity	20-50ul $1.5x10^{10}$ PEG NS/ml in PBS	100µl $2.4x10^{11}$ Peg NS/ml	150 µl $1.5x10^{11}$ PEG NS/ml in PBS	$8x10^8$ Peg NS/g body weight	7.0-8.5µl/g BW $3X10^9$ PEG NS/ml	$8x10^8$ Peg NS/g body weight
Injection Location	Intratumor 5mm	Tail Vein	Tail Vein	Tail Vein	Not stated	Tail Vein
NS tumor accumulation time	N/A	6 h	20 h	1 h, 24 h	18 h	20-24 h
Laser	820nm, 4W/cm^2, 5mm spot size	808nm 4W/cm^2, 5mm spot size	808nm 4W/cm^2, 5mm spot size	N/A	810nm 4W/cm^2	808 nm 0.5-1W/cm^2, 10mm spot size
Treatment Time	<6 min	3 min	3 min	N/A	3 min	20 min
Tumor Assessment	Immediately following treatment	>90 days	7 weeks	N/A	3 weeks	25 days
Treatment stop time	Euthanized immediately	Euthanized when tumor >10mm	Not stated	N/A	Not stated	Not stated

Table 1. Summary of *in vivo* nanoshell enabled photothermal therapy

Cancer is one of the three leading causes of death in industrialized nations. Cancer is the result of unchecked growth of malignant cells, therefore, curing cancer requires the removal of all

malignant cells without killing the individual. Conventional therapies, including surgical removal, chemotherapy, and radiation provide increasingly effective methods for the treatment of various types of cancer. The invasiveness and side effects of these treatment methods can potentially be minimized with new thermal ablation therapies. Gold nanoshell enabled photothermal therapy is one thermal ablation strategy with promising initial evidence as a minimally invasive, simple, multifunctional treatment that can both detect and remove tumors efficiently, and have recently reached the clinical trial stage. While *in vitro* and *in vivo* models have shown the ability to destroy tumor cells and induce tumor regression, a widely accepted, optimized treatment process has not been determined, and the process of cellular injury and resulting clearance of tumors is not well understood. A yet unproven theory proposed by various researchers for tumor regression must involve an immune response following treatment. In our work, we propose to determine the immunogenicity of the treatment from the start of injection, to clearance and regression of the tumor and the immune responses associated. A long term goal would consist of primary tumor regression and removal of metastases, accompanied by prevention of tumor recurrence through the generation of an anti-tumor adaptive immune response, using gold nanoshell enabled photothermal therapy.

A.1 Chapter Summary

Chapter 2: Synthesis and Characterization

The synthesis of gold nanoshells, consisting of a silica core coated with a thin gold shell, was first developed by Oldenburg and colleagues over a decade ago.[1] Tuning of the nanoshell surface plasmon resonance(SPR) into the NIR region which is most transparent to tissue is accomplished by controlling the core to shell ratio. Nanoshells optimized for photothermal therapy are sized in the 1-200nm diameter to utilize the enhanced permeability and retention(EPR) effect for passive accumulation at tumors due to the leaky vasculature in rapidly expanding tumors[10]. Passivation of nanoshells by PEGylation of the gold surface is often utilized to minimize immune interaction and increase circulation *in vivo*.[10, 21] Synthesized nanoshells will be characterized to determine complete shell formation, optimized NIR tuning(800nm), PEGylation, and efficient heating.

Chapter 3: *In vitro* cell responses to NEPTT

Efficacy of nanoshell enabled photothermal therapy is often assessed qualitatively with cell viability assays that do not provide specific information about cell death modalities. Relevant treatment parameters vary widely between studies with no optimized procedure published to date. Nanoshell dosing, laser fluence, and irradiation time are varied to modulate cell death efficacy and modality in a quantitative manner. Mechanisms of cellular injury leading to cell death are also considered. DNA degradation, membrane permeablization, and endocytic compartment disruption are implicated as possible heat induced damages resulting in cell death through necrosis or apoptosis.

Chapter 4: Intracellular temperature modeling

A number of studies have used gold nanoshells for photothermal destruction of cancer cells through the utilization of near infrared(NIR) lasers. Nanoshells can by internalized by the cell, and trafficked to various areas throughout the cytosol. The light energy is converted to heat leading to thermal injury of a number of intracellular components including membrane permeabilization, protein denaturation, and DNA/RNA damage.

Currently, no experimental approaches are available to measure temperature profiles during nanoshell enabled photothermal therapy(NEPTT) with subcellular resolution. Nanoshell heating has been analyzed on the nanoscale for individual particles, and on the macroscopic scale for whole tumor heating, while intracellular heating has been largely unexplored. Very few numerical simulations on the heat transfer process have been performed on a subcellular level for any nanoparticle systems, with no work having been performed on a nanoshell system.

Chapter 5: *In vitro* inflammatory response

Newly recognized inflammasome complexes involved in immune response to cell death provide a promising innate immune system stimulators. The NALP3 inflammasome has been implicated in activation and processing of pro-IL-1β into its active secreted in response to cellular injury signals from specific cell death modalities in macrophages primed with LPS[22]. Activation the NALP3 inflammasome in dendritic cells has been shown to be required for priming of CD8+ T cells. Macrophages will be exposed to dying tumor cells to determine inflammasome activation and secretion of IL-1β with the dying cells screened for various damage associated molecular patterns(DAMPs) generated following nanoshell enabled photothermal therapy. Dendritic cell maturation will also be assessed with the dying tumor cell constituents.

Chapter 6: Inflammatory response to Nanoshell accumulation

Gold nanoshells are particles consisting of a silica core coated in a thin gold shell used for the photothermal ablation of tumors and are currently in clinical trials. The benefit of using a nanoparticle system consisting of a silica core and gold shell layer is the relative biocompatibility of the two materials and lack of toxicity in clinical use. Nanoshell accumulation in tumors relies on the enhance permeability and retention(EPR) effect in which circulating nanoparticles extravasate into tumors due to the leaky nature of the vasculature within the rapidly expanding tumor mass. Circulating nanoparticles also accumulate in other areas as well, such as the liver, kidneys, spleen, and lungs.

Particulate sensing by the immune system occurs in phagocytic cells such as macrophages, and has been shown to require the activation of the NALP3 inflammasome complex. Inflammasome activation in macrophages by gold nanoshells will be assessed, and the mechanism associated with the complex formation will be elucidated.

B. Chapter 2: Synthesis and Characterization

B.1 Background

Fabrication of gold nanoshells was originally developed and described by Oldenburg et al[1], and involves a multi step process for shell formation. Briefly, monodisperse silica nanoparticles made using the stober method[23] are functionalized with an aminosilane, followed by attachment of 1-2nm colloidal gold particles prepared using a method developed by Duff et al.[24]. A solution of chloroauric acid($HAuCl_4$) is reduced onto the gold dressed particles, which lead to growth and coalescence into an apparently complete gold shell.

Reduction of chloroauric acid onto the gold seeded silica particles is one of the most important steps in the nanoshell formation process, and is also the step that leads to the most defects appearing on the nanoparticles as the gold islands grow and coalesce into a shell. Until recently, reduction was carried out with aqueous phase reducing agents, most notably formaldehyde(H_2CO)[21, 25, 26] and sodium borohydride($NaBH_4$)[1, 27], and relied on solution mixing to quickly distribute the reducing agent, with no discernible difference between the two reducing agents in terms of shell formation. When using these reducing agents, aging of the precursor reagents seem to effect shell formation, leaving small windows of time for optimized nanoshell formation[25]. A new gas phase reducing agent, carbon monoxide(CO), has recently been shown to form nanoshells more consistently than aqueous phase reducing agents, without the time dependence on reagents. In addition, the gold shells made using CO were thinner and more uniform compared to those prepared using H_2CO[25]. More importantly, use of a gas phase reducing agent which can be bubbled into the reducing solution does not rely on mechanical mixing for distribution, and has the potential to move from a batch process to a continuous reaction with an appropriately designed reactor.

PEGylation has many attractive qualities common through all colloidal drug delivery systems (CDDS). The first and foremost reason for the use of PEGylation is its ability to lengthen the circulation time of CCDS so as to have enough time to reach the therapeutic target. PEGylation allows for a way to effectively avoid uptake by cells of the Reticulo-endothelial system (RES)[28, 29]. PEG is also often chosen because it is uncharged, hydrophilic, non-immunogenic and can easily be grafted. Through the use of a PEG coating, a decrease in the apparent charge is evident on all CCDS, which ensures efficient stabilization.[30] Pegylation, due to the brushlike structure on the surface will increase colloidal stabilization, decrease protein adsorption, and increased circulation times for injected nanoshells used *in vivo*.

B.2 Research Design and Methods

Nanoshell Synthesis

The method employed to synthesize the gold nanoshell/silica core particles was adapted based on that described by Pham et al.[21] and Brinson et al [25].

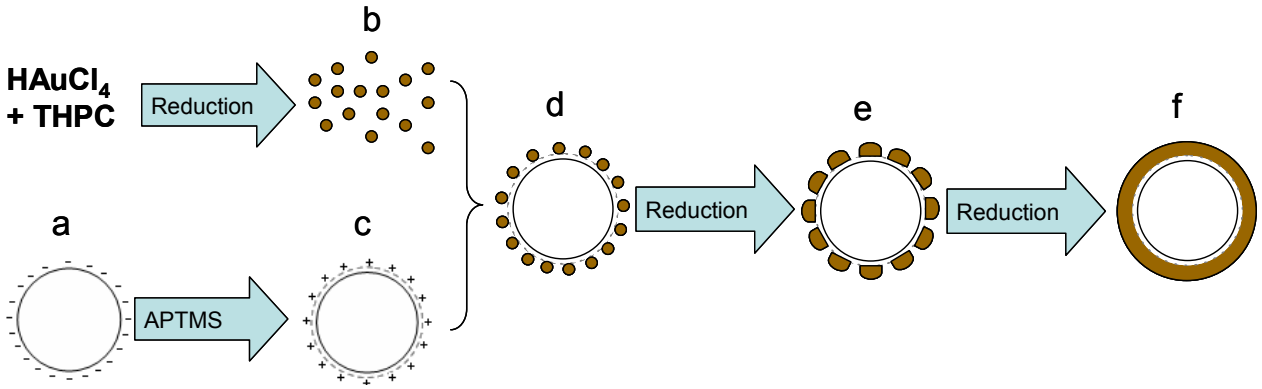

Scheme 1. Stepwise fabrication of silica core gold nanoshells. a) Bare negatively charged silica nanoparticles. b) 2-3nm negatively charged colloidal gold nanoparticles. c) APTMS treated silica with positive surface charge. d) electrostatic attachment of negatively charged colloidal gold to positively charged silica core particles. e) AuCl4- gold ion reduction on gold islands on silica particle surface. f) eventual coalescence of gold islands into silica core nanoshell particles

In brief, silica cores with a mean diameter of 110 nm were prepared using the Stober process[23]. 1.5ml Tetraethyl orthosilicate(TEOS) was added dropwise to a 50ml ethanol solution containing 3.2ml 70% ammonia resulting in condensation reactions self nucleating into monodisperse particles. They were subsequently functionalized with 25 µl (3-Aminopropyl)trimethoxysilane (APTMS) overnight followed by gentle boiling for one hour to enhance attachment. The particles were washed 3 times by centrifugation, and redispersed in 50ml of absolute ethanol. 2-3 nm colloidal gold particles were prepared using a method originally described by Duff et al. [24] 2ml 1% gold chloride solution was added to a 45ml solution of water containing 0.5ml NaOH and 12 µl of the the reducing agent tetrakis(hydroxymethyl)phosphonium chloride(THPC), and quickly reacted to form the colloidal gold particles indicated by the development of a dark reddish brown hue. The synthesized colloidal gold particles were attached to the surface of the silica nanoparticles through electrostatic interactions by adding 0.5ml of the

functionalized silica particles to 4ml of excess colloidal gold solution followed by purification through centrifugation and wash cycles before being redispersed in 5ml Milli-Q deionized water. The colloidal gold on the surface acted as nucleation sites for further reduction of gold ions onto silica core.

The nanoshell reducing solution was prepared by adding 25mg of potassium carbonate to 100ml of Milli-Q deionized water. After 10 mins of stirring 1.5ml of 1% gold chloride solution was added to the reduction solution. The solution was then aged overnight under refrigeration prior to use. The nanoshells formed were concentrated through centrifugation and redispersed in Milli-Q deionized water prior to use. Gaseous carbon monoxide, the reducing agent was bubbled at 25ml/min into a mixture of 4ml of the gold reducing solution and between 100-200 µl of the colloidal gold coated silica particles. The completion of the gold reduction was indicated by the development of blue shade in the reaction mixture.

The bare and gold nanoshell-coated silica cores were evaluated by scanning electron microscopy (SEM) (JOEL 7200 SEM) and UV-Vis spectroscopy (Molecular Devices Spectramax M5). The particle size was calculated based on SEM images. Extent of nanoshell formation and optimization of the nanoshell reduction conditions was based on absorbance spectra and SEM imaging. The absorbance spectra peak was tuned to 800nm by adjusting the amount of colloidal gold coated silica particles added to the reducing solution. The size distribution and aggregation of nanoshells were examined by the dynamic light scattering.

The silica particle concentration was calculated based on the average volume of each individual silica particle and the total silica volume for a given amount of TEOS. The molecular weight and density of the silica particles was assumed to be similar to bulk values. Gold nanoshell/silica core nanoparticle concentration was estimated based on silica particle quantity

assuming no loss of silica particles during the growth of gold nanoshells. For the convenience, the term, Au nanoshells, was used in the text to represent gold nanoshell/silica core nanoparticles.

Polyethelene Glycol Nanoshell Conjugation

Polyethelene glycol-thiol(PEG-SH) was conjugated to the gold surface of the nanoshells

5000mw PEG-SH(Sigma) was conjugated to synthesized gold nanoshells by mixing PEG-SH at concentrations from 1-10μM with aliquots of ~$1x10^9$ nanoshells/ml. The samples are mixed at room temperature and incubated for 1 hour. Excess PEG-SH is removed by 3 centrifugation and wash steps followed by redispersal in Milli-Q water. Pegylation will be characterized by zeta potential and hydrodynamic diameter using DLS(Zetasizer, Malvern Instruments ZS90).

B.3 Results

We have been able to successfully develop a method to prepare silica core gold nanoshells based on modifications to methods based on work by Pham et al[21]. To confirm the extent of nanoshell formation, imaging of the particles using scanning electron microscopy was performed.

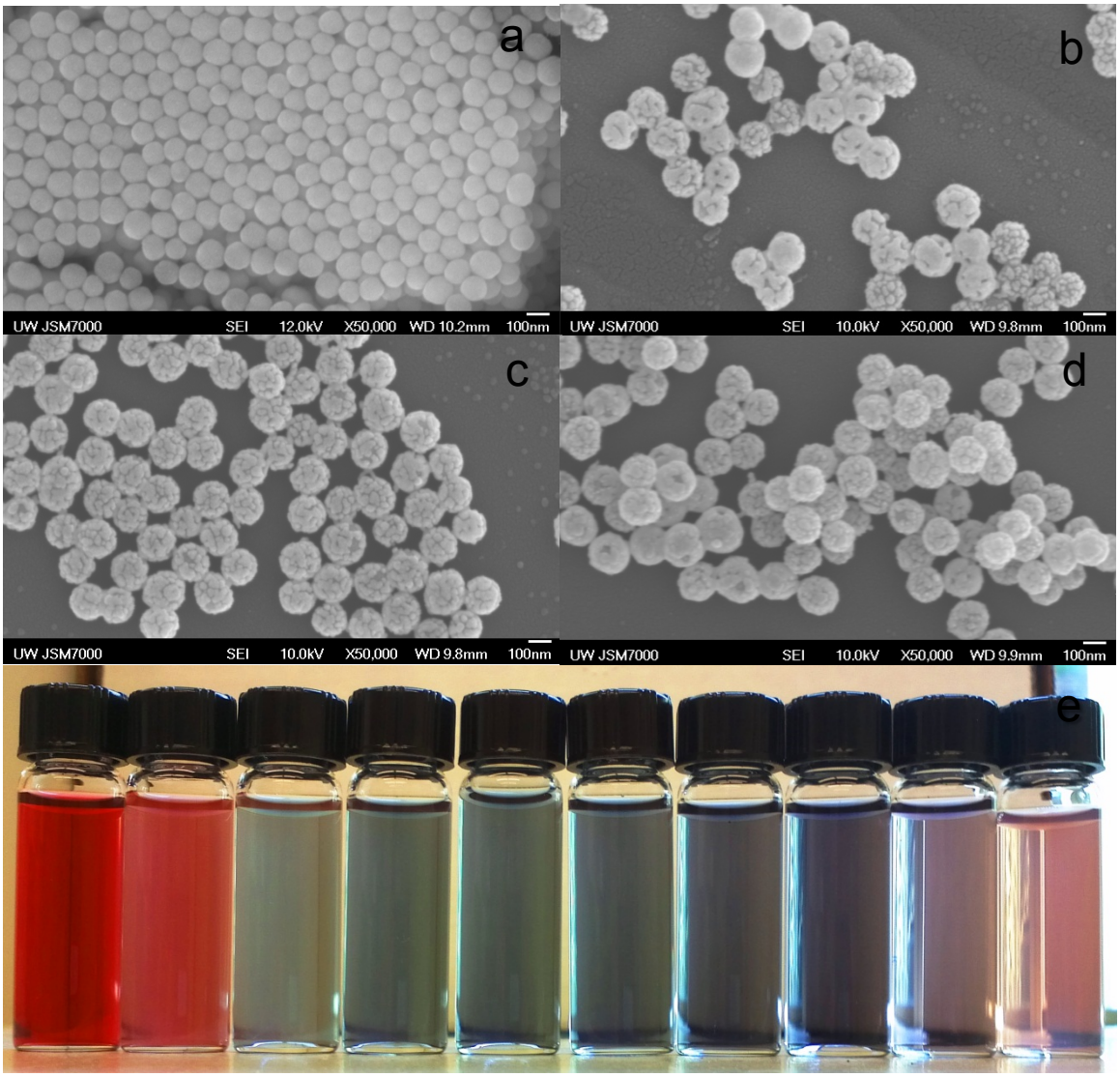

Figure 1. Fabricated silica core gold nanoshell particles used for thermal ablation. Bare silica core particles ~120nm diameter (a), nanoshell particles with increasing gold shell formation through additional gold ion solution reduction (b-d). Nanoparticle solutions at various stages of shell formation

Figure 1 displays the size and variance of the silica core nanoparticles and varying extents of nanoshell formation due to the reduction of increasing amounts of gold ion solution onto the silica cores using formaldehyde as the reducing agent. Many of the defects that have been observed on

previous nanoshell formations in *Figure 2* are present to some extent in this group of nanoshells as well based on the SEM images.

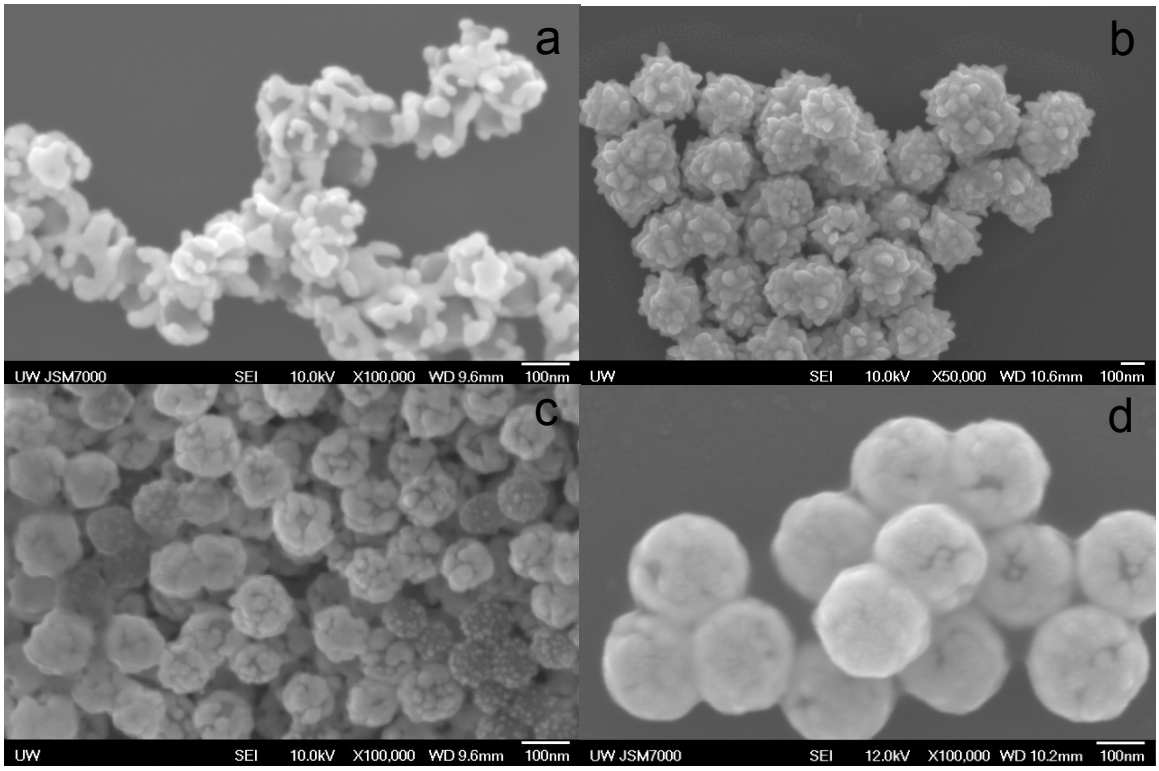

Figure 2. Common defects associated with gold shell formation using aqueous reducing agents such as formaldehyde: Uneven coalescence of islands (a), high surface roughness (b), and wide distribution of reduction levels (c). Even nanoshells deemed successfully coated show fissures and defects in the nanoshells (d).

However, even with the suboptimal nanoshells, the absorption spectra of each group in *Figure 3* is promising for use with 808nm laser irradiation with absorption peaks beginning at 800nm and blue-shifting back towards 750nm, although each subsequent group has higher overall absorption at 808nm. The broad peaks are indicative of a range of nanoshells at slightly different stages of shell completion in each sample, as well as due to the relatively high polydispersity of the silica core particles used.

Based on the promising results, a preliminary laser induced heating experiment was developed to test the thermal heating properties of the nanoshells on a solution. *Figure 3* displays the heating profiles for the three groups of nanoshells tested compared to laser induced heating of a water sample as a control. The results show a pronounced heating effect on the nanoshell solutions,

indicating successful preparation of nanoshells that can be used for laser nanoshell enabled photothermal therapy.

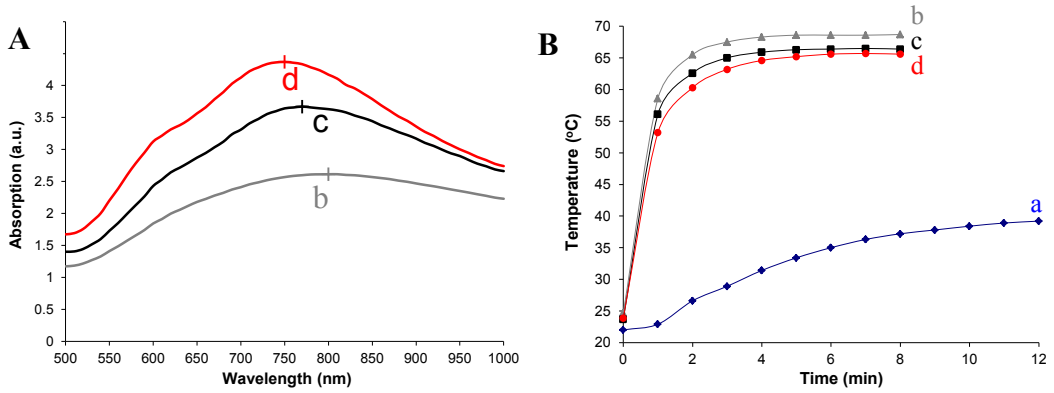

Figure 3. Optical absorption spectra of nanoshells (A) and laser induced heating of nanoshells dispersed in water using 808nm laser. Temperature change measured in 24 well plates using a thermocouple (B) in water (a) and nanoshells corresponding to SEM images (b-d).

An updated reduction process was developed utilizing carbon monoxide as a reducing agent for the formation of the gold shell. Reduction with carbon monoxide was achieved by bubbling the CO gas through the gold ion solution containing the colloidal gold coated silica particles. Gold nanoshells consisted of a silica core with 119 ± 11nm in diameter and a 17 nm gold shell. The gold nanoshells exhibited a broad absorption peak at 780 nm is shown in *Figure 4.* The size distribution and aggregation of nanoshells were monitored using a Zetasizer (Malvern Instruments ZS-90), with a hydrodynamic diameter of 206±10nm and a polydispersity index of 0.28

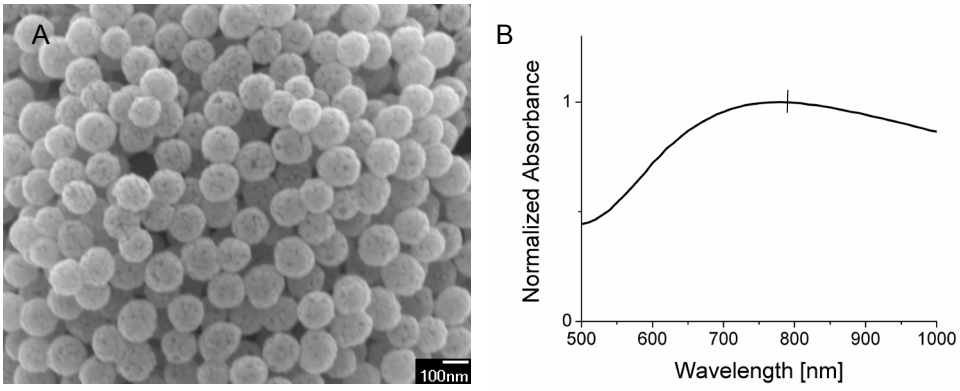

Figure 4. Characterization of gold nanoshells used in the following studies. (A)Scanning electron microscopy(SEM) image of synthesized gold nanoshells with 119 ± 11nm diameter silica core and a 17nm shell, and (B) their normalized UV-Vis absorption spectra in water. The nanoshells synthesized have an SPR peak in the NIR region at 780nm.

Pegylation of the nanoshells was assessed for a range of PEG concentrations using 5000MW Peg-SH. When excess PEG is used, pegylated nanoshells did not exhibit significant difference in surface coverage. Pegylation was assessed using dynamic light scattering to determine size and zeta potential. Pegylated nanoshells showed an increase in hydrodynamic diameter and decreased zeta potential in accordance with literature findings(*Figure 5*).

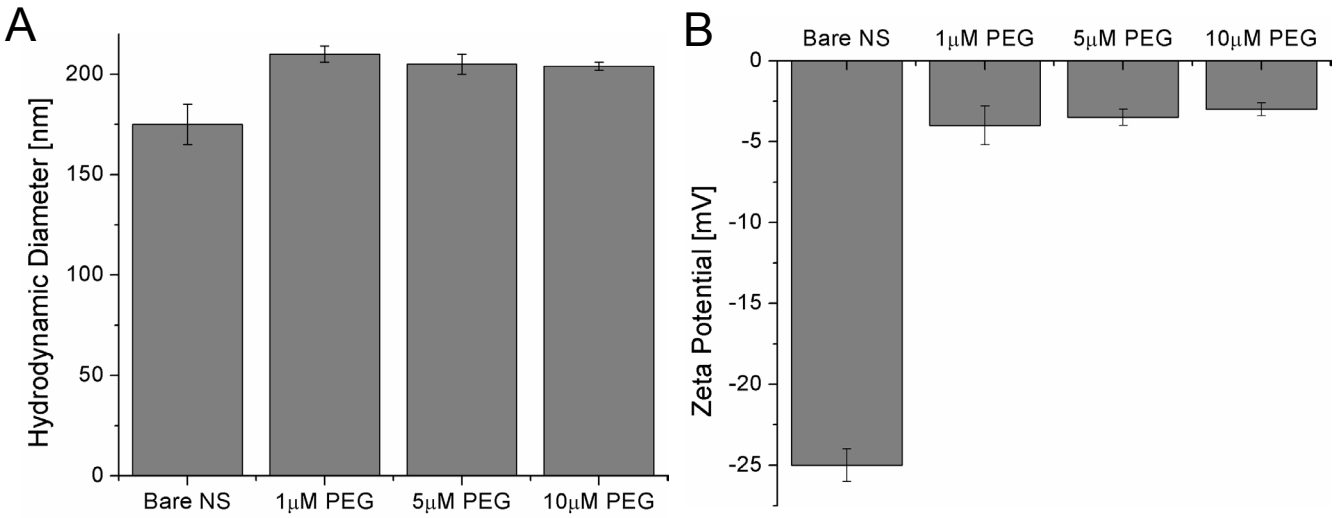

Figure 5. Pegylation of gold nanoshells with increasing PEG-SH concentrations. Dynamic light scattering measurement of A) hydrodynamic size B) zeta potential.

C. Chapter 3: *In vitro* cell responses to NEPTT

C.1 Background

Hyperthermia, the treatment of cancer with varying forms of heat, has long been studied using a multitude of methods and temperatures with varying effectiveness as a noninvasive alternative to conventional cancer treatment[31]. Localized hyperthermia, which includes photothermal therapy, is a subset which has garnered growing interest. Gold nanoparticles with various geometries, from spherical gold nanoparticles[32], nanorods[33-35], nanocages[36], and nanoshells[3, 6, 9, 36-40], have been demonstrated as excellent candidates to convert light energy to heat for PTT. Gold nanoshells are particularly appealing because of their optical resonance tuneability into the near infrared (NIR) region, where tissues are most transparent to light, and good biocompatibility owing to the inert metal shell, as well as the ease of surface functionalization for enhancing "stealthing" properties with PEG [8] or cell-specific targeting by antibodies[4, 5, 8, 41]. While a number of studies have used gold nanoshell mediated PTT both *in vivo*[9-12] and *in vitro*[4-8] for cancer cell destruction in a qualitative way, very little has been done to quantify the effects of the various treatment parameters on cancer cells[3, 12]. *Table 1* provides a comprehensive summary of treatment parameters employed using nanoshells photothermal therapy. Little is known about the actual process in which the nanoshells mediate the death of the treated cells, and the combination of conditions that lead to efficient ablation of cancer cells or tumors.

Source	Cancer Cell System	Cell Density	Gold Nanoshell Dose	Targeting	PTT Conditions
Hirsch 2003[10]	SK-BR-3 human breast carcinoma cells	Not stated	$4.4x10^9$ NS/ml 12 well plate	PEG	Not stated
Loo 2004[42]	SK-BR-3 human breast carcinoma cells	Cultured to full confluency 24 well plate	$2x10^9$ NS/ml	Anti-HER2	820nm 35W/cm2 for 7 mins
Loo 2005[7]	SK-BR-3 human breast carcinoma cells	Not stated	$3x10^9$ NS/ml 0.5ml	Anti-HER2	820nm 35W/cm2 for 7 mins
Lowery 2006[8]	SK-BR-3 human breast carcinoma cells	$1x10^4$ cells/well 24 well grown to near confluency	$2.9x10^8$ NS/ml in 0.5ml 24 well plate	Anti- HER2	820nm $8x10^{-5}$ W/cm^2(0.8 W/m^2) for 7 mins
Stern 2007[43]	PC-3 C4-2 human prostate cancer cells	$3x10^5$ cells/35mm plate, $8x10^3$ cells/well 96 well plate	4-8000 NS/cell	N/A	810nm 88W/cm^2 for 5 mins
Fu 2008[44]	SK-BR-3 human breast carcinoma cells	$5\text{-}8x10^4$ cells/cm-2 25cm^2 culture flask	1-1.5 NS/ml	Anti-HER2	N/A
Gobin 2008[5]	PC-3 human prostate cancer cells, HDF dermal fibroblast cells	Not stated	$3.0x10^9$ NS/ml	Anti-EphA2, PEG	808nm 80W/cm^2 for 7 mins
Bernardi 2009[4]	Daoy & Daoy.2 human medulloblastoma, U373 & U87 glioma, HDF dermal fibroblast cells	Not stated	$7.2X10^9$ NS/ml in 0.5ml 24 well plate	Anti- HER2, IL13Rα2	800 nm 80W/cm^2 for 2 mins

Table 2: Summary of *in vitro* nanoshell photothermal therapy literature

It is apparent that temperature is one of the key parameters in hyperthermia and photothermal therapy, and much work has been done for various aspects related to plasmon induced nanoshell heating. Theoretical calculations have predicted surface temperatures on nanoshells during irradiation in the thousands of Kelvins, but due to the small size and mass of the nanoshells the temperature drop-off is also predicted to be rapid[45]. Theoretical modeling has shown transient temperatures near the surface of nanoshells up to 350 times the steady state bulk temperature[46]. Nanoshell based photothermal therapy thus is a process of localized heat generation that leads to conduction first into the space near nanoparticle accumulation and eventually build up of heat resulting in a general temperature rise from the thermal gradients which must be present near the heat sources, the nanoshells.

Cell death from localized hyperthermia can be a complicated process involving damage to many intracellular components and organelles[31, 47-49], including membrane injury and an

increase in its permeability[49-51], and DNA damage [51-55]. Cell death can occur either through a necrotic or apoptotic pathway, both of which have been suggested as desirable modes for cancer therapy. Apoptosis, a more natural form of cell death has been the preferred method for many chemotherapies due to the minimization of an inflammatory response, while other researchers try to elicit an immune response for cancer immunotherapy through cell death modulation[56]. Necrosis, a non-natural form of cell death associated with irrepairable cell injury, in general elicits an inflammatory response to the cell trauma and a corresponding immune response. [57]Hyperthermia has been shown to be an efficient method for modulate the cell death mechanism through careful control of treatment parameters[58, 59].

Cell death from localized hyperthermia can be a complicated process involving damage to many intracellular components and organelles[31, 47-49]. Membrane injury and subsequent increase in permeability is implicated quite often as a major factor in cell death[49-51]. DNA damage has also been suggested as a key modulator of cell death[51-55].

In our current study, we investigated the effect of nanoshell dosage concentration, laser fluence, total irradiation time, and cell density on the mechanisms of cell death using a more quantitative approach than had previously been completed. We also look at the effects of nanoshell heating on the environment surrounding the treated cells and indirect damage to adjacent cells. These parameters provide a model of the conditions present *in vivo*, and our results can potentially provide a basis for the combination of photothermal therapy and immunotherapy of cancers.

C.2 Research Design and Methods

Cell Culture and Incubation of Nanoshells with Cells.

9L rat gliosarcoma cells (ATCC BRC) were maintained in Dulbecco's Modified Eagle medium(DMEM) containing 10% FBS, 1% antibiotics, L-glutamine, and sodium pyruvate at 37^{o}C and 5% CO_2. Cells were plated in flat bottom 24 well plates and allowed to attach for 24 hours before incubation with nanoshells. Nanoshells were centrifuged and redispersed in cell culture media without the addition of FBS, and diluted to the designated concentrations in additional media. Cells were incubated with 500 µl of nanoshell solution for 3 hours to allow for uptake and internalization of particles. Cells were then rinsed with fresh media three times to remove unbound nanoshells prior to laser irradiation. Cells were imaged in 24 well plates under a bright-field microscope (Nikon Eclipse TE2000-U) with a CCD camera (Photometrics Coolsnap ES). Images were taken at the same exposure level and magnification for all samples.

Quantification of nanoshell uptake

Cells were incubated nanoshells redispersed in cell culture media without the addition of FBS with the addition of 200µg/ml of the green fluorescent dye Calcein for 3 hours prior to washing and detachment and redispersing in FACS media followed by analysis using flow cytometry. Changes in fluorescent intensity were measure in the FL-1 channel and differences in the mean fluorescent intensity(MFI) between the control population and the nanoshell treated samples were calculated.

Laser irradiation of cells loaded with nanoshells

Cells were detached with 0.05% trypsin and resuspended in 200 µl fresh culture media prior to the laser irradiation. Cells were treated in 96 well plates containing 100 µl of redispersed cell solutions(2 wells per sample) using a diode laser (Newport Corporation, 808nm, 23W/cm^2 max) positioned to illuminate the full well area of a 96well plate for each sample. Immediately

following irradiation, the temperature of the well solution was measured, and the cells recombined into one sample per concentration for flow cytometric analysis.

Analysis of Apoptosis and Necrosis by Flow Cytometry

The apoptosis assay kit (Annexin V, BD Biosciences) was used for assessment of cell viability and mode of death using flow cytometry. The laser-irradiated cells and controls were washed 2 times with cold PBS and then resuspended in the binding buffer. The staining of cells followed the instructions as suggested by the manufacture. The samples were analyzed within the hour using flow cytometry (BD FACScan, Univ. of Washington Cell Analysis Facility). Untreated viable cells and cells treated in water bath at 80^{o}C to induce necrosis for 5 min were used as controls and for compensation.

Nanoshell treated cell staining

To differentiate between nanoshell treated cells and untreated cells, cells were co-incubated with nanoshells redispersed in media without serum along with the cell permeable dye Calcein-AM for 3 hours to allow for uptake up the nanoshells and cleavage of the dye into the green fluorescent cell impermeable calcein fraction. Cells were washed with PBS 2 times to remove excess particles and dye before detachment and redispersal in media, and mixed at ratios from 100:0 to 0:100 with untreated cells prior to laser irradiation. Viability was assessed using the fluorescent dye 7-AAD, and the samples were process by flow cytometry using the FL-1 channel to gate for treated and untreated cell populations, and the FL-3 channel for viability.

Cell Killing Mechanism Assay

An apoptosis assay kit(Annexin V, BD Biosciences) for flow cytometry. The cells were washed 2 times with cold PBS before being resuspended in the binding buffer solution. Fluorescently conjugated Annexin V and 7-AAD dyes were added, followed by a 15 minute incubation at room temperature in the dark before dilution with additional buffer. The samples

were analyzed within the hour using flow cytometry(BD Facsan). The samples were gated using a control consisting of untreated viable cells and. Compensation was performed with cells undergoing necrosis by a standard protocol utilizing water bath incubation at 80^{o}C for 5 minutes.

Membrane Permeability Assay

Cells were incubated with cell permeant dye calcein-AM at a concentration of 5 μM prior to laser irradiation along with the nanoshells. Cells were washed 3 times before being redispersed in 100 μl of cell media and treated as previously described. Following PTT, cells were washed in DPBS prior to being redispersed in FACS buffer consisting of DPBS containing 5% FBS solution. Samples were stored on ice and analyzed within the hour using flow cytometry.

DNA Fragmentation Assessment

DNA extraction for electrophoresis and flow cytometric analysis was performed using a protocol described by Gong et al for extraction of lower molecular weight DNA[60]. Treated cells were collected for DNA fragment extraction and fixed in 70% cold ethanol after resuspension in Hank's Buffered Salt Solution (HBSS). Cells were stored for a minimum of 24 hours at -20^{o}C. Cells were pelleted with a centrifuge at 800g for 5 minutes and redispersed in 40μl of phosphate citric acid buffer(PCB pH 7.8) and incubated at 37^{o}C for 30 minutes to enhance DNA fragment migration. The solution was centrifuged down at 1000g for 5 minutes to pellet the cells. The supernatant was carefully removed and treated sequentially with RNase A and Proteinase K before running on an electrophoresis gel prepared at a concentration of 1.5% agarose. The gel was run with 1X TBE buffer at 100V for 2 hours followed by DNA staining with SYBR Green fluorescent dye. A positive control was prepared by treating cells with the apoptosis inducing drug Camptothecin at a concentration of 10μM for 24 hours. Linear DNA size markers in 100bp and 1kbp ranges were obtained from New England Biosciences and prepared as instructed.

Cellular DNA Content Assessment

The cell pellet obtained following DNA extraction was used to assess the DNA content of the cells by staining with the fluorescent dye DAPI. Treated cells were stained with DAPI solution prepared with 100mM HEPES, 2mM $CaCl_2$, 0.1% Triton X-100, and 1μg/ml DAPI for 15 minutes prior to analysis with flow cytometry. Cell doublets were gated out by comparing DAPI-Area vs. DAPI-Height as indicated. Cells with DNA content below the g1 subpopulation were gated for DNA loss.

Effect of doses of gold nanoshells on cell death

Cell death resulting from hyperthermia can be categorized as either necrosis or apoptosis, and forms of cell death were assessed by flow cytometry using the combination of 7-Amino-Actinomycin (7-AAD) and fluorescently conjugated Annexin V. 7-AAD is a fluorescent dye that has a high affinity for DNA, but impermeable to an intact cell membrane. During late stages of cell death either through necrosis or late stages of apoptosis, the plasma membrane becomes permeable to 7-AAD. As a result, the 7-AAD can access the nuclei and bind to DNA. Annexin V can bind to the membrane ligand phosphatidylserine (PS). For viable cells, few PS is present on the intracellular side of cell membranes compared to cells undergoing the early stages of apoptosis where PS is externalized. When cells exhibit binding to Annexin V but not to 7-AAD, cells are at an early stage of apoptotic cell death. When cells exhibit the binding to both Annexin V and 7-AAD, cells undergo either necrosis or late stages of apoptosis[61, 62]. Since the cells were processed and stained promptly following PTT, cells positive for both dyes are considered necrotic.

C.3 Results

Uptake and cellular distribution of Nanoshells

The cellular uptake of nanoshells was first qualitatively assessed by using optical microscopy (*Figure 6A*). Gold nanoshells appeared to be darker compared with intracellular

components. There existed a correlation between the dosing of nanoshells and the cellular uptake, with little to no observable uptake at the lower dosing concentrations. Following 3 hour-incubation, nanoshells were accumulated in the perinuclear region, which was more obvious at the higher dose compared to lower dose. Heterogeneous uptake was observed among cells at the same dosing of nanoshells, particularly at the lower dose of nanoshells.

To semi-quantitatively measure nanoshell uptake, the change in fluorescent intensity of the samples incubated with nanoshells were compared to controls containing only the green fluorescent Calcein dye using the mean fluorescent intensity of the population. This data is the inset plot for the respective dosing and the MFI is graphed in *Figure 6B*, with quenching calculated as the difference in the mean fluorescence intensity of the control population compared to the sample.

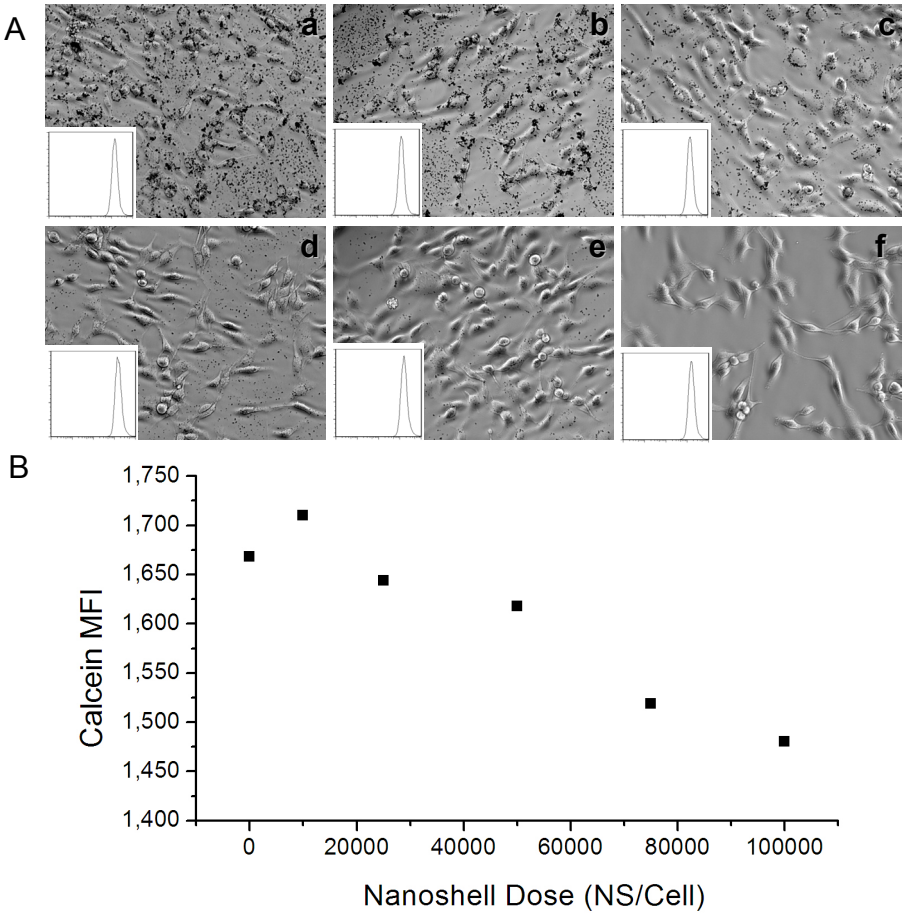

Figure 6. Relative nanoshell uptake quantification determined by decrease in fluorescence by nanoshell quenching. (A) Light microscopy imaging of 9L cells incubated with nanoshells from 100,000-10,000 nanoshells/cell with nanoshells showing localization and internalization. Cells stained with 200 μg/ml Calcein during nanoshell incubation. Fluorescence quenching calculated as the change in the mean fluorescent intensity between the control population and the nanoshell treated samples.

Cells were first exposed to varying dosing of gold nanoshells for 3 hours and irradiated with an 808nm laser at a constant 23 W/cm^2 power for 5 min, within the typical *in vitro* treatment duration of 3-7 min used by various groups [5, 10, 36, 41]. Cell death was assessed immediately after the laser irradiation. As shown in *Figure 7*, at the higher doses of gold nanoshells, almost 100% of the cells underwent necrosis. As the doses of gold nanoshells were reduced, an increasing percentage of cells were viable and were not affected by gold nanoshell-mediated laser irradiation. A corresponding decrease in temperature was also observed as a function of nanoshell dose along with a threshold below 43^{o}C where minimal cell damage occurs. At a dosing of 15,000 nanoshells/cell, corresponding to a final temperature of 47^{o}C, a significant proportion of the cells underwent apoptosis, a mode of cell death not observed to a significant degree at other temperatures. Researchers looking at the effect of temperature during hyperthermia have observed a similar change in the mode of cell death at temperatures in that range for other cell lines[58]. The heterogeneity of cellular uptake of nanoshells at the lower doses may contribute to the non-uniform killing. This result indicates that the level of nanoshells internalized or localized on the surface of the cells is critical for the induction of cell death by laser-irradiation. Quantification of intracellular level of nanoshells can give a better assessment of the threshold of nanoshell dose required for cell death.

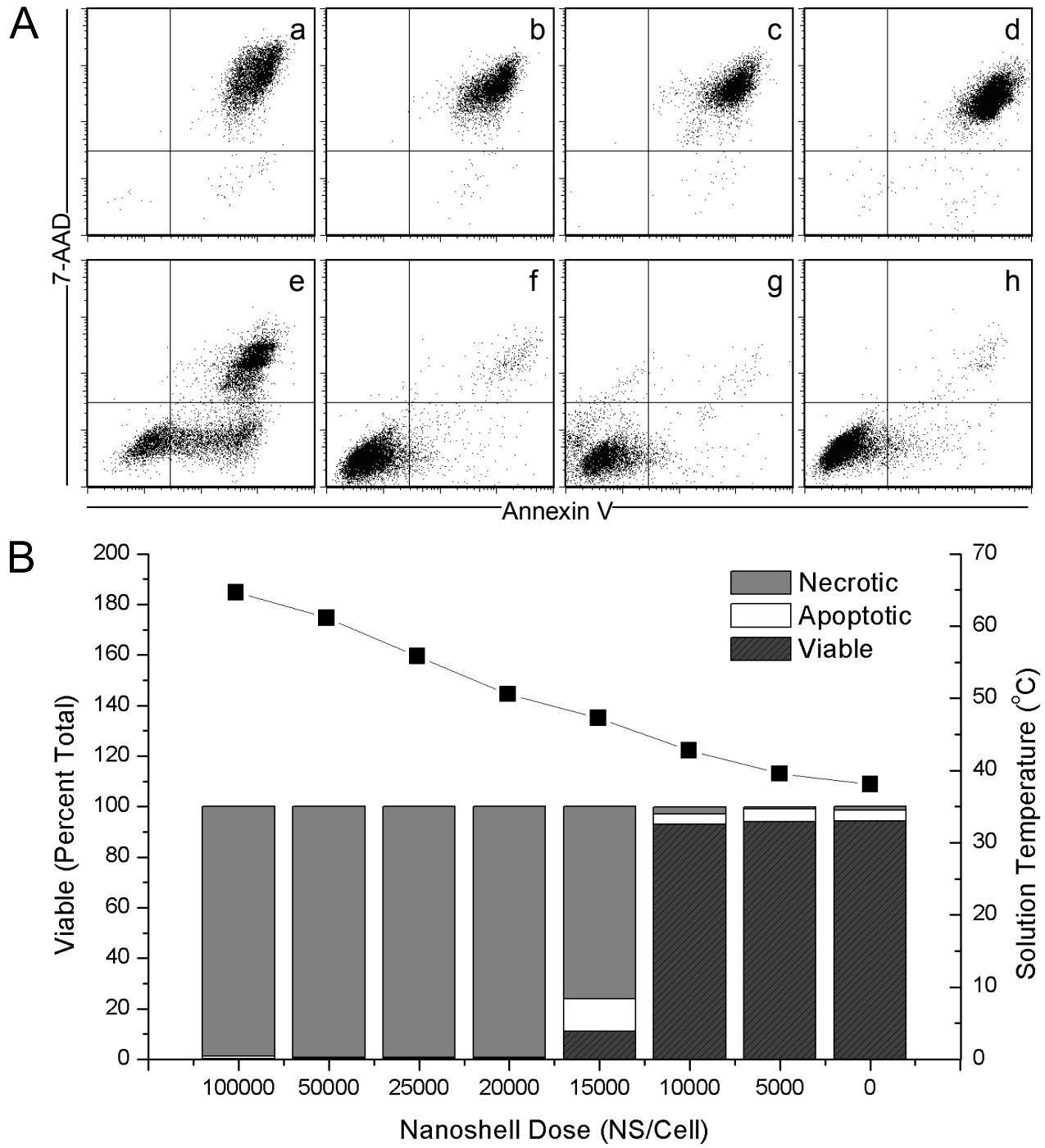

Figure 7. 9L cell death following nanoshell incubation for 3 hours and laser irradiation at 23W/cm^2 for 5 minutes quantified using flow cytometry. (A) Plots of cells stained with Annexin V-FITC and 7-AAD after PTT treatment to asses cell death. Viable cells are negative for both dyes, cells undergoing apoptosis are positive for Annexin V-PE but exclude 7-AAD, and cells undergoing necrosis stain positive for both dyes. (a) 100,000, (b) 50,000, (c) 25,000, (d) 20,000, (e) 15,000, (f) 10,000, (g) 5,000 nanoshells/cell and (h) control cells. (B) Distribution of cells states with modes of cell death affected by PTT and the solution temperature after PTT are plotted against the nanoshell dosage. Mainly necrotic cell death occurs for nanoshell doses above 20,000 corresponding to temperatures above 50^{o}C, mixture of necrotic and apoptotic cell death occurs at 15,000 nanoshells/cell with a temperature ~47^{o}C, and minimal cell death occurs below 5,000 nanoshells/cell at temperatures below 43^{o}C.

The effect of laser fluence on cell death

Due to the heterogeneity of tumor tissues, it is possible that individual tumor cells receive varying level of power density, that is, laser fluence dependant of the spatial relationship to the source of irradiation. We subsequently examined how the laser fluence affected the form of cell death at a given dose of nanoshells. The fluence at which 100% of cell death was achieved at 23 W/cm^2 for 5 minutes dosed at 50,000 nanoshells/cell. As shown in *Figure 8A*, when the fluence decreased while maintaining the total energy input constant by increasing the duration of irradiation, the fraction of cell death was reduced correspondingly. To achieve ~50% of cell death, approximately 18 W/cm^2 fluence was required. When the fluence was reduced to 5 W/cm^2, almost all the cells remained viable.

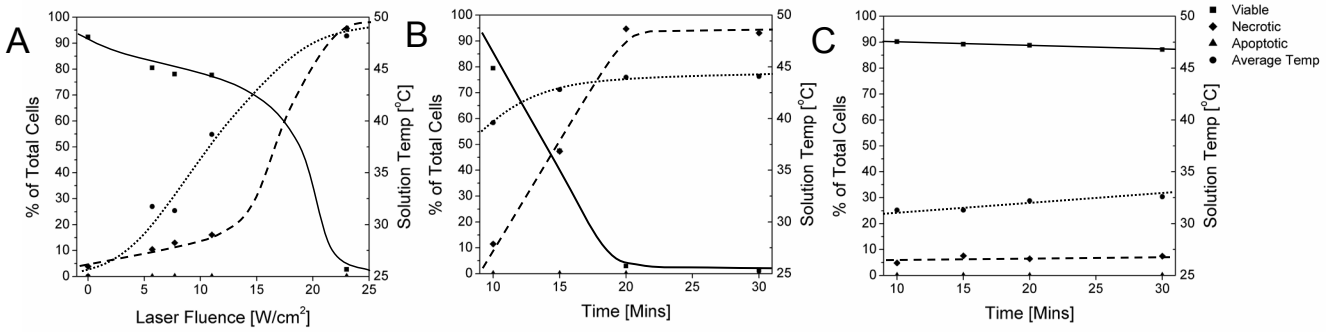

Figure 8. Effect of laser fluence and total laser power on cell killing. (A) Cells dosed at 50,000 NS/Cell where laser fluence during PTT was varied along with the total treatment time to keep total power input constant. Laser fluence:treatment times were applied as follows: 23W/cm^2:5mins, 11W/cm^2:10mins, 7.7W/cm^2:15mins, 5.7W/cm^2:20mins. PTT at a constant 11W/cm^2 (B) and 7.7W/cm^2 (C) for increasing treatment times to vary total laser power input. Total power input plays a lesser role compared to fluence rate in cell killing with a definite threshold fluence rate required to achieve significant amounts of cell killing.

The effect of laser irradiation time on cell death

The resistance of cells to elevated temperature has been shown to decrease dramatically in response to higher temperatures, thus exposure to increasing amounts of laser irradiation during photothermal therapy will increase the efficacy of killing. *Figure 8B* shows the increase in cell death as a result of longer exposure and the corresponding increase in temperature. Below a

threshold temperature at lower dosing however, heat can be dissipated efficiently enough that the threshold is not reached where significant cell death occurs in a reasonable treatment timeframe as shown in *Figure 8C*.

Our results demonstrate that the induction of complete cell death by nanoshell-mediated photothermal therapy requires sufficient level of total energy and laser fluence. In addition, there exists a threshold of laser fluence. The threshold of laser fluence can be affected by the thermal properties of local tissues and flow conditions, which potentially affect the accumulation of heat and thus local temperature around targeted tumor cells.

Effect of Localized Heating on Cell Death

Cells were first dosed with 50,000 nanoshells/cell and then diluted at various concentrations between 0.75-3^5 nanoshell-containing cells in 100 μl of medium. As a result, nanoshell-containing cells consisted of the same level of intracellular nanoshells, but at varying levels of cell density. As shown in *Figure 9A*, a decrease in cell death resulted from a decreased fraction of nanoshell-containing cells. These results indicate that a localized heating alone is not sufficient in inducing complete cell death. The density of nanoshell-containing cells plays a critical role of inducing complete cell death as well, likely contributing the amount of heat that can be dissipated into the medium.

Next we examined the role of the bulk temperature in the induction of cell death. We hypothesized that the exposure of cells to the same bulk solution temperature either through nanoshell-mediated PTT or a more convention external heating method by a water bath would provide comparable efficiencies of cell killing if the bulk temperature played a dominant role in the induction of cell death. As shown in *Figure 9B*, the bulk solution temperature (~50^{o}C) at which nearly complete cell death was achieved during PTT was significantly lower than that (~60^{o}C) using a water bath to heat the entire solution and cells more uniformly. Our results with water

bath treatment are consistent with previously reported by Ross-Riveros and Leith[63]. In their studies, 9L cells were subjected to temperatures in the range of 39-43^{o}C in a water bath. At temperatures below 41^{o}C, no cell death occurred for short incubation times below 6 hours. Above 43^{o}C cell killing was observed in 10-20% of the cells for short incubation periods in close agreement with our results. Therefore, the heating resulted from neighboring cells and/or extracellular matrix, and thus the rise of temperature in surrounding tissues(media), is critical for the induction of complete cell death by nanoshell-mediated PTT.

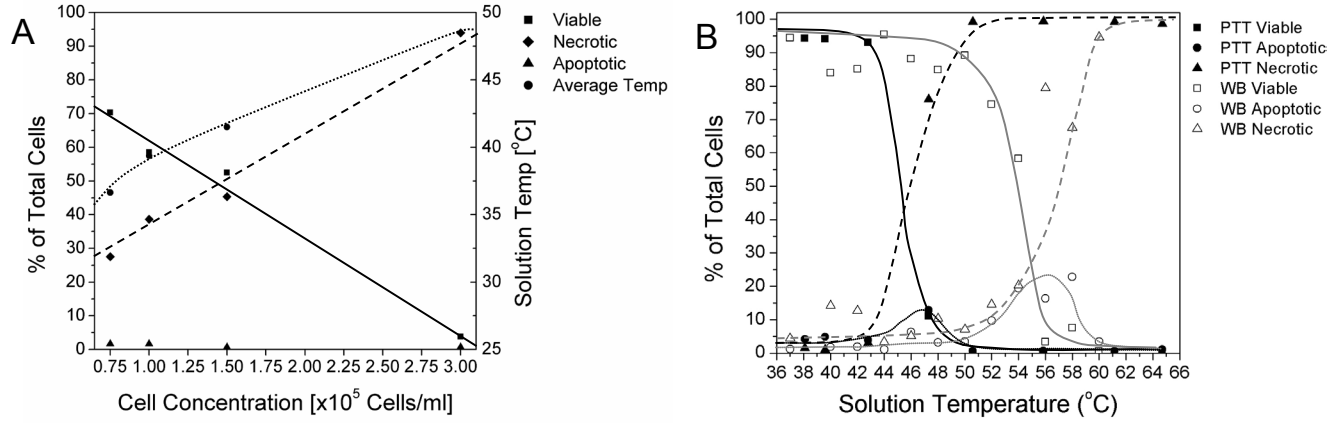

Figure 9. Effect of localized and overall heating on cell death. (A) Cells dosed at a rate of 50,000 NS/cell followed by dilution between 0.75-3x10^{3} cells/ml to change the cell concentration during PTT, total cell numbers were kept constant by treatment of additional wells at higher dilution rates recombined following completion of PTT for all samples. (B) Solutions temperatures during PTT required to achieve significant amounts of cell killing were compared with conventional hyperthermia treatment using water bath heating. Both localized and overall bulk heating during PTT play a role in determining cell death.

Effect of Localized Heating on Adjacent Cell Populations

Heterogeneous uptake of nanoshells was observed *in vitro* in our studies based in careful analysis of the images obtained showing nanoshell accumulation at all dosing concentrations. At higher nanoshell dosing treatments, cell death was observed in virtually all cells regardless of observed nanoshell uptake, whereas at lower dosing concentrations, heterogeneous populations of cell death were observed in samples dosed with the same concentration of nanoshells. We thus hypothesized that heat generated intracellularly due to absorption of light by the nanoshells

would dissipate and potentially effect the surrounding environment and cells in close proximity, resulting in cell damage to untreated cells. By mixing various ratios of nanoshell treated cells with untreated cells the extent of interaction and damage could be assessed. *Figure 10* shows the results of two different samples treated with high and low nanoshell concentrations. At the higher nanoshell dose(Figure 9B), the treated cells were able to efficiently kill untreated cells nearby at a wide range of ratios while still efficiently damaging the treated cells. Only where a small percentage of treated cells were present did the extent of the heating effects become muted. This would indicate that above a threshold loading, the amount of energy absorbed by the nanoshells resulted in elevated temperatures through dissipation to a level that could affect the surrounding population. At a lower nanoshell dose, the extent of this effect decreased more dramatically as the ratio of treated cells to untreated cells decreased. In addition some of the nanoshell treated cells did not die which is the result of heat dissipation in a manner observed in the samples from *Figure 9A* at lower cell densities. Heat generated is dissipated at a rate below the rate of thermal resistance of the cells. The implication is that homogenous distribution of nanoshells is not required throughout the tumor as long as sufficient nanoshell loading occurs. However, damage to healthy tissue surrounding the tumor is also a possible undesired side effect.

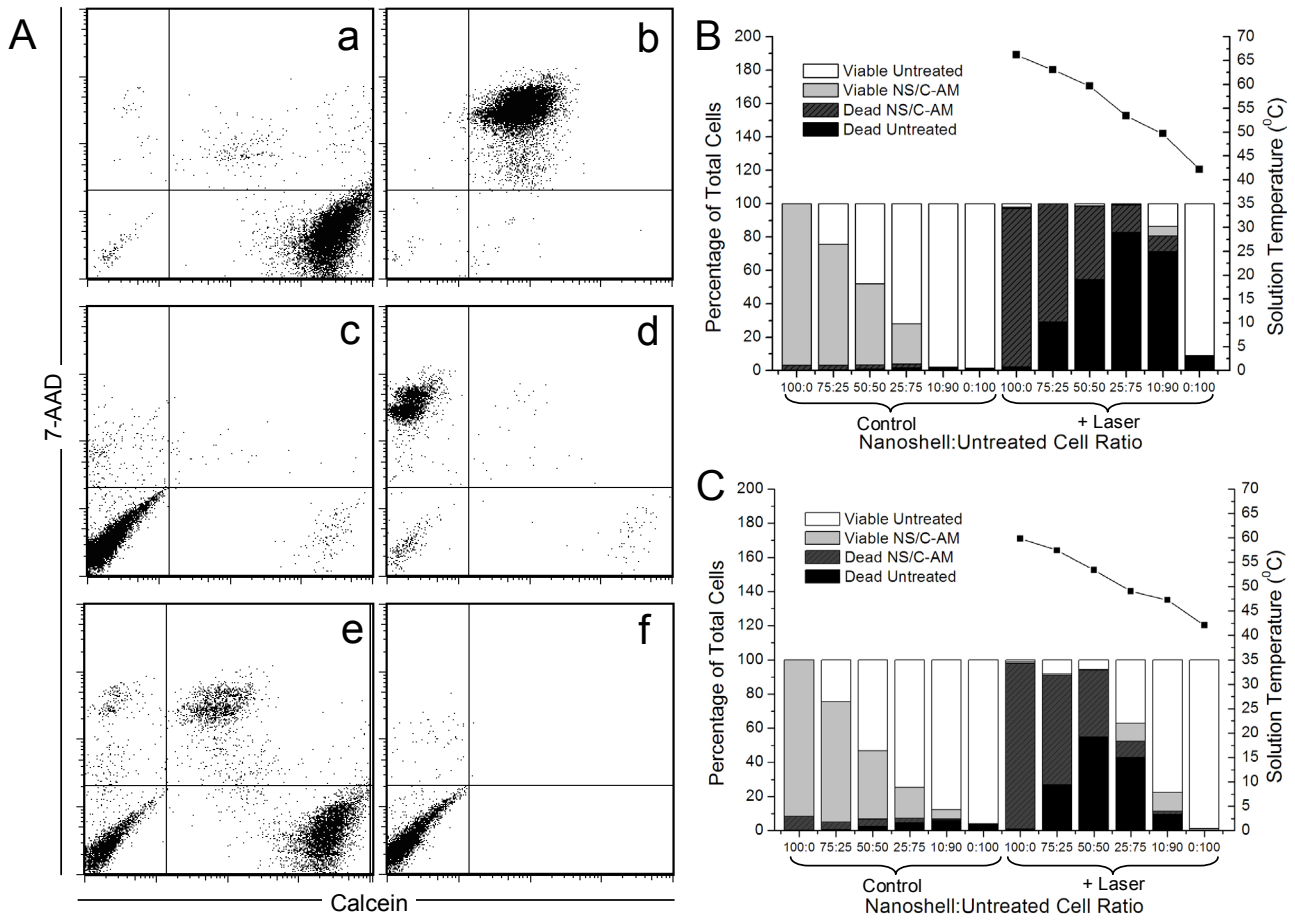

Figure 10. Effect of nanoshell treated cell heating on surrounding cells in the environment. (A) Nanoshell treated cells stained with Calcein-AM to differentiate from bare cells assessed by flow cytometry for cell viability prior to and after PTT. (a) Viable nanoshell treated cells stained with calcein negative for the viability stain 7-AAD, (b) dead nanoshell treated cells stained with calcein positive for the viability stain 7-AAD, (c) untreated viable cells negative for the viability stain 7-AAD, (d) untreated dead cells positive for the viability stain 7-AAD, (e) mixture of all possible cell populations, (f) unstained control cells. (B) 9L cells treated with 100,000 NS/Cell (B) and 50,000 NS/Cell (C) mixed at various ratios of [nanoshell treated:untreated] prior to PTT.

Mechanisms of Cell Injury

Loss of membrane integrity has long been associated with irrepairable cell damage and subsequent onset of cell death through a necrotic pathway[50, 51]. Calcein-AM is a commonly used indicator of membrane permeability. Initially membrane permeable and nonfluorescent, cleavage by intracellular esterases produces the membrane impermeant fluorescent calcein anion[64]. Calcein-AM was employed by the West group[5, 7, 10] as an indicator of cell viability, although a dosage dependence was not determined and internalization of the nanoshells was not

verified. *Figure 11* clearly shows the effects of nanoshell mediated PTT at varying dosages on the membrane integrity of the cell and the resulting damage as a function of concentration. The nanoshell concentration in turn affected the heating and subsequent temperature rise, which plays a key role in membrane damage as evidenced by the water bath samples that show loss of fluorescence. For 9L cells, temperatures in excess of 45°C begin to damage the cell membrane resulting in loss of calcein. This corresponds with the cell viability data above from *Figure 8*, although the measurements are of essentially the same membrane integrity.

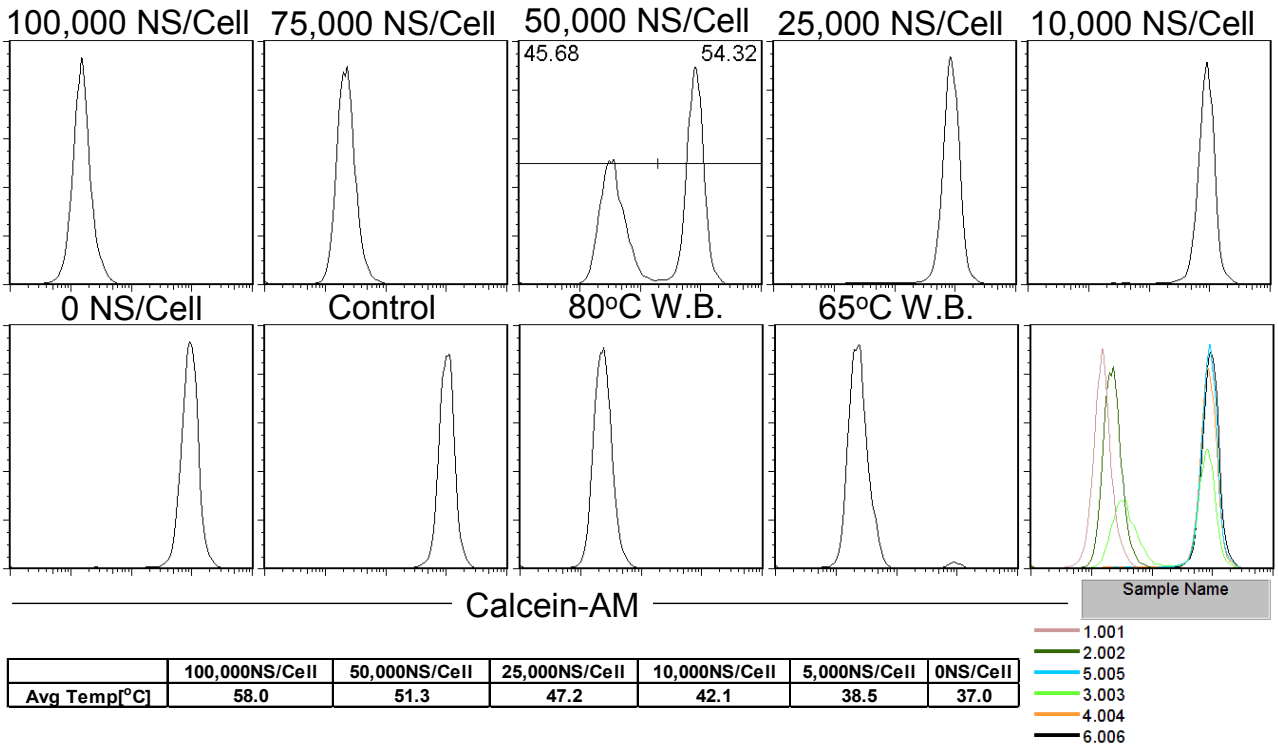

	100,000NS/Cell	50,000NS/Cell	25,000NS/Cell	10,000NS/Cell	5,000NS/Cell	0NS/Cell
Avg Temp[°C]	58.0	51.3	47.2	42.1	38.5	37.0

Figure 11. Membrane permeability changes following nanoshell enabled photothermal therapy(NEPTT) and average bulk solution temperatures recorded following laser irradiation. Cells dosed at varying concentrations of nanoshells and 5 μM Calcein AM as well as water bath treatments near the high bulk solution temperatures observed during PTT. Membrane integrity loss is associated with elevated temperatures greater than 50°C for short 5 minute duration treatments used.

Loss of membrane integrity in the context of heat damage is an irreversible injury that proceeds to cell death, however, it may not be the one of the major cell functions that are damaged during nanoshell PTT resulting in loss of cell viability. Nanoshell accumulation in the perinuclear

region of the cell places the heat source near the DNA within the nucleus that may be damaged earlier in the heating process.

Heat induced DNA damage is not well understood due the complexities associated with its constant replication and repair by enzymes and proteins. DNA can be denatured at elevated temperatures and nicks in the strands, either in a single or double strand. Whether double strand nicks resulting in DNA fragmentation from direct heat is still unclear with contradictory findings[55, 65], with different methods of heating being implicated as a possible reason for confliction reports related to DNA double strand breaks[66]. What has been observed is that DNA can become damaged when exposed to elevated temperatures, which may be a result of direct heat damage or loss of DNA repair mechanisms and protein denaturation that stabilizes nuclear DNA[31, 51-55]. Replication can also be inhibited which would explain the increased susceptibility of S-phase cells to heat damage[51].

Heat may also induce apoptosis which activates endonucleases that cleave nuclear dna into fragments of multiples of 180bp, forming a DNA ladder pattern when extracted DNA is run on a agarose gel. DNA laddering through induced apoptosis is observed for the positive control treated with Camptothecin shown in *Figure 12A*. Loss in DNA content results in a sub g1 population of cells when DNA content is determined as shown in *Figure 12B* for DAPI stained cells. Although no DNA laddering appears for nanoshell PTT treated samples, DNA bands appearing in the >10kbp range corresponding with cells exhibiting decreased DNA content staining for the cells treated with 50,000 and 25,000 nanoshells/cell respectively indicate that some type of DNA damage or fragmentation is occurring. It is also feasible that random DNA fragmentation and damage could be occurring which are at levels below the sensitivity of the gels. Evidence of this is occurring may be seen in the samples treated with the highest concentration of nanoshells, where the highest temperatures are observed increasing the likelihood of DNA damage. A definite shift the DNA

content of those cells observed from the flow cytometry data without corresponding staining on the gel could indicate random fragmentation of DNA.

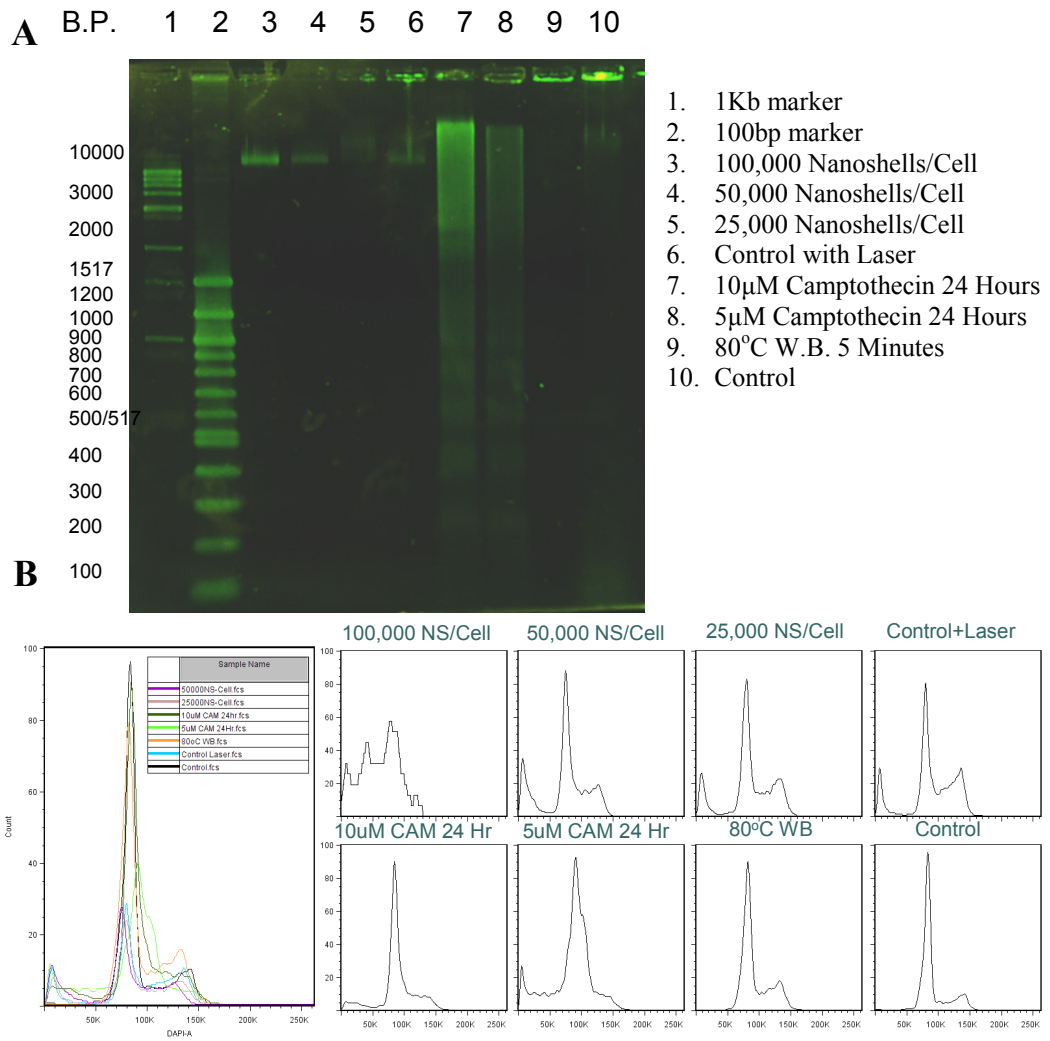

Figure 12. DNA damage following photothermal therapy. (A) DNA fragments recovered from cells treated with PTT and conventional hyperthermia. A 1.5% agarose gel stained with SYBR Green illuminated with UV light. Extracted DNA was treated with RNase A and Proteinase K to remove residual contaminants prior to loading. (B) Cells used for DNA extraction are stained for DNA content using the fluorescent dye DAPI as a confirmation of DNA fragmentation that appears on the gel. Cell doublets are gated out using DAPI-A vs. DAPI-H.

Another potential source of DNA is from the mitochondria, which is another organelle potentially damaged by heating from PTT. Mitochondrial DNA exists as a ring of DNA 10-15kbp long, which could be the DNA band observed in our experiment. Mitochondrial damage has been observed due to heat[51] and also by PTT using gold nanorods as the heat absorber[34, 35]. Damage to nuclear or mitochondrial DNA would also represent an likely irreversible cellular injury contributing to the mechanism of cell death by nanoshell mediated PTT.

C.4 Discussion

Our study determined a semi-quantitative way to measure nanoshell uptake combined with high magnification cell microscopy to show internalization and localization of nanoshells. We determined the effect of nanoshell dosing, laser fluence, and cell density on cell death following PTT using a quantitative approach. The contribution from direct localized heating from nanoshells on cells directly and indirectly treated was determined in a more qualitative manner. These results, taken as a whole, provide insight into the various parameters and conditions that exist within a heterogeneous tumor cell population. Our study provides further understanding of tumor treatment by nanoshell-mediated PTT in clinical settings.

Nanoshell mediated photothermal therapy in vivo relies on the preferential accumulation and uptake of the nanoshells in tumor tissue. This is most commonly achieved through intravenous injection of nanoparticles that have been pegylated to reduce clearance by the immune system. Increased nanoparticle accumulation occurs in tumor tissues due to the enhanced permeability and retention (EPR) effect. Intravenously injected nanoparticles circulate in the blood stream and extravasate into tumor tissues defective and leaky vasculature barriers[67]. Tumor neovasculature is often poorly distributed leading to hypoxic regions. Blood vessels supplying the tumor are often defective and have poorly aligned endothelial cells allowing the leakage of macromolecules and nanoparticles in the tumor interstitium(extracellular space). Combined with the lack of effective lymph drainage, passive accumulation and diffusion of nanoparticles into the tumor near the blood vessels can occur. This nanoparticle diffusion within the extracellular space of tumor tissues will be limited due to the lack of convective flow, leading to the development of nanoshell concentration gradients emanating from the leaky vessels. The nanoshell distribution within the tumor tissue will thus be concentrated around the vasculature resulting in both a heterogeneous accumulation in the local cell environment and cellular uptake

of nanoshells[67]. Imaging of tumors treated intravenously with nanoshells indeed illustrates heterogeneous accumulation of nanoshells within tumor tissues [68]. A schematic representation of possible nanoshell distributions within a tumor are shown in *Figure 13*, cell uptake can range from very high in tissues located near blood vessels, to no nanoshell accumulation at all in hypoxic regions with little to no blood flow. A combination of any of the proposed distributions exists within larger tumors. The effect of intracellular level of nanoshells on the induction of cell death, as shown in *Figure 6*, can lend some insight into how the heterogeneous cellular level of nanoshells would affect the eradication of tumors in clinical practice, in particular the threshold levels of nanoshells required for significant cell death. The dose effect can be manifested for larger sizes of tumors. Therefore, it is critical to employ strategies to ensure a sufficient level of cellular uptake of nanoshells.

Laser light used to irradiate the tumor may not have an unimpeded path *in vivo*. A laser beam commonly has a Gaussian beam profile that has an intensity that is a function of its radial distance from the central axis. Beam intensity falls as a function of the distance and penetration depth of a medium due to absorption and scattering which is dependent on the optical properties of the light path. The laser fluence received by an individual tumor cell is highly dependent on the anatomical location of cells and optical properties of surrounding tissues. Experimental and theoretical models for homogenous tissue phantoms show the laser-temperature relationship[45]. NIR laser penetration depth for tissue is no more than a few centimeters[3]. Based on our results shown in *Figure 8*, laser fluence has significant impact on the induction of cell death by nanoshell-mediated PTT. It is possible that tumor cells can escape from cell death through low levels of laser irradiation though high levels of intracellular nanoshells are achieved. In a worst case treatment scenario, regions of the tumor can receive little to no nanoshell accumulation and receive no laser irradiation.

In addition to the effect of intracellular level of nanoshells and fluence on cell death, we also demonstrate that both short- and long-range heating is critical for the induction of cell death. The short-range heating is associated with the cellular uptake of nanoshells, the laser fluence received by cells, and thermal properties of cells. The long-range of heating is dependent on the distribution of nanoshell-containing cells and thermal properties of tissues. Several situations can be envisioned as shown in *Figure 13*. In additional, our in vitro studies to not account for the accumulation and distribution of nanoshells in the interstitium of the tumor, but the method of cell injury and subsequent death could be rather dissimilar. Each scenario may result in different efficacy of the eradication of tumors. The complexicity of tumor structures and vasculature and dimensions associated with individual clinical cases can compound the prediction of successful rates of nanoshell-mediated PTT.

Given our findings, many *in vivo* studies have shown the efficacy of nanoshell-based photothermal therapy, which may arguably indicate that our observations may be due to our experimental settings. We would like to mention that, in all the *in vivo* studies, the size of tumors is within 1 to 3 mm in diameter, and all the tumors are grown subcutaneously. In addition, a relatively high dose of nanoshells (10^9-10^{11} nanoshells/ml[6, 9, 15]) has been used. In such an *in vivo* setting, it is possible that with high levels of intracellular nanoshells, uniform distribution of cells containing nanoshells, and homogeneous laser fluence can be achieved. Particularly, we observed that the temperature rise in surrounding medium played a significant role. It is possible that the heat transfer in a tumor environment is limited, leading to the rapid increases in the temperature of the whole tumor tissues. This has been observed *in vivo*[12, 45, 69].

Lastly, we have also demonstrated nanoshell-mediated PTT mainly induced necrosis regardless of cellular uptake, laser fluence and total laser power input, with apoptosis induced in a fraction of cells at moderate nanoshell doses. High bulk solution temperatures often result in

necrotic cell death as reported previously. It is possible that the rapid increase of temperatures in surrounding media may contribute to the mainly necrotic cell death [58, 59]. This may not be the case in an *in vivo*. Further studies are required to elucidate the detailed mechanisms of cell death *in vivo*.

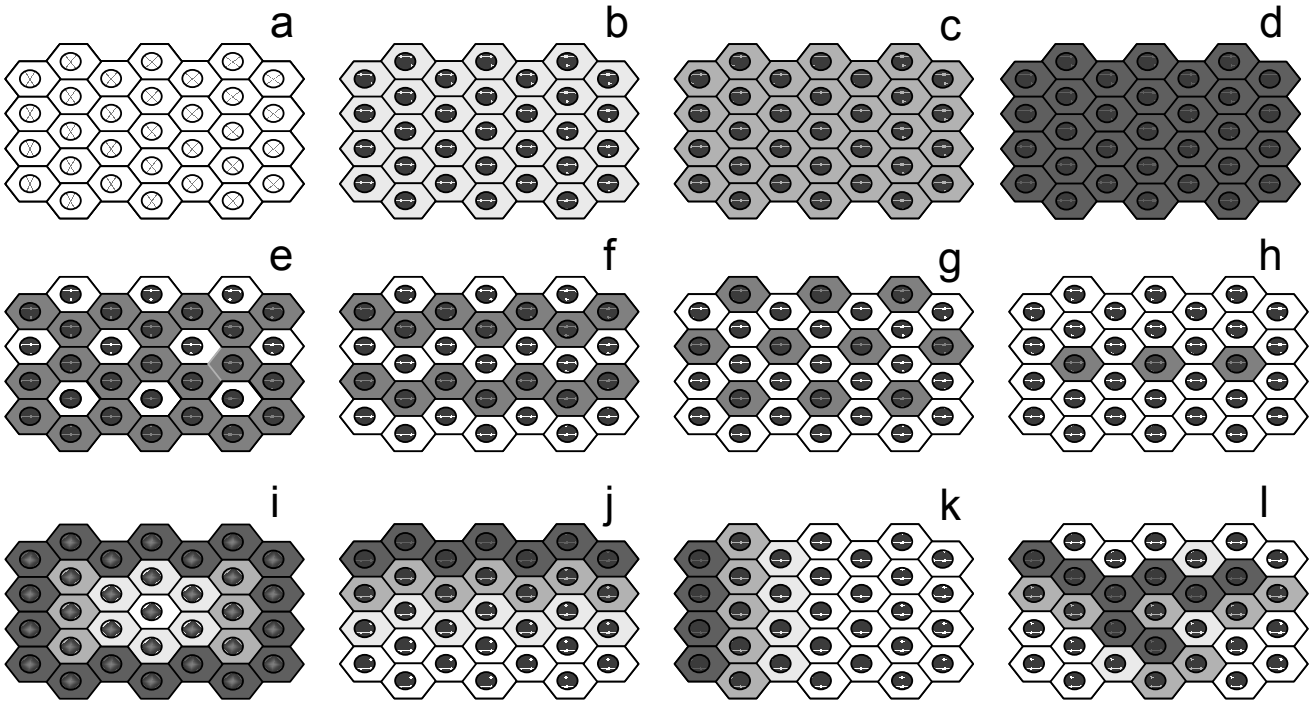

Figure 13. Schematic of theoretical nanoshell distributions in tumors. (a-d) Homogenous distribution of nanoshells at increasing concentrations. (e-h) Heterogenous distribution of nanoshells at varying ratios of treated and untreated cells. (i-l) Potential distributions observed in real tumors.

C.5 Conclusion

In this study, we have shown the effects of nanoshell dose, fluence, and treatment time on cancer cell killing *in vitro* using flow cytometry to quantify the efficacy. In addition the relative contributions of localized and overall heating on cell death were also explored, and damage to untreated cell populations was observed, having significant implications for *in vivo* experiments. We have shown the mechanism of cell death can modulated between necrosis and apoptosis which can alter the inflammatory response. This brief introductory study into the mechanisms associated with nanoshell-enabled photothermal therapy(NEPTT) cell death *in vitro* can lead to

increasingly efficient treatment strategies employed to further improve the use of nanoshell mediated-photothermal therapy for cancer treatment, and modulating the potential inflammatory response to cell death.

D. Chapter 4: Intracellular temperature modeling

D.1 Background

A new generation of nanoplasmonics derived from gold nanoparticles, including nanorods[33, 35, 70], nanocages[36, 71], and nanoshells[1, 10, 12, 42, 43], have been demonstrated as excellent candidates for photothermal therapy (PTT). Compared to spherical gold nanoparticles[72], these gold nanoparticles attract increasing attention because of their large absorption cross sections and optical resonance tunability into the near infrared (NIR) region, where tissues are the most transparent to light. A number of studies have used these gold nanoparticles to destruct cancer cells both *in vivo*[10-12, 33, 42]. Gold nanoshells have recently entered clinical trials for treating neck and head tumors[73].

Gold nanoshell-enabled photothermal therapy (NEPTT) by constant wave (cw) laser primarily relies on the elevation of the tumor temperatures[74], which shares the same concept as the traditional hypothermia. The temperature change plays multiple roles. One apparent role is to induce tumor cell death. Hyperthermia for the treatment of cancer is most commonly performed within the range of 40-45^{o}C. 43^{o}C has been considered as a critical temperature for cell death[31]. At temperatures near this threshold, cell death increases significantly, as well as often shift from apoptosis to necrosis[75, 76]. NEPTT *in vivo* occurs at much higher temperatures ($\sim$ 65 to $\sim$ 97^{o}C) within tumors and often induces necrosis[10, 12].

Complete removal or killing of tumor cells is often difficult to achieve due to the metastasis of tumors, size and anatomical location of tumor cells. The partial tumor cell death presents an opportunity for the immune system to take control of the regression and clearance of tumor cells. In order for the establishment of effective immune responses, the mode of cell death is critical. It is generally recognized that necrotic cell death can be more effective in activating the immune system than apoptotic cell death[77]. In recent years, molecular understandings of the link between the cell death and the activation of immune responses suggest that dead cells release

danger (or damage)-associated molecular patterns (DAMPs)[77]. These findings suggestion an additional role for the temperature change is to preserve or induce and to release DAMPs for signaling the immune system. In order to establish long-lasting immune responses, the temperature change is also expected to preserve tumor-associated antigens (TAAs).

Cellular components, that provide sources of DAMPs and TAAs, exhibit different sensitivity to temperatures. Membrane phase transitions begin to occur at temperatures greater than 37^{o}C, with permanent changes occurring at temperature above 41^{o}C[78, 79]. Protein denaturation within the cell can occur over a wide range of temperatures from 40 to 65^{o}C[80, 81]. Direct thermal injury of DNA and RNA require significantly higher temperatures, greater than 85^{o}C in most cases[31]. Besides their different temperature sensitivity, intracellular locations of these cellular components are distinct from each other.

Though the minimal temperature (40^{o}C) required to induce cell death has been established, this temperature is in general referred to the average temperature or sometimes the environmental temperature a cell experiences. It represents a threshold for cell death to occur[51]. It however masks the temperature cellular components are exposed to. Intracellular temperature profile at the sub-cellular level would provide a more accurate estimate of temperatures cellular components exposed to. Currently, no experimental approaches are available to measure temperature profiles during NEPTT with the subcellular resolution. Advances in the development of molecular thermometers will soon allow the direct measurement of temperature at the subcellular resolution [82]. Alternatively, the intracellular temperature profiles can be simulated computationally. Though the simulated temperature profiles are required to be validated by experimental measurements, they can shine light on the mechanisms of cell death and subsequent signaling pathways resulted from cell death (i.e. proinflammatory

and adaptive immune responses). So far, no simulated intracellular temperature profiles at a single cell level under various experimental conditions of NEPTT have been investigated yet.

The modeling of intracellular temperature distribution profiles is compounded by the intracellular distribution of nanoshells. Nanoshells are mainly localized on the cell membrane when they are modified to target a surface receptor such as stimulatory anti-HER2 antibody[83]. In some cases, nanoshells are internalized by cells. Liu and coworkers functionalized nanoshells with a peptide, AGKGTPSLETTP (A54) for targeting them to liver cancer cells[84]. They showed nanoshells were distributed throughout the cytosol. Recent studies suggest that intracellular distribution of nanoplasmonics affect the efficiency of inducing cell death and the cell death mode [85]. A number of investigators have attempted to model the intracellular heating of cells by nanoplasmonics [32, 86, 87]. The models employed in their studies did not take into account the intracellular distribution of nanoshells.

In this study, we present simulations of intracellular temperature profiles at a single cell level during NEPTT by using the finite element analysis. We modeled three scenarios that represent different pathways of intracellular trafficking and thus distributions of nanoshells. We investigated effects of two key parameters, including the nanoshell density and incident laser intensity on the intracellular temperature profiles. The results of this study can give us insights into the onset and mode of cell death and subsequent immune responses.

D.2 Research Design and Methods

Mathematical models of intracellular temperature profiles

Energy conservation was applied to each layer in which thermal properties were consistent. Assume there was no convection and radiation,

$$\frac{1}{r^2}\frac{\partial}{\partial r}\left(kr^2\frac{\partial T}{\partial r}\right)+\frac{1}{r^2\sin^2\theta}\frac{\partial}{\partial \phi}\left(k\frac{\partial T}{\partial \phi}\right)+\frac{1}{r^2\sin^2\theta}\frac{\partial}{\partial \theta}\left(k\sin\theta\frac{\partial T}{\partial \theta}\right)+\dot{Q}=\rho C_p\frac{\partial T}{\partial t} \qquad (1)$$

Additionally, heat transfer in the r-direction only was assumed,

$$\frac{1}{r^2}\frac{\partial}{\partial r}\left(kr^2\frac{\partial T}{\partial r}\right)+\dot{Q}=\rho C_p\frac{\partial T}{\partial t} \tag{2}$$

where T=T(r,t)

Mathematical models for each case were derived for each layer of the cells with corresponding cellular geometries shown in Figure 1.

Case I:

A monolayer of nanoshells was considered to coat the nucleus (Figure 1A). The heat generation was assumed to be evenly distributed within this layer. The monolayer of spheres on the surface of the nucleus was modeled as a porous layer of packed spheres, which we called the composite nanoshell layer. The thermal properties of the composite nanoshell layer was determined as described in 3.

$$\frac{1}{r^2}\frac{\partial}{\partial r}\left(k_n r^2\frac{\partial T_N}{\partial r}\right)=\rho_N C_{p,N}\frac{\partial T_N}{\partial t} \tag{3}$$

$$\frac{1}{r^2}\frac{\partial}{\partial r}\left(k_{GL} r^2\frac{\partial T_{GL}}{\partial r}\right)+\dot{Q}=\rho_{_N} C_{p,GL}\frac{\partial T_{GL}}{\partial t} \tag{4}$$

$$\frac{1}{r^2}\frac{\partial}{\partial r}\left(k_C r^2\frac{\partial T_C}{\partial r}\right)=\rho_C C_{p,C}\frac{\partial T_C}{\partial t} \tag{5}$$

$$\frac{1}{r^2}\frac{\partial}{\partial r}\left(k_E r^2\frac{\partial T_E}{\partial r}\right)=\rho_E C_{p,E}\frac{\partial T_E}{\partial t} \tag{6}$$

The initial condition at t = 0 is

$$T_N(r,0)=T_{GL}(r,0)=T_C(r,0)=T_E(r,0)=T_i$$

Where T_i is the initial environmental temperature

Assuming a semi-infinite medium, the boundary conditions are

$$\frac{\partial T_n(0,t)}{\partial r} = 0$$
$$T_n(R_N,t) = T_{GL}(R_N,t)$$
$$T_{GL}(R_{GL},t) = T_C(R_{GL},t)$$
$$T_C(R_C,t) = T_E(R_C,t)$$
$$T_E(r \to \infty,t) = T_i$$

Case II:

In this case, Au nanoshells were assumed to be homogenously distributed in the cytosol (Figure 1B). The effective thermal properties in cytosol packed with nanoshells were determined as in 3.

$$\frac{1}{r^2}\frac{\partial}{\partial r}\left(k_n r^2 \frac{\partial T_N}{\partial r}\right) = \rho_N C_{p,N} \frac{\partial T_N}{\partial t} \quad (7)$$
$$\frac{1}{r^2}\frac{\partial}{\partial r}\left(k_{GL} r^2 \frac{\partial T_{GL}}{\partial r}\right) + \dot{Q} = \rho_N C_{p,GL} \frac{\partial T_{GL}}{\partial t} \quad (8)$$
$$\frac{1}{r^2}\frac{\partial}{\partial r}\left(k_E r^2 \frac{\partial T_E}{\partial r}\right) = \rho_E C_{p,E} \frac{\partial T_E}{\partial t} \quad (9)$$

Where

The initial condition at t = 0 is

$$T_N(r,0) = T_{GL}(r,0) = T_E(r,0) = T_i$$

Where T_i is the initial environmental temperature

Assuming a semi-infinite medium, the boundary conditions are

$$\frac{\partial T_n(0,t)}{\partial r} = 0$$
$$T_n(R_N,t) = T_{GL}(R_N,t)$$
$$T_{GL}(R_N,t) = T_E(R_E,t)$$
$$T_E(r \to \infty,t) = T_i$$

Case III:

A monolayer of nanoshells was considered to coat the outer cell membrane (Figure 1C). The heat generation was assumed to be evenly distributed within this layer. The monolayer of

spheres on the surface of the membrane was modeled as a composite nanoshell layer for determining the thermal properties as below.

$$\frac{1}{r^2}\frac{\partial}{\partial r}\left(k_n r^2 \frac{\partial T_N}{\partial r}\right) = \rho_N C_{p,N} \frac{\partial T_N}{\partial t} \tag{10}$$

$$\frac{1}{r^2}\frac{\partial}{\partial r}\left(k_C r^2 \frac{\partial T_C}{\partial r}\right) = \rho_C C_{p,C} \frac{\partial T_C}{\partial t} \tag{11}$$

$$\frac{1}{r^2}\frac{\partial}{\partial r}\left(k_{GL} r^2 \frac{\partial T_{GL}}{\partial r}\right) + \dot{Q} = \rho_{GL} C_{p,GL} \frac{\partial T_{GL}}{\partial t} \tag{12}$$

$$\frac{1}{r^2}\frac{\partial}{\partial r}\left(k_E r^2 \frac{\partial T_E}{\partial r}\right) = \rho_E C_{p,E} \frac{\partial T_E}{\partial t} \tag{13}$$

Where

The initial condition at t = 0 is

$$T_N(r,0) = T_{GL}(r,0) = T_C(r,0) = T_E(r,0) = T_i$$

Where T_i is the initial environmental temperature

Assuming a semi-infinite medium, the boundary conditions are

$$\frac{\partial T_n(0,t)}{\partial r} = 0$$
$$T_n(R_N,t) = T_{GL}(R_N,t)$$
$$T_{GL}(R_{GL},t) = T_C(R_{GL},t)$$
$$T_C(R_C,t) = T_E(R_C,t)$$
$$T_E(r \to \infty,t) = T_i$$

Where:

Term	Description
T_N	Temperature within the nucleus
k_N	Thermal conductivity of the nucleus
ρ_N	Density of the nucleus
$C_{p,N}$	Heat Capacity of the nucleus
T_C	Temperature within the cytosol
k_C	Thermal conductivity of the cytosol
ρ_C	Density of the cytosol

$C_{p,C}$	Heat Capacity of the cytosol
$\dot{Q}$	The rate of volumetric heat generation by nanoshells
T_{GL}	Temperature within the composite nanoshell layer
k_{GL}	Thermal conductivity of the composite nanoshell layer
ρ_{GL}	Density of the composite nanoshell layer
$C_{p,GL}$	Heat Capacity of the composite nanoshell layer
T_E	Temperature within the extracellular space
k_E	Thermal conductivity of the extracellular space
ρ_E	Density of the extracellular space
$C_{p,E}$	Heat Capacity of the extracellular space

Rate of volumetric heat generation ($\dot{Q}$)

$\dot{Q}$ represents the total thermal heat conversion of the internalized nanoshells due to the absorption of the incident laser source. It is dependent on the absorption efficiency of Au nanoshells, nanoshell density and laser intensity. The optical properties of a group of nanoshells can differ from an individual nanoshell due to interactions between nanoparticles with close interparticle spacing [88]. The optical interference between particles was not considered in our model.

It has been theoretically shown that individual nanoparticles can be heated to high temperatures near the particle surface[89-91]. The small size relative to the volume of the embedded medium however leads to the rapid dissipation of this heat over a short distance through conduction. In this study, the converted heat from the nanoshells was assumed to be dissipated into the immediate area surrounding the nanoshells.

Therefore, the total heat generation within a uniform layer of medium or cells was calculated by summing the heat generation of individual nanoshells (eq. 14). It was assumed to be evenly distributed within each layer. The attenuation of the laser intensity due to the directionality of the incident light on a single cell was less than 1% and was not considered in this study.

$$\dot{Q} = \frac{N \times (\sigma_{abs} \cdot I)}{V_{GL}} \tag{14}$$

Where

N	Number of particles
σ_{abs}	Particle absorbance cross section [m^2]
I	Laser Intensity [W/m^2]
V_{GL}	Volume of gold nanoshell layer [m^3]

The particle cross section for nanoshells was calculated from based on theory[2, 92], and was often given in terms of the absorbance efficiency Q_{abs}, a ratio of the absorbance cross section to the geometric cross section:

$$Q_{Abs} = \frac{\sigma_{abs}}{\pi R_P^2} \tag{15}$$

The absorbance cross section σ_{abs} or the dimensionless absorbance efficiency Q_{abs} were calculated by adapting the BHCOAT program by Bohren and Huffman [93]. Details of the calculation are included in the supplemental information.

Nanoshells with a 110 nm-core and10 nm thick gold shell commonly used in *in vitro* and *in vivo* NEPTT (Table 2) were used in our model. The Q_{abs} was calculated to be ~3.0 and σ_{abs} was 4.0 $x10^{-14}$ m^2 for an individual nanoshell.

3. Effective density and thermal properties of composite nanoshell layers

The cell layers that contained nanoshells, composite nanoshell layers, were represented by a randomly packed bed of spheres with the void volume filled with cystolic fluid. The effective density and heat capacity of the composite layer were calculated based on a volume-weighted average of all the components.

$$\rho_{GL} = \frac{V_{gold}\rho_{gold} + V_{silica}\rho_{silica} + V_{void}\rho_{cytosol}}{V_{GL}} \tag{16}$$

$$C_{P,GL} = \frac{V_{gold}C_{P,gold} + V_{silica}C_{P,silica} + V_{void}C_{P,cytosol}}{V_{GL}} \tag{17}$$

The effective thermal conductivity for a bed of randomly packed spheres has been calculated previously[94, 95]. The heat resistance of thin gold shell was assumed to be negligible compared to that of the silica core. Thus, the nanoshell spheres were simplified as silica spheres for the calculation of the effective thermal conductivity:

$$k_{GL} = \frac{k_{cytosol}V_{void} + k_{silica}V_{GNS}\left[\frac{3k_{cytosol}}{2(k_{cytosol} + k_{silica}}\right]}{V_{void} + V_{GNS}\left[\frac{3k_{cytosol}}{2(k_{cytosol} + k_{silica}}\right]} \tag{18}$$

The effective thermal properties and density were calculated at each density of nanoshells (Supplemental Figure 1) and used for calculating intracellular temperature profiles.

4. Choice of parameters

Current commonly used parameters in *in vitro* NEPTT were summarized in Table 2. Based on Table 2, a range of values for nanoshell density (nanoshell/cell) and laser intensity was used to model the temperature distribution.

Case I

Nanoshells/cell: 500-3,906

Average Laser Intensity: 0.1-80 W/cm^2

Case II

Nanoshells/cell: 500-200,000

Average Laser Intensity: 0.1-80 W/cm^2

Case III

Nanoshells/cell: 500-15,000

Average Laser Intensity: 0.1-80 W/cm^2

The geometric and thermal properties of cells used in this study are summarized in Table 3.

Table 3. Geometric and thermal properties of modeled cells

	Radius, R_n [μm]	Density, ρ_n [kg/m^3]	Heat Capacity, $C_{p,n}$ [J/kgK]	Thermal Conductivity, k_n [W/mK]
Nucleus	2.5	1.05 x10^3	3.00 x10^3	0.30
Cytosol	5	1.05 x10^3	4.18 x10^3	0.59
Membrane	0.01	1.10 x10^3	2.10 x10^3	0.20
Extracellular Space	500	1.05 x10^3	4.18 x10^3	0.59

D.3 Results & Discussion

Upon the internalization by cells, the nanoshells can reside in the perinuclear region of the cell (Case I) (Figure 14A) or throughout cytosolic compartments (Case II) (Figure 14B). Nanoshells can be also situated on the cell membrane (Case III) (Figure 14C). The three cases were modeled independently to represent possible subcellular localization of nanoshells.

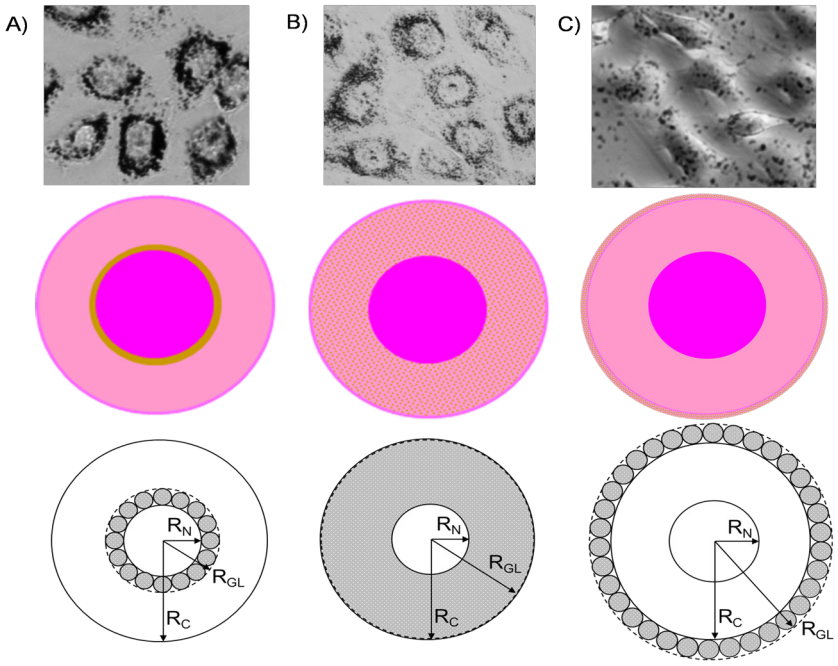

Figure 14. The modeled intracellular distribution of nanoshells. A) Perinuclear localization, B) homogenous cytosol distribution, and C) membrane accumulation. Representative images of nanoshell accumulation in cells (Top), schematics of nanoshell distribution in model cells (middle), and corresponding model geometry of model cells (bottom) were shown. The thin cell membrane layer was not included in the model due to its negligible contribution to the heat transfer.

(1) Time-resolved intracellular temperature distribution

Heating of individual nanoparticles has been shown to reach a steady state on the order of nanoseconds[91]. Heating of tissue phantoms by Au nanoshells reaches a steady state on the order of minutes[96]. 300 seconds or longer have been used for most of *in vitro* laser irradiation of tumor cells (Table 2).

We first examined the progression of the intracellular temperature change for a single cell. A quasi-steady state was reached within 0.1 second for all three cases (Figure 15A). A quasi-steady state, corresponding to a heating duration of 300 seconds, was assumed for subsequent studies.

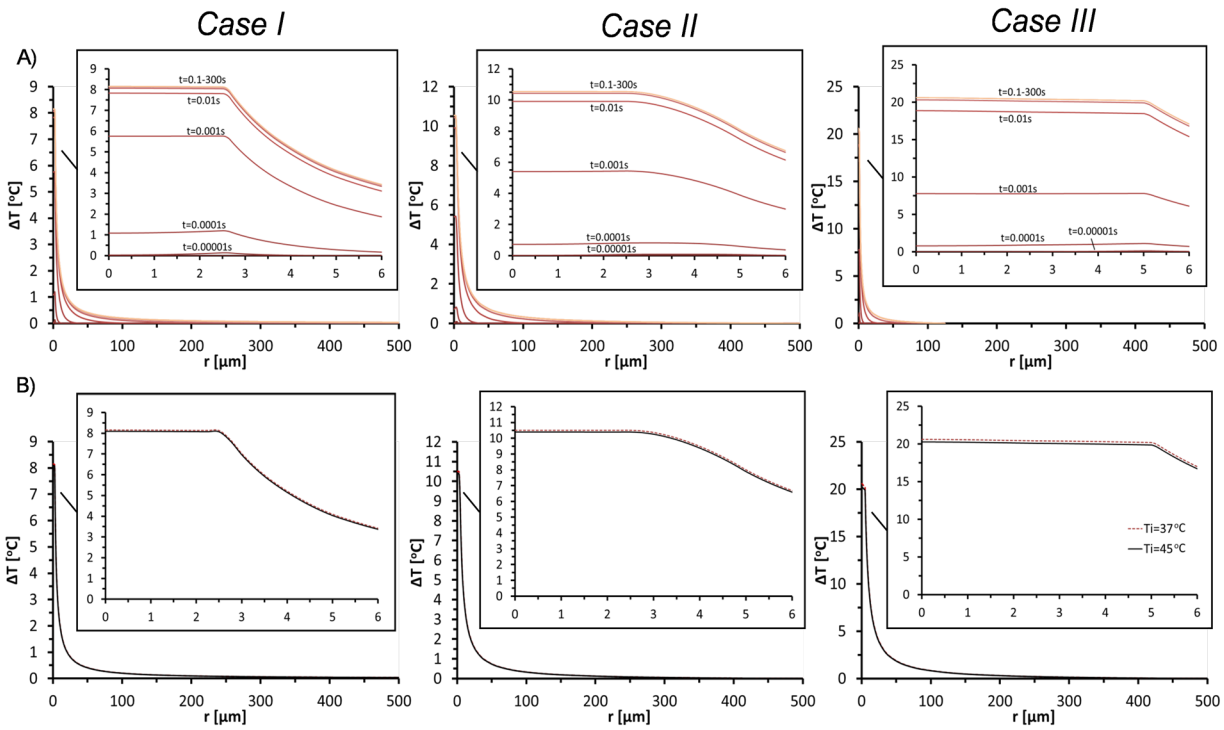

Figure 15. Validation of modeling assumptions. A) Time-dependence of the intracellular temperature change. Nanoshell-loaded cells were irradiated for the duration from 0 to 300 s. The temperatures approached steady state at 0.1 s. B) Intracellular temperature change at tissue environmental temperature (T_i) of 37°C or 45°C after 300 s – laser irradiation. Temperature change approached within 10% of the maximum change at 10 times of the cell radius. Case I at 3,906 nanoshells/cell and 80 W/cm^2, Case II at 10,000 nanoshells/cell and 80 W/cm^2, and Case III with membrane accumulation 15,000 nanoshells/cell and 80 W/cm^2 were shown.

(2) Validation of semi-infinite boundary conditions

A semi-infinite boundary condition was assumed in determining the intracellular temperature profiles. As shown in Figure 15B, the temperature change dropped to below 10% of the maximum temperature increase at a distance equal to 10 times the cell radius. The semi-infinite boundary condition can be considered to be reasonable when the density of cells that contained gold nanoshells was less than 1 million cells/cm^3, at which the interspacing between cells was larger than 20 cell radius. A 1-cm tumor often contains 10^9 cells[97]. Based on the analysis by Zaman et al.[19], 1.8 x 10^8 nanoshells were accumulated in a 1-cm tumor 1 h after the tail vein injection of 8 x 10^8/g nanoshells. In the range of nanoshell density (500 ~ 200,000 nanoshells/cell) we studied, only 450 to 0.7 million cells/cm^3 contains nanoshells. The cell density is below 1 million cells/cm^3. Some studies have shown that nanoshells are more concentrated within the tumor cortex and much less in the core of tumors [10, 98, 99]. In the cortex region, a higher density of nanoshell-containing cells is expected than we calculated. The semi-infinite boundary conditions are still reasonable by considering the high density region as a single cell with dimensions of cell aggregates. When a direct measurement of the anatomical distribution of nanoshell-containing cells in tumors is available, our models can be modified to more accurately simulate the conditions occurring *in vivo*.

(3) Consideration of the surrounding temperature of the model tumor cell

During the course of NEPTT, the environment temperature a tumor cell is exposed to is influenced by the heat generated from neighboring nanoshell-containing cells, free nanoshells residing in the extracellular space and laser. In this study, we assumed that cells that consisted of Au nanoshells were less than 1 million cells/cm^3 as discussed above, and the heating from free nanoshells in extracellular space and laser was minimal. Under our assumptions, the tissue environment temperature at 10 times of the cell radius did not affect the intracellular temperature change significantly (Figure 15B). The tissue environmental temperature was assumed to be 37^{o}C,

which indicated a tumor that was scarcely populated with Au nanoshell-containing cells (less than 1 million cells/cm^3) and that was not in close contact with laser maintained at the body temperature.

(4) Dependence of intracellular temperature profiles on the density of nanoshells and the laser intensity

The cellular uptake of nanoshells within tumor cell mass varies significantly due to the delivery means. Both the radial Gaussian distribution of the laser and the attenuation of laser intensity within the tumor mass as the function of the depth can result in a range of incident laser intensities throughout the tumor mass. The broad distribution of dimensions and interparticle interactions of nanoshells can alter their absorption characteristics. A systematic survey of a range of parameters of NEPTT facilitates our understanding of the heterogeneity of NEPTT at a single cell level and provides a framework for better design of NEPTT treatment strategies. The temperature profiles of a single cell after 300 s – laser radiation were examined at different density of nanoshells and laser intensity for all three cases. For clarity, the temperature increase at four intracellular locations, corresponding to the center of the nucleus, the perinuclear region, the center of the cytosol, and the cell membrane, is shown in detail (Figure 16 and 17).

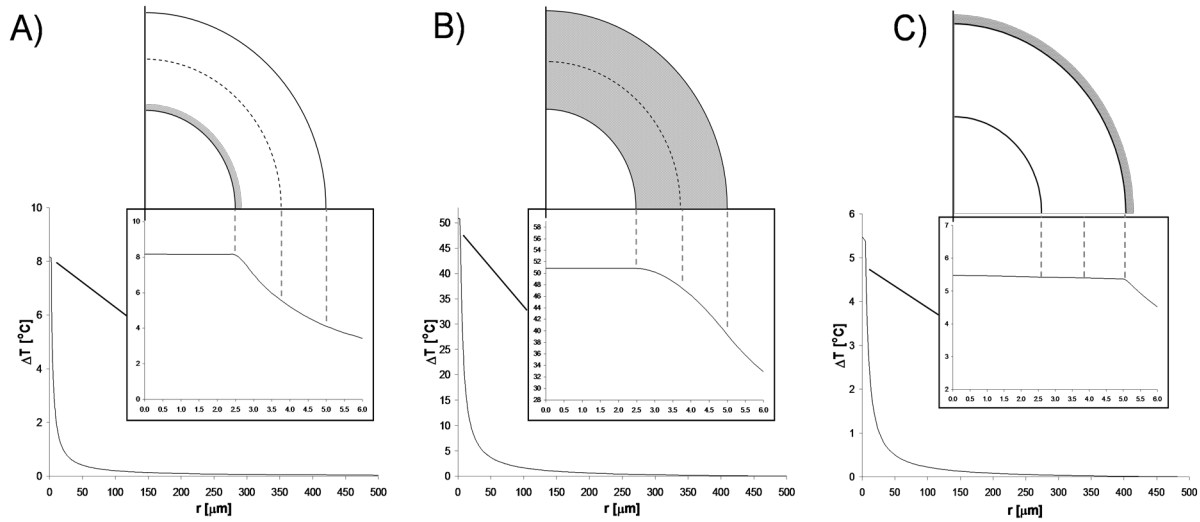

Figure 16. Representative intracellular temperature change for each case of nanoshell distribution. A) Case I at 3,906 nanoshells/cell and 80 W/cm^2, B) Case II at 50,000 nanoshells/cell and 80W/cm^2, C) Case III at 3,906 nanoshells/cell and 80W/cm^2. The four temperature points within the cell correspond to the nucleus center, perinuclear region, center of the cytosol, and cell membrane.

It is apparent that the cellular location of nanoshells significantly affected the temperature profiles at single cell level. The effects of temperature change on cell membrane, protein and DNA/RNA at three subcellular locations of nanoshells are discussed in Section (5). The effects of subcellular distribution of nanoshells on the efficiency of inducing cell death by NEPTT, the mode of cell death and the possibility of preservation or generation and release of DAMPs under different experimental conditions, which are critical for mobilizing the immune system, are discussed in Section (6 - 8).

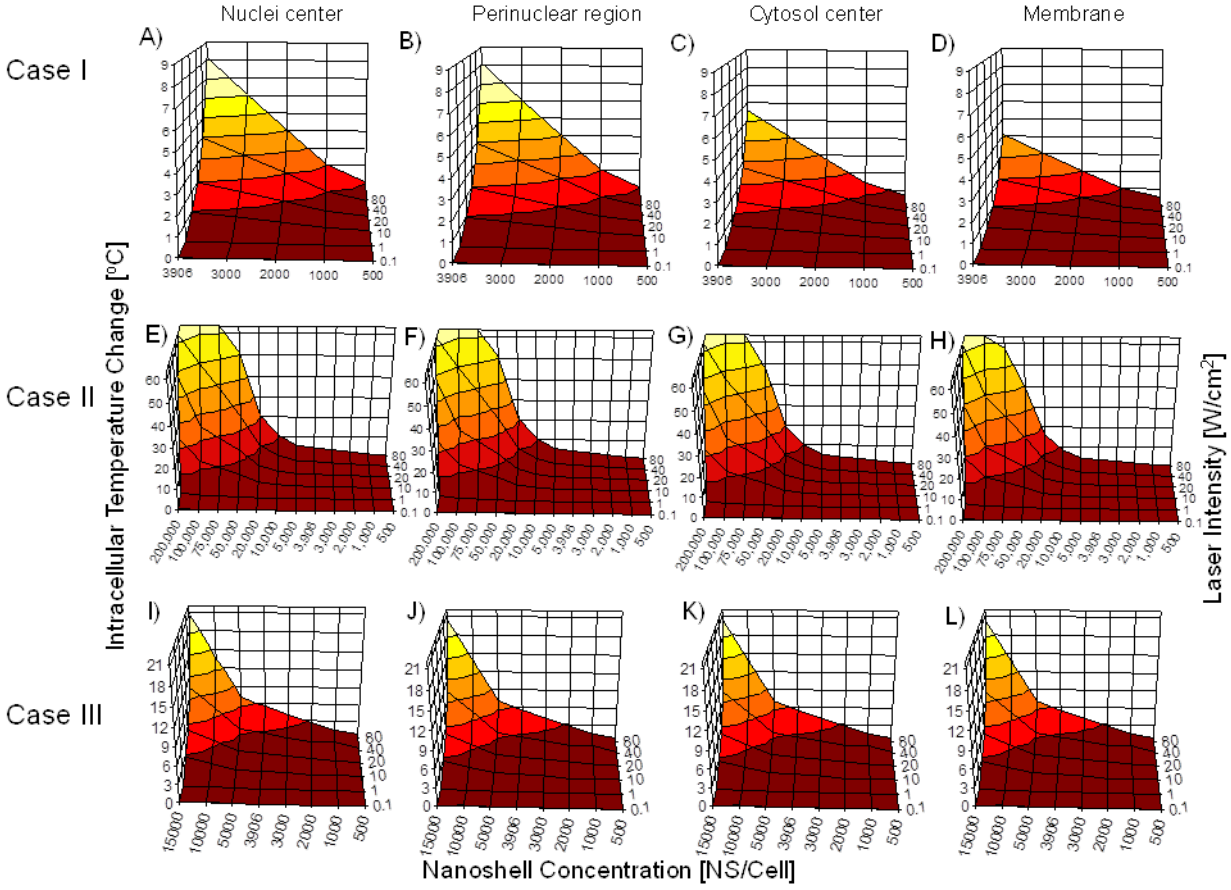

Figure 17. Temperature change for Case I in A) nucleus center, B) perinuclear region, C) center of cytosol, and D) cell membrane; for Case II in E) nucleus center, F) perinuclear region, G) center of cytosol, and H) cell membrane; for Case III in (I) nucleus center, J) perinuclear region K) center of cytosol, and L) cell membrane, for a range of nanoshell concentrations and laser intensities.

(5) Effects of subcellular distribution of nanoshells on the damage of cell membrane, protein and DNA/RNA

Cell membrane

Most cell membranes undergo irreversible transitions at a range of 41-45 ^{o}C [78, 79]. A temperature of 41 ^{o}C corresponded to temperature increase (ΔT) of 4 ^{o}C. This degree of temperature increase could only occur at the highest nanoshell concentration for Case I (Figure 17D), 3906 nanoshells/cell at 80 W/cm^2. This condition is not readily achieved experimentally. Therefore, it is highly possible that membranes maintain their integrity in Case I. For Case II (Figure 17H), where the nanoshells were distributed throughout the cytosol, the minimum number of nanoshells required to elevate the membrane temperature 4 ^{o}C was 5000 nanoshells/cell at 80 W/cm^2. Decreasing laser intensity required increasing intracellular levels of nanoshells, at the highest nanoshell concentration, 200,000 nanoshells/cell, a laser intensity of 10 W/cm^2 is required to achieve sufficient heating. It is in generally impossible to achieve 200,000 nanoshells/cell. Nevertheless, a wide range of experimental conditions can irreversibly damage membranes in Case II. For Case III (Figure 17L), where the nanoshells accumulated only on the cell membrane, membrane damage could occur at nanoshell concentrations greater than 3000 nanoshells/cell at 80W/cm^2. Completely covering the membrane with nanoshells (15,000 nanoshells/cell) would result in membrane damage at laser intensities as low as ~20 W/cm^2. Recent studies measured the density of receptors on leukemia cells, which ranges from 550 to 1300 receptors/μm^2 [100]. Based on these measurements, 180,000 to 400,000 receptors are available for the binding for our model cell. The density of nanoshells on the cell membrane is limited by the size of nanoshells. Therefore, a range of experimental conditions could irreversibly damage membranes in Case III.

Protein denaturation

Protein denaturation, including the inactivation of enzymes, membrane receptors, and ion transporters, is implicated in cell death by hyperthermia [79]. Protein denaturation occurs over a wide range of temperatures typically in excess of 40^{o}C. For proteins within the cytosol (Figure 17C, G, K), a minimum ΔT of 3^{o}C, corresponding to a temperature of 40^{o}C in Case I (Figure 17C), occurred at a minimum nanoshell concentration of between 2000 - 3000 nanoshells/cell for a laser intensity of 80 W/cm^2. It was unlikely that sufficient heating can occur at lower laser intensities for nanoshells localized within the perinuclear range (Case I) at ranges beyond a few nm into the cytosolic space. Proteins contained in the membrane might not be significantly denatured in Case I either, as the temperature decreased significantly in the cytosol to near 37^{o}C at the membrane (Figure 17D). For Case II, protein denaturation was likely to occur throughout the cytosol (Figure 17G) and within the membrane (Figure 17H) at experimentally achievable intracellular level of nanoshells and laser intensity. Proteins residing in the cytosol could denature at nanoshell concentrations higher than 3000 nanoshells/cell for an 80W/cm^2 laser intensity, while nearly 200,000 nanoshells/cell were required to sufficiently heat the cytosol at the lower laser intensity of 10W/cm^2 (Figure 17G). Membrane protein denaturation would require slightly higher nanoshell concentrations, about 4,000 nanoshells/cell at 80W/cm^2 and up to 200,000 nanoshells/cell at 10W/cm^2 (Figure 4H). Protein denaturation for Case III would occur in the cytosol and within the membrane at concentrations greater than 2,000 nanoshells/cell (Figure 17K, L). Completely covering the membrane with nanoshells (15,000 nanoshells/cell) would result in protein denaturation at laser intensities as low as ~10 W/cm^2.

Damage of DNA or RNA

More significant heating is required to cause the damage of DNA or RNA, which occurs at temperatures higher than 85^{o}C[79]. For Case I (Figure 17A) and III (Figure 17I), under no

conditions modeled in this study would DNA or RNA damage likely occurred. For Case II (Figure 4E), a ΔT of 48°C could occur when the intracellular level of nanoshells was greater than 50,000 nanoshells/cell, in which ~12.5% cytoplasmic space was filled with nanoshells, with the laser intensity of 80 W/cm^2. A minimum laser intensity of 20 W/cm^2 would be necessary at 200,000 nanoshells/cell, where the cytosol was nearly filled with nanoshells. Therefore, DNA or RNA damage could only occur in Case II at both high density of nanoshells and high laser intensity.

(6) Effect of subcellular distribution of nanoshells on the efficiency of inducing cell death

The efficiency of inducing cell death by nanoparticle enabled photothermal therapy with cw laser has been shown to depend on the intracellular localization of the nanoparticles experimentally [85, 101]. Tong et al. observed that targeting nanorods to the cell membrane (Case III) was more efficient in causing cell death by NEPTT than targeting them to the perinuclear region (Case I) under cw irradiation[101]. Huang et al. showed that gold nanoparticles distributed throughout the cytoplasm were more efficient in inducing cell death under cw laser irradiation than localized in nuclei[85]. For both studies, membrane permeability of a membrane impermeable dye was examined as an indicator of cell death. Both studies did not quantify the level of nanoparticles. In our case, the temperature change at the membrane can be used an indicator of membrane permeability. At the same level of Au nanoshells, Au nanoshells accumulated at cell membrane (Case III) were more efficient in destroying cells than in perinuclear region (Case I) and distributed throughout the cytoplasm (Case II) (Figure 17D, H, and L, Figure 18 (r = 5 μm)). The cytoplasmic space, however, could accommodate a much higher level of nanoshells, which generated higher temperature and destroyed cells more effectively at a much lower laser power. Our results agree with experimental observations and provide additional insights into how the level of nanoparticles can compound the assessment of the efficiency of cell killing by targeting nanoparticles to a given subcellular location.

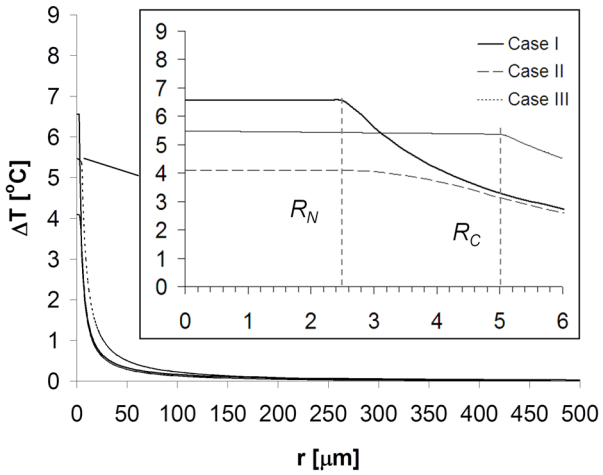

Figure 18. Effect of nanoshell distribution for equivalent nanoshell dose and laser intensity on intracellular temperature change. The simulation was performed at 3,906 nanoshells/cell and a laser intensity of 80W/cm^2. R_N indicates the nucleus size and R_C indicates the outer cell radius. Perinuclear localization of nanoshells (Case I) led to higher intracellular temperature within nuclei compared to their dispersion throughout the cytosol (Case II) or accumulation on the membrane (Case III). Case II led to higher intracellular temperature within the cytosol compared to other two cases.

(7) Effect of subcellular distribution of nanoshells on the mode of cell death

It is generally accepted that hyperthermia induces different modes of cell death depending on the temperature, often resulting in a mixed cell population of apoptotic, necrotic and viable cells at temperatures corresponding to mild hyperthermia[31]. Temperatures between 40-46 ^{o}C have been reported to induce apoptosis and temperatures above 43 ^{o}C leading to a shift to necrosis. The transition temperature is cell line-dependent [59, 75, 76, 102]. Recent experimental observations suggest that Au nanoparticles concentrated at nuclei mainly induced apoptosis under cw laser while they induce either necrosis or apoptosis when they were distributed within the cytoplasm depending on the laser power[85]. In these studies, the level of Au nanoparticles was not quantified. When Au nanoshells were concentrated in the perinuclear region (Figure 17A-D), an average temperature change of 6^{o}C within cells, corresponding to 43^{o}C, required at least 70% of coverage. We expect that 70% or more of coverage cannot be readily achieved by the majority of targeting strategies. As a result, targeting Au nanoshells to the perinuclear region likely induces apoptosis only. The cytoplasmic space permitted a higher level of Au particles than

the nuclei, which could give rise to a range of temperatures that could be either below or above 43^{o}C by varying the laser power (Figure 17C). This range of temperatures could induce either necrosis or apoptosis cell death based on the temperature criteria. Our results agree with current experimental observations. As for targeting nanoshells to the cell membranes (Figure 17L), about 30% of coverage, was required for an average temperature change of 6^{o}C. It is possible to induce either apoptosis or necrosis by many of membrane targeting strategies.

(8) Effect of subcellular distribution of nanoshells on the generation and preservation of DAMPs

A number of damage associated molecular patterns (DAMPs), including heat shock proteins (HSPs), high-mobility group box 1(HMGB1) protein, and DNA/RNA associated with the temperature increase have been identified [77]. So far few studies have reported how the subcellular location of nanoplasmonics affect the generation of DAMPs. Some other hyperthermia strategies have proposed that the generation of DAMPs is associated with the temperature cells or tissues are exposed to[103].

HSPs are upregulated in response to elevated temperatures, and can be released following cell death[79]. Due to their diverse cellular functions, HSPs are localized in a number of intracellular compartments such as the nucleus, cytosol, mitochondria, and endoplasmic reticulum[104]. HSPs are generally upregulated at mild to moderate hyperthermia (40.5-47^{o}C) but not at thermal ablation range temperatures (above 56^{o}C)[51, 105]. The release of HSPs occurs upon necrotic death[106]. As a result, only a small window of temperatures (~43-47^{o}C) at which HSP can be generated and released. All three cases of subcellular locations of Au nanoshells can potentially generate HSPs (Figure 17C, G, K). It would require careful modulation of the intracellular nanoshell level and the laser intensity to achieve significant release of HSPs into extracellular space. In Case II (Figure 17G), high nanoshell concentrations within the cytoplasm

combined with moderate to high laser intensities led to temperatures in the range of thermal ablation which may suppress the generation of HSPs. In Case I (Figure 17C), more than 70% coverage of perinuclear region was required for necrosis to occur. It is likely that the intracellular HSPs cannot be released into the extracellular space for activating the immune system in this case. One promising strategy would be a two-phase photothermal therapy, involving an initial moderate temperature increase to promote the upregulation of HSPs followed by an ablative temperature to induce necrotic cell death and cell rupture to release the intracellular HSPs.

HMGB1 is located within the nuclear compartment and secreted from necrotic cells. Increasing levels of HMGB1 have been shown to be released into the extracellular space following heating at increasing temperature from 43.7^{o}C to 56^{o}C [107]. Based on our simulated results, a low level of HMGB1 was expected to be detected in the extracellular space when nanoshells were accumulated at perinuclear region alone (Figure 17A). In contrast, effectively targeting Au nanoshells to the cytosolic space (Figure 17E) or the cell membrane (Figure 17I) make it possible to achieve temperatures above 50^{o}C and release a significant level of HMGB1.

DNA/RNA are localized in the nucleus and the cytosolic space. It has been shown that DNA and RNA are released into the extracellular space and act as a DAMP when cells undergo necrotic cell death[77]. Cells exposed to a range of temperatures from 50 to 90^{o}C can generate DNA fragments in response to thermal injury[108]. Based on our simulation results, when nanoshells were accumulated in the cytosolic space (Figure 17E), temperatures in the 50-90^{o}C could be reached for a number of nanoshell concentrations and laser intensity combinations but would be nearly impossible when nanoshells were accumulated in perinuclear region (Figure 17A). The release and immunogenicity of these DNA fragments requires further studies.

(9) Limitations of our current model

In our current model, we made a few assumptions. First, we did not consider cell morphologies other than spheres (Figure 14). Second, we did not consider the effect of density of nanoshells on the absorption efficiency of individual nanoshells. When the density of nanoshells increases, the interspacing between nanoshells decreases and the absorption efficiency of individual nanoshell decreases. The dependence of absorption efficiency on the interspacing of nanoshells was predicted by Liu et al[88]. Based on their results, the total heat generation was not linearly dependent on the nanoshell density as used in the current model (eq. 14). Our current model over-estimated the temperature change for the same nanoshell density. In order to achieve the same temperature at a given intracellular location, a higher laser intensity than predicated in the current model was needed. Third, we assumed that nanoshells were uniformly localized in cytosol , perinuclear region, or cell membrane (Figure 14). It is most likely that nanoshells are heterogeneously accumulated in a number of subcellular locations.

While the model we developed had many simplifications, our conclusions are in agreement with available experimental observations. A survey of a range of Au nanoshells and laser powers helped to clarify some experimental observations and provided possible strategies for the optimal treatment by NEPTT. We used gold nanoshells as our model system. The major difference between different nanoplasmonics is the absorption efficiency. Our current model can be easily adapted to assess the intracellular temperature profiles induced by other nanoplasmonics. The intracellular temperature profiles at a single cell level provide us with a microscopic understanding of the effects of subcellular location of Au nanoshells on the onset and mode of cell death and the generation and release of DAMPs.

D.4 Conclusion

Theoretical cases presented here represent a range of conditions possible during actual treatment. Nanoshell uptake within a population of cells will vary significantly due to delivery both *in vitro* and *in vivo*. Both the radial Gaussian distribution of the laser, and the attenuation within the medium as function of depth will result in a range of incident laser intensities throughout the mass. The nanoshells synthesized will not be perfectly monodispersed, with slight variation in absorption efficiency, as well as interparticle interactions that can alter their absorption characteristics. These variations can lead to a wide range of intracellular temperatures within the population of cells treated. The simulations performed in this study can provide insight into optimizing the conditions for efficient intracellular heating for a significant portion of cells to be treated.

D.5 Supplemental Information

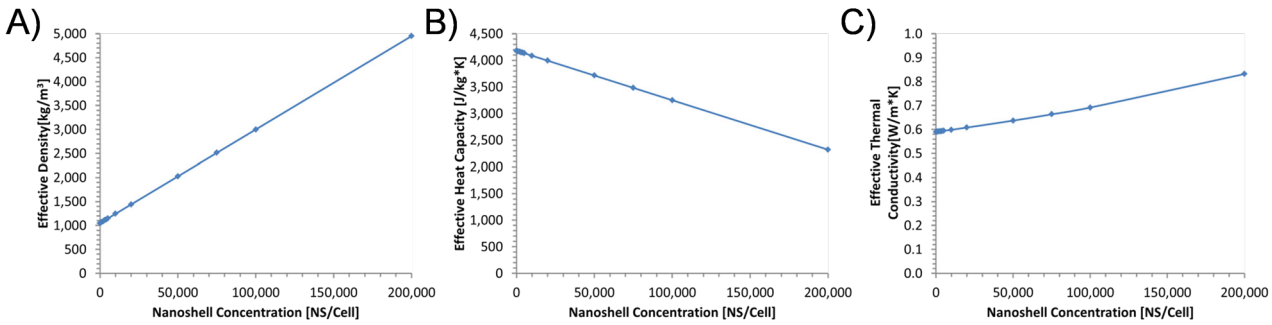

Figure 19. Effective thermal properties of the gold layer used throughout the simulations. Effective density (A), heat capacity (B), and thermal conductivity (C).

Calculation of σ_{abs} and Q_{abs}

The absorbance cross section σ_{abs} or the dimensionless absorbance efficiency Q_{abs} were calculated based on the BHCOAT program by Bohren and Huffman [93] . Briefly, a coated sphere with inner radius a and outer radius b was exposed to an incident electromagnetic field (E_i, H_i) that was polarized in the x plane in an isotropic, homogenous medium. The electromagnetic field was expanded into an infinite series of vector spherical harmonics

$$E_i = E_o \sum_{n=1}^{\infty} i^n \frac{2n+1}{n(n+1)} [M_{o1n}^{(1)} - iN_{e1n}^{(1)}] \quad \text{(S1)}$$

$$H_i = \frac{-k}{\omega\mu} E_o \sum_{n=1}^{\infty} i^n \frac{2n+1}{n(n+1)} [M_{e1n}^{(1)} + iN_{o1n}^{(1)}] \quad \text{(S2)}$$

The electromagnetic fields within the core and shell regions, as well as scattered away from the particle were written as

$$E_1 = \sum_{n=1}^{\infty} E_n[c_n M_{o1n}^{(1)} - id_n N_{e1n}^{(1)}] \tag{S3}$$

$$H_1 = \frac{-k_1}{\omega\mu_1} \sum_{n=1}^{\infty} E_n[d_n M_{e1n}^{(1)} + ic_n N_{o1n}^{(1)}] \tag{S4}$$

$$E_2 = \sum_{n=1}^{\infty} E_n[f_n M_{o1n}^{(1)} - ig_n N_{e1n}^{(1)} + v_n M_{o1n}^{(2)} - iw_n N_{e1n}^{(2)}] \tag{S5}$$

$$H_2 = \frac{-k_2}{\omega\mu_2} \sum_{n=1}^{\infty} E_n[g_n M_{e1n}^{(1)} + if_n N_{o1n}^{(1)} + w_n M_{e1n}^{(2)} + iv_n N_{o1n}^{(2)}] \tag{S6}$$

$$E_s = \sum_{n=1}^{\infty} E_n[ia_n M_{e1n}^{(3)} - b_n M_{o1n}^{(3)}] \tag{S7}$$

$$H_s = \frac{-k}{\omega\mu} \sum_{n=1}^{\infty} E_n[ib_n N_{o1n}^{(3)} + a_n M_{o1n}^{(3)}] \tag{S8}$$

Where

$$E_n = i^n E_o \frac{2n+1}{n(n+1)}$$

$$a_n = \frac{\psi_n(y)[\psi'_n(m_2 y) - A_n \chi'_n(m_2 y)] - m_2 \psi'_n(y)[\psi_n(m_2 y) - A_n \chi_n(m_2 y)]}{\xi_n(y)[\psi'_n(m_2 y) - A_n \chi'_n(m_2 y)] - m_2 \xi'_n(y)[\psi_n(m_2 y) - A_n \chi_n(m_2 y)]} \tag{S9}$$

$$b_n = \frac{m_2 \psi_n(y)[\psi'_n(m_2 y) - B_n \chi'_n(m_2 y)] - \psi'_n(y)[\psi_n(m_2 y) - B_n \chi_n(m_2 y)]}{m_2 \xi_n(y)[\psi'_n(m_2 y) - B_n \chi'_n(m_2 y)] - \xi'_n(y)[\psi_n(m_2 y) - B_n \chi_n(m_2 y)]} \tag{S10}$$

$$A_n = \frac{m_2 \psi_n(m_2 x)\psi'_n(m_1 x) - m_1 \psi'_n(m_2 x)\psi_n(m_1 x)}{m_2 \chi'_n(m_2 x)\psi'_n(m_1 x) - m_1 \chi'_n(m_2 x)\psi_n(m_1 x)} \tag{S11}$$

$$B_n = \frac{m_2 \psi_n(m_1 x)\psi'_n(m_2 x) - m_1 \psi_n(m_2 x)\psi'_n(m_1 x)}{m_2 \chi'_n(m_2 x)\psi_n(m_1 x) - m_1 \psi'_n(m_1 x)\chi_n(m_2 x)} \tag{S12}$$

where

$$x = \frac{2\pi a N}{\lambda}, y = \frac{2\pi b N}{\lambda}$$

and ψ, χ, ξ are the Reccati-Bessel functions where

$$\psi_n(\rho) = \rho j_n(\rho),\ \chi_n = -\rho j_n(\rho),\ \xi_n(\rho) = \rho h_n^{(1)}(\rho)$$
$$h_n^{(1)}(\rho) = j_n(\rho) + i y_n(\rho)$$

N: Refractive index of the medium
a: radius of core
b: radius of shell
λ: wavelength of incident light
m_1: refractive index of the core relative to the surrounding medium
m_2: refractive index of the shell relative to the surrounding medium

The absorption coefficient can be calculated from the extinction and scattering coefficients.

$$\sigma_{ext} = \frac{2\pi}{k^2}\sum_{n=1}^{\infty}(2n+1)\,\mathrm{Re}\{a_n + b_n\} \tag{S13}$$

$$\sigma_{sca} = \frac{2\pi}{k^2}\sum_{n=1}^{\infty}(2n+1)\left(|a_n|^2 + |b_n|^2\right) \tag{S14}$$

where

$k = y / b$

$$Q_{ext} = \frac{\sigma_{ext}}{\pi b^2} \tag{S15}$$

$$Q_{sca} = \frac{\sigma_{sca}}{\pi b^2} \tag{S16}$$

$$Q_{abs} = Q_{ext} - Q_{sca} \tag{S17}$$

E. Chapter 5: *In vitro* inflammatory response

E.1 Background

Significant progress in the development of nanoplasmonics with the high efficiency of energy conversion from near-infrared light (NIR) to heat has instigated recent advances in photothermal therapy for cancer treatment.[37, 69, 109] The efficacy of nanoplasmonics-enabled thermal ablation of tumor cells, particularly those based on gold nanoshell/silica cores, termed nanoshell enabled photothermal therapy (NEPTT), has been demonstrated both *in vitro* and *in vivo.*[4-12]

One of the key roles of the immune system is to clear dying cells in the body and generate the appropriate response to the dying cells or their cellular components. Programmed cell death, or apoptosis, of cells during normal homeostasis is generally considered not to elicit inflammation or an immune response, which would otherwise result in autoimmunity.[77] Cell death can lead to an immunogenic response when they undergo specific forms of necrosis or stress that result in the preservation and release of various danger-associated molecular patterns (DAMPs).[22]

The immune system recognizes DAMPs through a series of receptors either on the surface or within the cytoplasm of cells. Some of the toll like receptors (TLRs) that mainly recognize pathogen-associated molecular patterns (PAMPs), have been shown to detect DAMPs. TLR2 and 4 recognize high mobility group box 1(HMGB1) protein,[110, 111] hyaluronan and biglycan,[22, 112-114] and heat shock proteins (HSPs).[115, 116] The stimulation of TLR2 and 4 can induce the production of pro-IL-1β and pro-IL-18 that can be cleaved into the active secreted form by the caspase-1 complex associated with the activation of inflammasome complexes.[117]

The other group of receptors implicated in sensing cell death and injury are the NOD-like receptors (NLRs). Some NLRs, such as NLRP1, NLRC4, and AIM2 inflammasome, primarily involve pathogen recognition.[117-119] The NALP3 inflammasome has been shown to be activated by a

wide range of pathogen associated danger signals as well as DAMPs. The DAMPs that can activate the NALP3 inflammasome include extracellular ATP,[22, 120, 121] ADP, AMP,[122] uric acid and monosodium urate (MSU) crystals.[123-125] Uric acid released from dying cells has been shown to crystallize into monosodium urate (MSU) in the extracellular environment due to the presence of high levels of sodium ions.[125, 126] Iyer and colleagues also suggest that actively-respiring mitochondria that are released from necrotic cells can activate the NALP3 inflmmasome possibly through the generation ATP.[22]

Inflammasomes form high molecular weight complexes that activate caspase-1 to cleave precursors of proinflammatory cytokines, such as IL-1β and IL-18.[127] The generation of IL-1β, a potent proinflammatory cytokine, is believed to be the key mediator in the generation of a cascade of immune responses.[128] It can recruit neutrophils[22, 129] and other inflammatory cells[128] to the site of injury, promote the maturation of dendritic cells (DCs),[120] prime $CD8^+$ T-cells,[130] induce the differentiation of type 17 T-helper cells,[131] and stimulate the production of various downstream molecules such as nitric oxide(NO) and proinflammatory cytokines such as IL-6 and IL-12.[132] Activation of the inflammasome complexes has been shown to be required for the development of adaptive immune responses against tumors.[130]

Recently, cancer therapies that combine cell killing with the induction of a strong immune response against dying tumor cells have been shown to increase therapeutic efficacy in the clearance and regression of cancers.[133, 134] The induction of immune responses to tumor cells during combined therapies involves the generation of DAMPs by the treatments and the stimulation of the innate immune sensors by DAMPs, followed by the recognition and presentation of tumor associated antigens (TAAs) to T cells by antigen presenting cells (i.e. DCs) for the establishment of TAA-specific immune responses.[120]

Towards the goal of eradicating and preventing the recurrence of tumors, an important question for the development of nanoplasmonics remains to be addressed: does nanoplasmonic-enabled photothermal therapy simply perform a microsurgery, which only removes the tumor mass, or can it also mobilize immune responses against tumors? In this study, we show that NEPTT, under commonly-used experimental conditions, induced necrotic cell death. Subsequently, we assessed whether DAMPs released from NEPTT-treated cells stimulated inflammasome complexes and whether they were able to activated macrophages for the generation of pro-inflammatory cytokines, i.e. IL-1β. Our results provide critical insights into the development of nanoplasmonics for combining photothermal therapy and immunotherapy to treat cancers.

E.2 Research Design and Methods

Cell Culture

TC-1 cells (ATCC) were maintained in Roswell Park Memorial Institute (RPMI) 1640 media supplemented with 10% fetal bovine serum (FBS), 2 mM L-glutamine, 1mM sodium pyruvate, 10 mM (4-(2-hydroxyethyl)-1-piperazineethanesulfonic acid)(HEPES), 1.5 g/L sodium bicarbonate and 4.5 g/L glucose. 9L gliosarcoma rat cells (ATCC), B16 melanoma (ATCC), and J774A.1 mouse macrophage cells (ATCC) were maintained in Dulbecco's Modified Eagle medium (DMEM) containing 10% fetal bovine serum (FBS), 1% Penicillin-Streptomycin, 4 mM L-glutamine, and 1 mM sodium pyruvate at 37^{o}C and 5% CO_2. Hela cells (ATCC) were maintained in MEM media supplemented with 10% FBS, 1% Penicillin-Streptomycin, 2 mM L-glutamine, and 1 mM sodium pyruvate at 37^{o}C and 5% CO_2. THP-1 cells were maintained in RPMI 1640 supplemented with 10% FBS, 2 mM L-glutamine, 1 mM sodium pyruvate, 10 mM HEPES, 50 μM 2-mercaptoethanol,1.5 g/L glucose. All the cells were maintained at 37^{o}C and 5% CO_2.

Gold Nanoshell Enabled Photothermal Therapy

TC-1, B16, and J774A.1 cells at 6x10^4 cells/well were plated in flat bottom 24 well plates and allowed to adhere for 24 h. Au nanoshells were collected by centrifugation and re-dispersed in FBS-free cell culture media, and diluted to the designated concentrations. Cells were incubated with 500 μl of Au nanoshell solutions for 4 h. Cells were then rinsed with Dulbecco's phosphate-buffered saline (DPBS) three times to remove unbound Au nanoshells prior to the laser irradiation. 9L cells were plated at 3x10^4 cells/well in flat bottom 96 well plates incubated with 100 μl of Au nanoshell solutions for 4 h. Cells were imaged under a bright-field microscope (Nikon Eclipse TE2000-U) with a CCD camera (Photometrics Coolsnap ES) to confirm Au nanoshell internalization. Images were taken at the same exposure level and magnification for all samples.

Cells were detached with 0.05% trypsin-EDTA and re-suspended in 100 µl of DPBS. Cells were irradiated in a well of 96-well plate using a diode laser (Newport Corporation, 808nm, 23W/cm^2 max), which was positioned to illuminate the full area of the well of the 96-well plate. Immediately following the irradiation, the temperature of the solution in the well was measured. The cells obtained from two wells were combined for further analysis and the stimulation of macrophages.

Other means of inducing necrosis, including the incubation of cells in a 70^{o}C water bath for 5 minutes, and 3 cycles of freeze-thaw, were used as controls.

Analysis of Cell Death by Flow Cytometry

The apoptosis assay kit (Annexin V, BD Biosciences) was used for the assessment of cell viability and mode of cell death using flow cytometry. The laser-irradiated cells and controls were washed 2 times with cold phosphate buffered saline (PBS) and then re-suspended in the binding buffer. Cells were stained with 5 µ85l each of the Annexin V-FITC and 7-AAD dyes and incubated for 15 min prior to FACS analysis. The samples were analyzed within one hour using a BD FACScan (Cell Analysis Facility, University of Washington). Apoptotic cells were positive for the Annexin V-FITC dye, while the necrotic cells were positive for both the Annexin V-FITC and 7-AAD. Viable cells were negative for both dyes.

Stimulation of macrophages

J774A.1 cells were initially primed in 24 well plates with 2 µg/ml lipopolysaccharide (LPS) from Escherichia coli 0111:B4 (Sigma) for 24 h. THP-1 cells were first differentiated into macrophages using 500 nM phorbol-12-myristate-13-acetate (PMA) for 6 hours, followed by priming with 2 µg/ml LPS for 8 hours. The primed J774A.1 and THP-1 cells were washed once with DPBS followed by the culture media. Then they were stimulated with fractions of cells subjected to NEPTT, 2 mM ATP in DPBS, or 1 mg/ml Min-U-Sil 15 silica crystals in DPBS. J774A.1

cells and THP-1 cells with and without LPS priming were stimulated with cell culture media containing DPBS as negative controls to determine the background level of IL-1β. LPS primed macrophages were stimulated with 0-2 mM ATP, 0-10 mM ADP, and 0-100 μM MSU crystals to determine the concentration required to activate the inflammasome complex for those DAMPs.

ATP Quantification

ATP levels released from NEPTT-treated and untreated cells were quantified using a Promega Enliten ATP assay (Promega Corp.). The samples were diluted serially up to the concentration range suitable for the assay. Luciferase enzyme solution was mixed quickly with diluted samples at a 1:1 ratio in an opaque white Costar 96-well plate with low background luminescence. The luminescence was measured by a Spectramax M5 plate reader. Luminescence from all wavelengths was collected over a 1000 ms-integration time. At least three separate measurements at each dilution within the assay range were taken. The concentration of each sample was determined by averaging the values obtained from three dilutions.

ADP Quantification

ADP levels released from NEPTT-treated and untreated cells were quantified using a Transcreener ADP^2 FI Assay (Bellbrook Labs). Samples were diluted serially up to the concentration range suitable for the assay. ADP^2 Antibody-IRDye QC-1 was mixed with diluted samples at 1:1 ratio to a final volume of 50 μl and a final dye concentration of 4 nM in an opaque black 96-well plate. The fluorescence intensity was measured by a Spectramax M5 plate reader with an excitation wavelength of 590 nm and an emission wavelength of 617 nm.

Uric Acid Quantification

Levels of uric acid in the supernatants from NEPTT- and un- treated cells were quantified using both the uricase enzyme and the Ampliflu Red peroxidase reagent (Sigma-Aldrich) using a protocol based on the method used by Gasse and collegues.[135] Uricase converts the uric acid

into allantoin, hydrogen peroxide, and carbon dioxide. Hydrogen peroxide in the presence of horseradish peroxidase (HRP) reacts with the Ampliflu Red reagent to produce the fluorescent product resorufin. Supernatants were diluted two times in 0.1 ml Tris-HCl and mixed with an equal part of a reaction solution containing 100 μM Amplifu Red reagent, 0.4 U/ml HRP, and 0.4 U/ml uricase. Fluorescence intensity was measured by a Spectramax M5 plate reader with an excitation wavelength of 540 nm and an emission wavelength of 590 nm.

Enzyme-linked Immunosorbent Assay (ELISA)

The level of IL-1β secreted by macrophages was assessed by ELISA. For the J774A.1 IL-1β quantification, anti-mouse/rat IL-1β was used as the capture antibody (clone B122) and biotinylated polyclonal rabbit anti-mouse IL-1β antibody (polyclonal) was used as the detection antibody. For THP-1 IL-1β quantification, anti-human IL-1β (clone CRM56) was used as the capture antibody and biotinylated mouse anti-human IL-1β antibody (clone CRM57) was used as the detection antibody. Samples were diluted at a proper range with blocking buffer (1% FBS/PBS). The detection range for IL-1β was 8 - 2000 pg/ml. Standard procedures described in eBioscience protocol literature (eBioscience San Diego, CA) were used.

Dendritic Cell Maturation

BC-1 mouse dendritic cells were stimulated with Au nanoshell-treated B16 cells for 48 hours prior to flow cytometric (BD Biosciences FACSCan). Cells were washed 3 times in DPBS prior to nonspecific site blocking with FC block (2μg/ml purified rat anti-mouse CD16/32) for 15 minutes on ice. Cells were then stained with 0.05 μg/ml anti-mouse FITC-conjugated CD-86 and 0.05 μg/ml anti-mouse PE conjugated MHCII for 30 minutes at 4^{o}C. The cells were then washed 3 times prior to being re-dispersed in 200 μl of FACs buffer containing 7-AAD. The samples were analyzed within one hour. BC-1 cells treated with 1 ng/ml LPS were used as a positive control for maturation.

Statistics

All results are representative of at least two sets of independent experiments, with samples performed in duplicates or triplicates. Results represent average values with error bars representing ± the standard deviation (SD) of the samples.

E.3 Results

Stimulation of inflammasome complexes by cellular components released from NEPTT-treated cells

Recent studies suggest that cellular components released from dead cells either by chemotherapeutic drugs,[120] pressure-disruption,[22] or complement-mediated lysis[22] stimulate inflammasomes but not by UV irradiation or freeze-thaw cycles.[22, 130] We then examined whether cellular components from NEPTT-treated cells would trigger inflammasomes. In this study, a mouse macrophage cell line, J744A.1, and a human macrophage cell line, THP-1, were used. J744A.1 and THP-1 have been well characterized as cell lines that respond to a variety of well-documented inflammasome-inducers.[136-138] J744A.1 and THP-1 cells were first treated with lipopolysaccharide (LPS) to induce pro-IL-1β. Upon the stimulation of inflammasomes, pro-IL-1β is cleaved into IL-1β which is secreted from cells. The stimulation of inflammasomes was therefore characterized by the secretion of IL-1βin J744A.1 and THP-1 cells.

B16 cells loaded with various doses of Au nanoshells were irradiated and separated into secreted, nuclear and mitochondrial fractions. Initially, all the fractions were tested for the activation of inflammasomes. None of the fractions induced IL-1β secretions in both macrophage cell lines (data not shown). Subsequently, only secreted fractions were used to test the effect of Au nanoshell concentration and the ratio of dead cells to macrophages. Regardless of the concentrations of Au nanoshells, secreted fractions from dead cells did not induce a significantly higher level of IL-1β in macrophages compared to untreated cells (*Figure 20A*). Higher ratios of dead cells to macrophages did not activate inflammasomes either (*Figure 20B*).

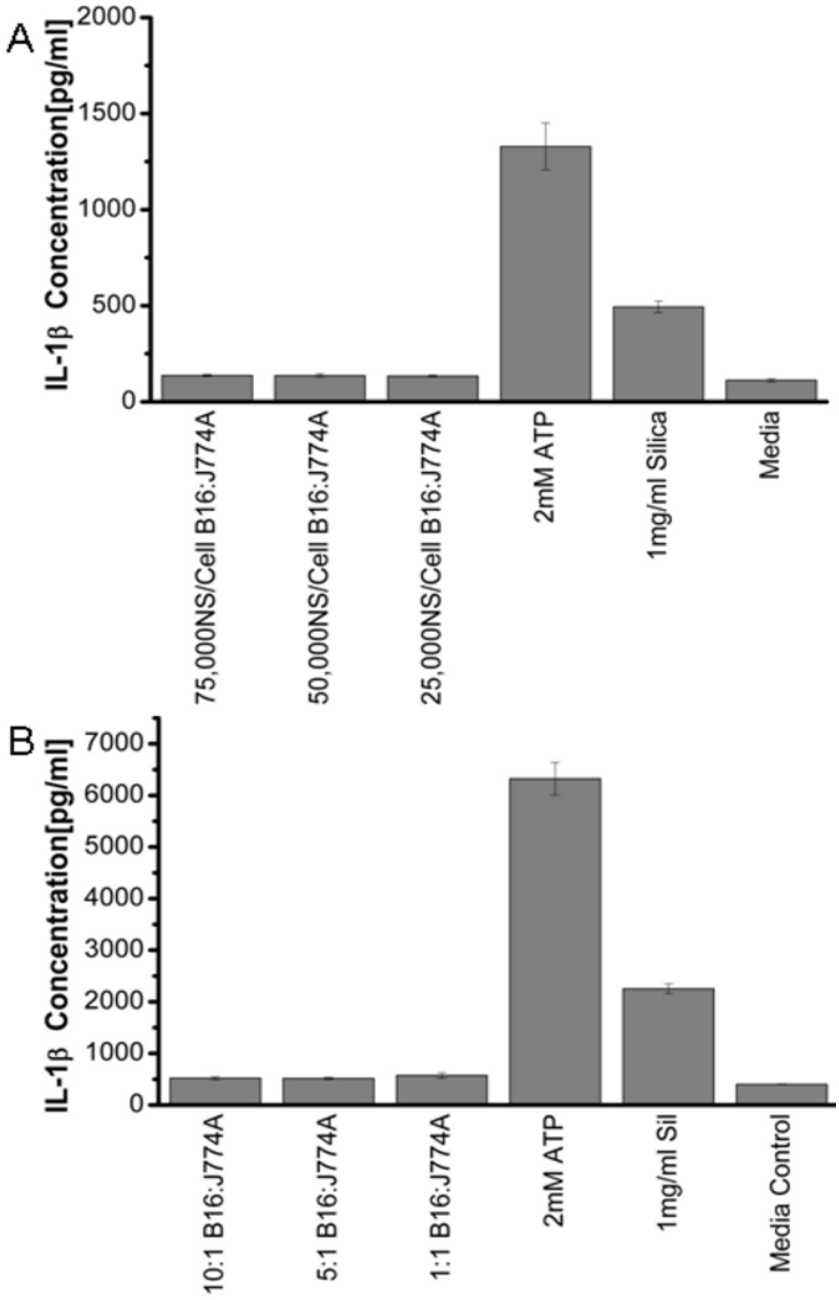

Figure 20. The stimulation of inflammasomes by NEPTT treated cells are not affected by the dose of gold nanoshells or the cell supernatant concentration. (A) J774A.1 macrophage cells were stimulated with supernatant fractions collected from treated B16 cells. A ratio of B16 to J774A.1 of 10:1 was used. (B) J774A.1 macrophage cells were stimulated with supernatant fractions collected from treated B16 cells at a ratio of B16 to J774A.1 of 10:1-1:1 for a gold nanoshell dosing concentration of 75,000 nanoshells/cell. IL-1β secreted by stimulated macrophages were collected after 24 h and quantified by ELISA. 2 mM ATP and 1 mg/ml Min-U-Sil 15 silica particles were used as positive controls for inflammasome activation. DPBS was used as a negative control. Values are mean ± SD. Experiments are representative of at least two independent experiments.

Macrophages in the absence of LPS pre-treatment also did not generate IL-1β. In order to confirm our results from B16 tumor cells, a number of other tumor cell lines derived from either mouse or human tissues were tested for their ability of stimulating inflammasomes. None of these cell lines tested activated the inflammasome complexes to produce IL-1β (*Figure 21*).

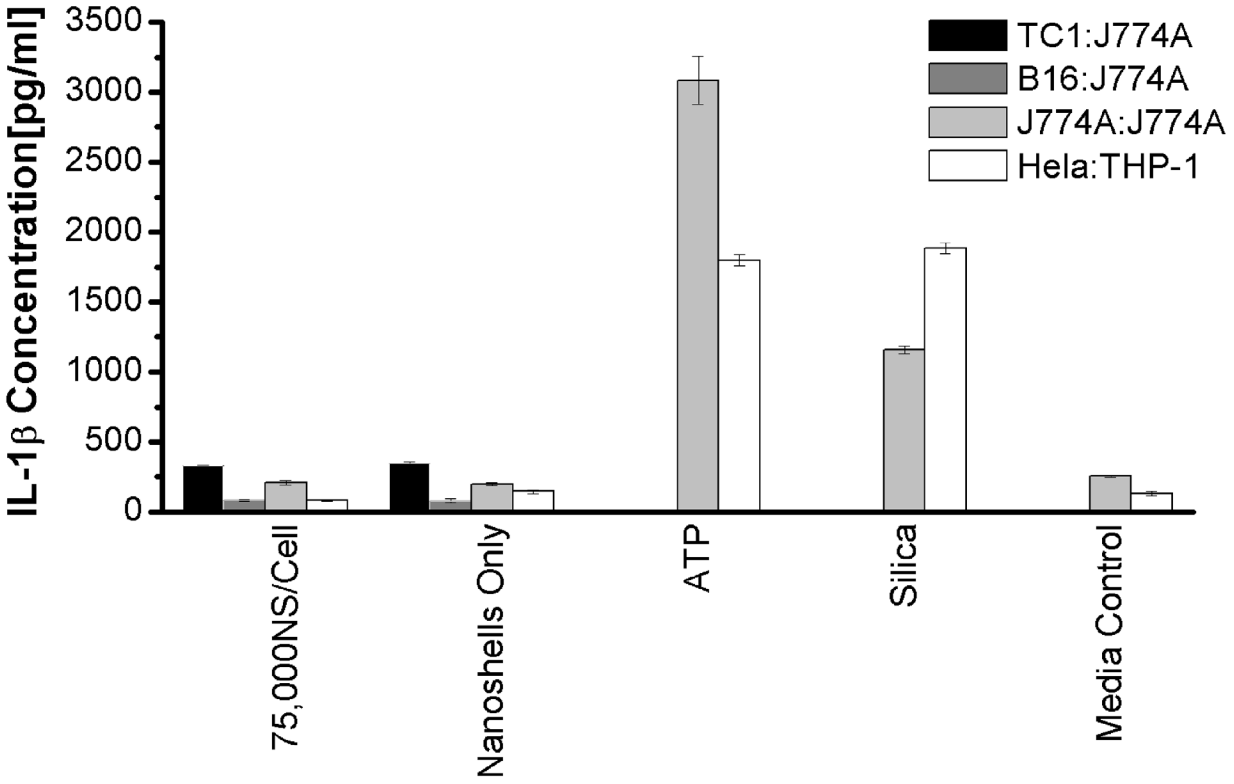

Figure 21. Inflammasome activation by NEPTT is not cell line dependant. Two macrophage cell lines were stimulated with supernatant fractions collected from treated cells at a ratio of 1:1 for gold nanoshell dosing concentrations of 75,000 nanoshells/cell. Three murine cell lines, TC1, B16, and J774A.1 were used to stimulate J774A.1 macrophages, with human Hela cells used to stimulate THP-1 macrophage cells. DPBS treated with NEPTT in the absence of cells was used as a negative control. 2mM ATP and 1 mg/ml Min-U-Sil 15 silica were used as positive controls. IL-1β secreted by macrophages were collected after 24 h and quantified by ELISA. Values are mean ± SD. Experiments are representative of at least two independent experiments.

Quantification of ATP, ADP and Monosodium Urate (MSU) released from NEPTT-treated cells

We next quantified the levels of major DAMPs, including ATP, ADP and MSU, that have been suggested to be responsible for the stimulation of inflammasomes by necrotic cells.[22, 122, 125] The level of ATP released from NEPTT-treated cells is about 0.004 mM and significantly higher than untreated cells ($p < 0.05$) (*Figure 22A*). However, 0.5-5 mM ATP was required to activate inflammasomes and induce IL-1β secretion alone (*Figure 22B*). Iyer and collegues[22] have suggested respiring mitochondria released from pressure-disrupted or complement induced-lysis of cells actively produce ATP that is responsible for inflammasome activation. They have also shown that heating to 65^{o}C inactivated the mitochondria and reduced the ATP level released from cells as well as the inflammasome activation. Tong and colleagues have observed that Au nanorod-

enabled laser irradiation damages mitochondria[35]. The temperatures at which necrotic cell death was induced by NEPTT were often greater than 60°C[12, 101] . As a result, NEPTT may have destroyed the respiring mitochondria and reduced the level of ATP generated. It is also possible that the mitochondria were not released upon cell death as hypothesized by Iyer and collegues.[22]

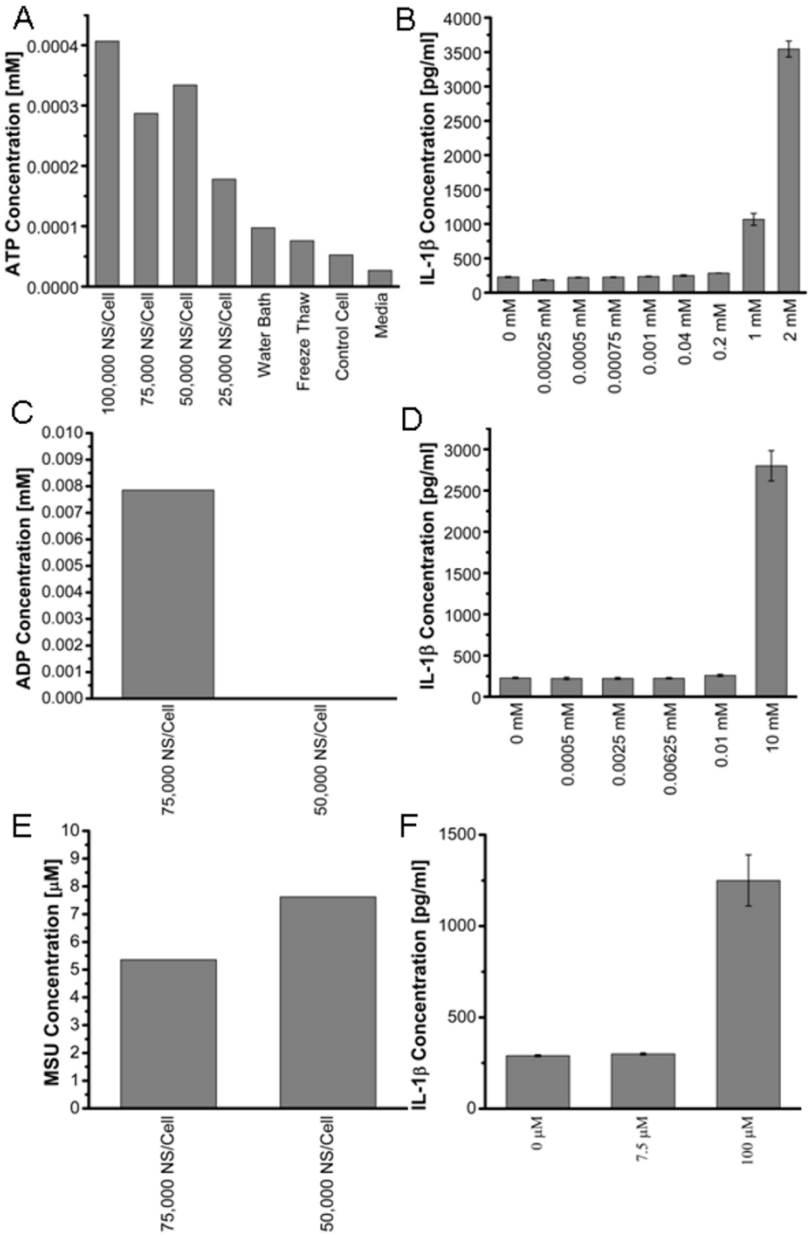

Figure 22. Cellular components released from dying cells known to trigger inflammasome activation are quantified and used to stimulate IL-1β secretion at the measured levels. (A) Extracellular ATP concentration quantified using a Promega Enliten ATP assay. (B) Inflammasome activation using 0-2 mM ATP. (C) Extracellular ADP concentration was quantified using a Bellbrook Labs ADP assay. (D) Inflammasome activation using 0-10 mM ADP. (E) Extracellular uric acid concentration was quantified. (F) Inflammasome activation using 0-100 μM MSU. IL-1β secreted by macrophages were collected after 24 h and quantified by ELISA. Values are mean ± SD. Experiments are representative of at least two independent experiments.

ATP-mediated inflammasome activation occurs through activation of the $P2X_7$ receptor found on many immune cells.[139] Exonucleases on the surface of the cell membrane or in the extracellular milieu may degrade ATP.[120] The degradation products of ATP, including ADP, AMP and adenosine, have not been shown to directly activate the inflammasome, but their ability to activate $P2X_7$ receptors and induce IL-1β secretion in immune

cells has been suggested.[121, 122, 140] ADP, the product of ATP de-phosphorylation by ATPases, was quantified for both its presence in the secreted components of NEPTT cells (*Figure 23C*) and its ability to induce inflammasome activation (*Figure 22D*). ADP levels generated by cells treated with NEPTT were higher than untreated cells, but below the threshold required to produce significant levels of IL-1β. We did not quantify AMP due to the lack of agents specific for AMP.

Uric acid, a product of purine metabolism, is released by dying cells into the extracellular environment and has been found to activate inflammasome complexes. The immunostimulatory effects of uric acid occur at the supersaturation condition (>70 μg/ml (~417μM)), indicating that MSU crystal formation is required.[123, 125] Uric acid released following NEPTT was present at insufficient levels to activate inflammasome complexes (*Figure 22E-F*). This was likely due to the low uric acid levels generated by NEPTT-treated cells, which was insufficient to induce the formation of MSU crystals.

In summary, higher levels of ATP, ADP, and uric acid were detected from NEPTT-treated cells compared to untreated-cells, indicating that DAMPs were released from NEPTT-treated cells following cell death and membrane disruption. However, the levels of these DAMPs were not sufficient to activate inflammasome complexes.

E.4 Discussion

The hidden self model proposes that endogenous DAMPs are located within the interior of the cell, and are only released following membrane disruption and release of the cytosolic components.[77] We have demonstrated that NEPTT-treated cells underwent necrosis and their cell membrane became permeable (*Figure 7*). However, the NEPTT-treated cells were poor in stimulating inflammasome complexes and pro-inflammatory cytokine secretions (*Figure 20 and 21*). The inability to stimulate inflammasomes was due to insufficient levels of the inflammasome-associated DAMPs generated or released from cells (*Figure 22*).

Supernatant levels of ATP were 3-4, ADP was 2-3, and uric acid was 1-2 orders of magnitude lower than required to activate the inflammasomes. Uric acid concentrations were not sufficient to precipitate into monosodium urate crystals, but even the presence of MSU crystals at the concentration of uric acid found in the supernatant was not sufficient to activate the inflammasome complexes.

We recognize that *in vitro* measurements can be different from what could occur *in vivo* or clinical settings. We estimated the possible level of major DAMPs released from a tumor mass 5 mm in radius and containing $5x10^6$ cells (*Table 4*).

DAMP	Measured Concentration	Cell Generation	Tumor	Blood Circulation (Human)	Blood Circulation (Mouse)
ATP	**mM**	**mmol/cell**	**mM**	**mM**	**mM**
100,000 NS/Cell	4.1E-04	2.0E-13	1.9E+00	2.5E-07	5.1E-04
75,000 NS/Cell	2.9E-04	1.4E-13	1.4E+00	1.8E-07	3.6E-04
50,000 NS/Cell	3.3E-04	1.7E-13	1.6E+00	2.1E-07	4.2E-04
25,000 NS/Cell	1.8E-04	8.9E-14	8.5E-01	1.1E-07	2.2E-04
Water Bath	9.8E-05	4.9E-14	4.7E-01	6.1E-08	1.2E-04
Freeze Thaw	7.6E-05	3.8E-14	3.6E-01	4.7E-08	9.5E-05
Control Cell	5.3E-05	2.6E-14	2.5E-01	3.3E-08	6.6E-05
Media	2.7E-05	1.3E-14	1.3E-01	1.7E-08	3.3E-05
ADP					
75,000 NS/Cell	7.9E-03	3.9E-12	3.8E+01	4.9E-06	9.8E-03
50,000 NS/Cell	0.0E+00	0.0E+00	0.0E+00	0.0E+00	0.0E+00
Uric Acid					
75,000 NS/Cell	5.4E-03	2.7E-12	2.6E+01	3.4E-06	3.3E-05
50,000 NS/Cell	7.6E-03	3.8E-12	3.6E+01	4.8E-06	3.3E-05

Table 4. Estimated *in vivo* DAMP concentrations. The measured concentration of the DAMPs ATP, ADP, and uric acid are converted to the generation rate per tumor cell. The intratumor concentration was estimated assuming a tumor density of $5*10^6$ cells within a 5 mm diameter tumor. Circulation within the bloodstream assuming dispersion was estimated for humans (4 liters total) and mice (2 ml total).

We also assumed that all the cells were loaded with sufficient levels of Au nanoshells and underwent necrotic death after NEPTT treatment. Two extreme scenarios were considered: one was that DAMPs were confined within tumor volume, and another was that DAMPs were immediately diluted into blood. NEPTT-treated cells could trigger inflammasome complexes in the first scenario but not for the second scenario. The first scenario, however, unlikely occurs since many of DAMPs are small molecules and tend to diffuse away from local tumor sites. Some DAMPs

are prone to be degraded and lose their activity (such as ATP). We also would like to note that it is nearly impossible to load all the tumor cells, especially cells located in the interior of the tumor, with a sufficient level of Au nanoshells to induce necrotic cell death and release DAMPs.

NEPTT-treated cells may be immunogenic through non-inflammasome pathways. A number of other DAMPs associated with necrotic cell death have been identified, including heat shock proteins(HSPs),[106, 116, 133] high mobility group box 1(HMGB1) protein,[110, 141, 142] S100 proteins,[143, 144] DNA,[145] RNA,[146] and the cytokine IL-6.[147]

Heat shock proteins (HSPs), including HSP70, HSP90, and GP96, are expressed in cells in response to thermal stress.[79, 103, 148, 149] These HSPs are immunogenic and can be recognized by CD14, CD40, CD91, TLR2, or TLR4.[150], [115, 116, 151, 152] They activate a variety of signaling pathways that induce pro-inflammatory cytokines (i.e. TNF-α, IL-1β, IL-6, IL-2) and play a role in DC maturation and antigen presentation[153]. The up-regulation of HSPs is generally associated with mild to moderate heating at sub-lethal doses. The release of HSPs and subsequent immune response are generally associated with necrotic cell death.[51, 106, 151, 154] Thermal ablation of cells that results in drastic temperature increase and coagulative necrosis may not allow for sufficient levels of HSP expression prior to cell death. Radiofrequency ablation used to generate temperatures in the range of 65 to 123^{o}C within a tumor showed little to no HSP70 within the tumor core but high HSP70 generation in the tumor periphery where the temperature was significantly lower.[155] Thermal ablation with multi-walled carbon nanotube enabled NIR photothermal therapy showed similar results for HSP27, HSP70, and HSP90: high temperatures within the tumor corresponds to areas with little to no HSPs, and low temperatures in the periphery of tumor corresponds high levels of HSPs. The temperatures during NEPTT generated are greater than 60^{o}C where coagulative necrosis would occur.[12],[156] Therefore, it is unlikely that significant levels of HSPs could be generated prior to cell death.

HMGB1, a nuclear protein that is secreted from necrotic cells, acts upon a number of receptors including TLR2, TLR4, and the receptor for advance glycation end products (RAGE). The activation of these receptors involves the MyD88/NF-κB signaling pathways and upregulates pro-IL-1β.[153] HMGB1 has been shown to translocate from the nucleus and subsequently released into the lysate following heating at 43.7°C, 47°C and 56°C.[107] The level of HMGB1 increases as the temperature increases up to 56°C. Under NEPTT conditions, HMGB1 could be induced. We did not directly measure HMGB1 and the production of pro-IL-1β. We tested the production of IL-1β in absence of LPS priming. The level of IL-1β was negligible. NEPTT might induce little or no HMGB1. Even if significant levels of HMGB1 were produced, other DAMPs would be required to activate the inflammasome complex to cleave pro-IL-1β into its active secreted form.

Other immunostimulatory cellular constituents such as DNA, RNA, S100 proteins, and IL-6 have also been associated with necrotic cell death.[77, 153] Low levels of DNA and RNA were released from NEPTT-treated cells (data not shown). Proteins and enzymes are likely to be inactivated during NEPTT or unable to be expressed before the cell death due to the rapid and drastic temperature increase.[31]

HSPs, DNA and RNA from necrotic cells are able to induce the maturation of DCs[145, 146, 157] and up-regulate surface molecules, such as CD86 and MHC II. We did examine whether B16 cells treated with NEPTT were able to activate immature DCs at different nanoshell dosages and the ratio of B16 to DCs (*Figure 23*). The up-regulation of both CD86 and MHCII on immature DCs were negligible compared to untreated cells. These results further confirm that NEPTT-treated cells did not release a significant level of HSPs, DNA and RNA.

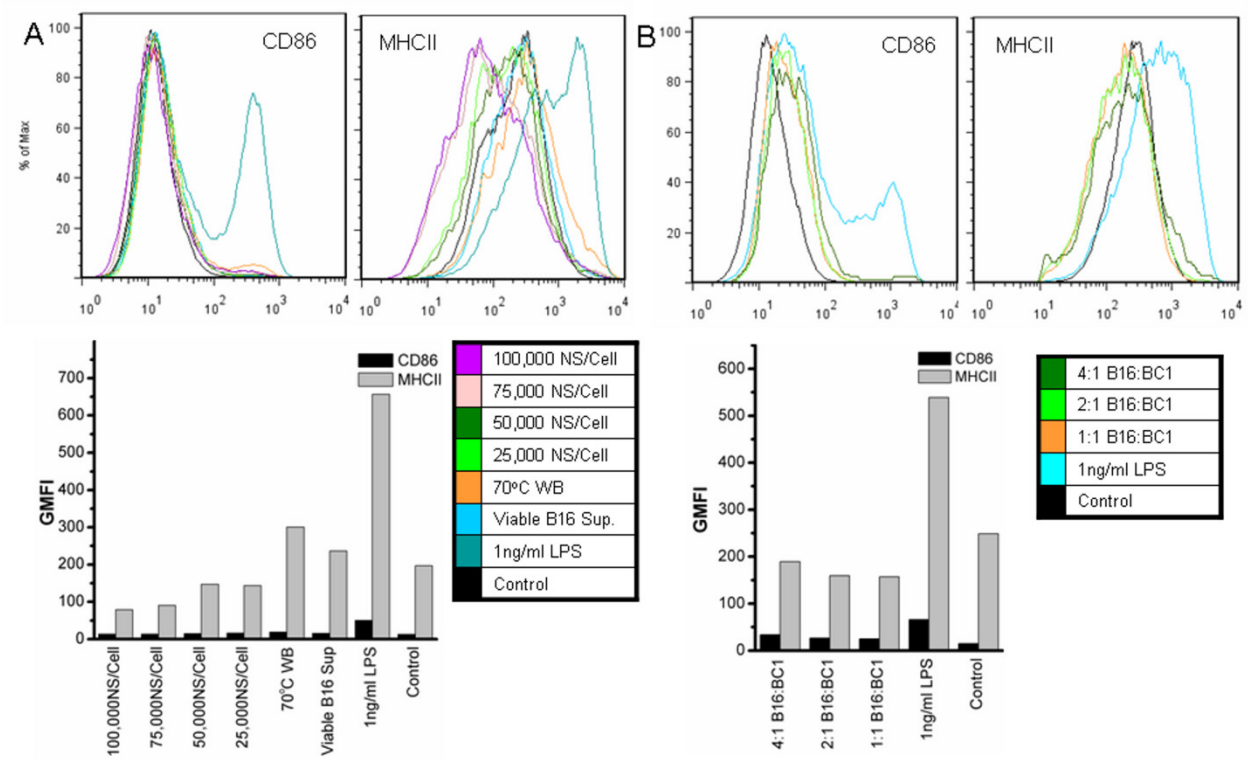

Figure 23. Killed B16 melanoma cells do not induce maturation in BC-1 dendritic cells. BC-1 maturation measured through CD86 and MHCII surface expression analyzed by flow cytometry. (A) BC-1 dendritic cells were stimulated with treated B16 cells at a ratio of B16 to BC-1 1:1 for gold nanoshell dosing concentrations of 100,000-25,000 nanoshells/cell. (B) BC-1 dendritic cells were stimulated with treated B16 cells at ratios of B16 to BC-1 from 4:1 to 1:1 for a gold nanoshell dosing concentration of 50,000 nanoshells/cell.

Taken together, cell death induced by NEPTT may not be immunogenic due. The effect of a non-immunogenic form of cell death on the efficacy of the therapy can have a range of consequences. The lack of an innate immune response may simply decrease the ability of DCs to become activated, mature, and process and present antigens, failing to establish effective adaptive immune responses against the tumor cells. Therefore, complete eradication of tumors will only rely on the primary photothermal therapy. A potential negative consequence may be the induction of immune tolerance to the tumor cells. Liu and colleagues found that mice developed a tolerogenic response to cell-associated antigen delivered in dying cells that possibly did not produce significant levels of DAMPs.[158] A tolerogenic response can result in a poor prognosis due to recurrence of tumors.

We recognize that the generation of DAMPs from necrotic cells is modality- and temperature dependent. In this study, we used nanoshells as the model system and studied the activation of inflammasomes in a cell culture system. Other nanoplasmonics may require additional analysis. The heterogeneity of the temperature profile within the tumor *in vivo* during NEPTT can generate necrotic tumor cells that may release sufficient levels of immunostimulatory DAMPs. Hirsch and colleagues reported a change in temperature range within a tumor from 10 to a maximum of 34^{o}C and an average temperature change between tumors from 28-60^{o}C.[10] An array of temperatures within a particular tumor undergoing NEPTT may provide a population of killed cells with diverse immunogenicity and/or tolerance, which can complicate the therapeutic outcomes of NEPTT.

E.5 Conclusion

Laser irradiation mediated by nanoplasmonics, including gold nanoshells, represents a novel means of surgical removal of tumors through thermal treatment. Thermal injury by NEPTT did not result in significant levels of DAMPs to activate the inflammasome complexes and induce proinflammatory cytokines, such as Il-1β. The lack of activation of inflammasomes and maybe other receptors for DAMPs potentially suppress the generation of adaptive immune responses to the tumor following NEPTT. The results from this study and other studies give insights into the development of nanoplasmonics for combined photothermal therapy and immunotherapy of cancers.

F. Chapter 6: Inflammatory Response to Nanoshell Accumulation

F.1 Background

Gold nanoshell/silica core nanoplasmonics have a broad spectrum of applications due to their unique tunable plasmon resonance. One of primary applications is laser-induced photothermal therapy, particularly for targeting cancer cells due to their passive accumulation at vascularized tumors [9-12]. Nanoshell accumulation in tumors relies on the enhance permeability and retention (EPR) effect in which circulating nanoparticles extravasate into tumors due to the leaky nature of the vasculature within the rapidly expanding tumor mass.

Normal blood vessels have tight endothelium which allows only small molecules such as nutrients to be diffuse across along with blood plasma, while retaining red blood cells and majority of macromolecules and nanoparticles[159]. Tumors larger than 2-3mm induce angiogenesis to sufficiently supply the rapidly growing tumor mass. Neovascularization of the tumor results in characteristic defective blood vessels with leaky endothelium[160]. Tumor cells also produce various growth factors such as vascular endothelial growth factor(VEGF) that increase vascular permeability[161].The leaky nature of the endothelium allows macromolecules and nanoparticles to be extravasted into the tumor interstitium where the tumor cells reside, which are not in direct contact with the blood flow. In addition to the leaky nature of the tumor blood vessels, poor lymphatic drainage allows macromolecules and nanoparticles to remain for extended periods of time[162]. This combination of increased leakiness and decreased drainage results in tumor interstitial fluid pressure (IFP), which can limit extravasation into the tumor[163, 164]. Nevertheless, gold nanoshells can still accumulate at high levels within the tumor utilizing the EPR effect[165].

Circulating nanoparticles often accumulate in other healthy organs as well, such as the liver, kidneys, spleen, and lungs[166]. In those organs, there exist abundant numbers of macrophages and other phagocytes that may tend to engulf nanoparticles encountered.

Gold nanoshell/silica core nanoplasmonics for cancer treatment and imaging has thought been relatively safe and biocompatible[3, 37, 167]. In recent years, particulates, such as micro- and nano- sized silica particles[168-170], asbestos[168], aluminum hydroxide[169], and crystal uric acid[124], have been shown to activate an intracellular sensor, NALP-3 inflammasome. NALP-3 Inflammasome is a protein complex consisting of apoptosis-associated speck protein with a caspase and recruitment domain (ASC) and caspase-1. NALP-3 acts as a scaffold protein, and ASC bridges NALP-3 to caspase-1 for its activation. The activated caspase-1 then cleaves precursors of proinflammatory cytokines, such as pro-IL-1β, to IL-1β[127]. The release of IL-1β into extracellular space triggers neutrophilic inflammatory responses. Several diseases, including silicosis, gout, asbestosis, type II diabetes mellitus, are involved in the pathway of NALP3-IL-1β. IL-1β has been responsible for many other disorders, which are extensively reviewed in [117].
It has been established that the activation of NALP-3 inflammasomes by silica particles is due to the resultant reactive oxygen species (ROS). Au nanoparticles have been shown to be the scavenger of ROS[170]. Will Au nanoshell/silica core nanoparticles activate NALP3 inflammasome and are indeed biocompatible and safe? In order to enhance their circulation time, poly(ethylene glycol) (PEG) has been used for modifying the surface of nanoparticles[29]. Will PEG attenuate or enhance the ability of Au nanoshell/silica core nanoparticles in activating NALP3 inflammasomes?
In this study, we set out to address these two questions. We show that Au nanoshell/silca core nanoplasmonics, currently involved in clinical trials, activated the NALP3 inflammasome complex and induced IL-1β secretions by macrophages. Pegylation reduced the production of IL-1β by

macrophages. Our results suggest that Au nanoshell/silica core nanoplasmonics mediated-inflammation can occur in various organs that are not being targeted for nanoshell enabled photothermal therapy. When they are used for *in vivo* imaging, neutrophilic inflammation due to the activation of NALP3 inflammasome and the generation of IL-1β should be carefully assessed. Surface modification of Au nanoshell/silica core nanoplasmonics, such as peglyation, can potentially reduce the probability of triggering NALP3 inflammasome pathway.

F.2 Research Design and Methods

Materials

Tetraethyl orthosilicate, ammonia, (3-Aminopropyl) trimethoxysilane, gold (III) chloride hydrate, sodium bicarbonate, tetrakis(hydroxymethyl)phosphonium chloride solution, sodium chloride, dihydrorhodamine 123, dichlorodihydrofluorescein, and sodium carbonate were obtained from Sigma-Aldrich (St. Louis, MO) and used as received. Carbon monoxide gas was obtained from Praxair (Danbury, CT). Cell culture supplies were obtained from Invitrogen (Carlsbad, CA). Min-U-Sil-15 was kindly provided by U.S. Silica (Berkeley Springs, WV). Enzyme-linked immunosorbent assay (ELISA) reagents including primary and secondary antibodies, Streptavidin-horse radish peroxidase (SA-HRP), and 3,3',5,5'-tetramethylbenzidine (TMB) were obtained from eBiosciences (San Diego, CA)

Cell Culture

THP-1 cells (ATCC) were maintained in Roswell Park Memorial Institute (RPMI) 1640 media supplemented with 10% fetal bovine serum (FBS), 2 mM L-glutamine, 1mM sodium pyruvate, 10 mM (4-(2-hydroxyethyl)-1-piperazineethanesulfonic acid)(HEPES), 50 μM 2-mercaptoethanol, and 1.5 g/L glucose. Cells were maintained at 37 ^{o}C and 5% CO_2, and kept at a concentration of between 4 and 8 $\times 10^5$ cells/ml.

Fabrication of nanoparticles

Silica NP and GNS nanoparticles were fabricated as previously described [171]. The PEG-GNS nanoparticles were fabricated by mixing 1 to 10 μM PEG-SH (MW: 5, 000 Da, Sigma) with GNS nanoparticles at the concentration of ~1×10^9 nanoparticles/ml. The samples were left at room temperature for 1 h while shaking. Excess PEG-SH of was removed by 3 times of centrifugation and followed by wash steps, The PEG-GNS nanoparticles were dispersed and stored in Milli-Q water before use.

Characterization of nanoparticles

Nanoparticles were characterized by scanning electron microscopy (SEM) (JOEL 7200 SEM) and UV-Vis spectroscopy (Molecular Devices Spectramax M5). The particle size was calculated based on SEM images. The shell thickness was estimated based on the images of silica NP and GNS nanoparticles. The size distribution and aggregation of nanoparticles were examined by the dynamic light scattering using a Malvern Zetasizer Nano ZS (Malvern Instruments Ltd Worcestershire, UK).

The silica particle concentration was calculated based on the average volume of each individual silica particle and silica mass concentration determined by freeze drying an aliquot of known volume of the stock solutions. The molecular weight and density of the silica particles was assumed to be similar to bulk values. GNS nanoparticle concentration was estimated based on the quantity of silica particles assuming no loss of silica particles during the preparation of GNS nanoparticles.

Stimulation of macrophages

THP-1 cells were initially treated in 96-well plates with 2 μg/ml lipopolysaccharide (LPS) from Escherichia coli 0111:B4 (Sigma) for 24 h at $1x10^5$ cells/cell. Then they were stimulated with different nanoparticles and Min-U-Sil 15 silica crystals (silica MP) in culture medium without FBS for 4 h before the addition of the FBS to a final concentration of 10%. Supernatants were sampled

after 24 h for ELISA. THP-1 cells incubated with cell culture media only after LPS stimulation were used as negative controls to determine the background level of IL-1β.

Enzyme-linked Immunosorbent Assay (ELISA)

The level of IL-1β secreted by macrophages was assessed by ELISA. Anti-human IL-1β (clone CRM56) was used as the capture antibody and biotinylated mouse anti-human IL-1β antibody (clone CRM57) was used as the detection antibody. Samples were diluted at a proper range with the blocking buffer (1% FBS in PBS). The detection range for IL-1β was 8 - 2000 pg/ml. Standard procedures described in eBioscience protocol literature (eBioscience) were used.

Detection of intracellular ROS

Intracellular ROS generation was assessed using the fluorescent probes dichlorodihydrofluorescein(DCF) and dihydrorhodamine 123 (DHR 123) (Sigma Aldrich St. Louis, MO). DHR 123 and DCF are cell permeable dyes that become fluorescent following the oxidation by ROS. $1x10^5$ LPS-treated THP-1 cells in 96-well plate were incubated with 10 μM DHR 123 and DCF for 45 min, washed twice carefully with DPBS, and exposed to the nanoparticles dispersed in media without FBS. ROS levels were monitored for a duration of 2 h at 490 nm (Ex)/536 nm (Em) in by a SpectrMax M5 plate reader.

Assessment of scavenging effect of GNS, PEG-GNS nanoparticles

50μl hydrogen peroxide (H_2O_2) was introduced to a 50μl solution containing GNS and PEG-GNS for 30 min at a concentration range from 10 to 0.1 μM of H_2O_2 in 96 well plates. The solutions were then spun down at 2000 rpm for 10 min to remove all the nanoparticles. 50μl of the supernatant was transferred to an opaque white Costar 96-well plate, and 50 μl of solution containing HRP at a 1:100 ratio, and 10μM DCF were added to each well. The solutions were allowed to react for 15 min before the fluorescence was measured at 490 nm (Ex)/536 nm (Em) in 96-well plate on a SpectraMax M5 plate reader.

Assessment of the quenching of fluorescence of DHR 123 and DCF by Au nanoparticles

A solution containing 100 μM of H_2O_2, HRP at a 1:100 ratio, and 4 μM of DHR 123 or DCF was reacted for 15 min before the addition of nanoparticles at a final concentration of 5 to 1mg/ml and measured immediately at 490 nm (Ex)/536 nm (Em) in 96-well plate on a SpectrMax M5 plate reader.

Statistical analysis

All results are representative of at least two sets of independent experiments, with samples performed in duplicates or triplicates. Results represent average values ± the standard deviation (SD) of the samples unless otherwise indicated.

F.3 Results

Characterization of nanoparticles

Four types of nanoparticles, including Au nanoshell/silica core (GNS), PEGlyated Au nanoshell/silica core (PEG-GNS), and silica nanoparticles (Si NP), were used in this study. GNS consisted of a silica core of 119 ± 11nm in diameter (Figure 24A) and a 17 nm-thick of gold shell (Figure 1b). PEG-GNS showed an increase in hydrodynamic diameter by 25 nm (Figure 24B) and zeta potential by 20 mV (Figure 24C), consistent with literature findings for other gold nanosparticles that show an increase in hydrodynamic diameter and neutralization of surface charge[172]. Both GNS and PEG-GNS nanoparticles used in this study exhibited similar dimensions and optical properties as used in previous *in vivo* and *in vitro* studies [5, 7, 9, 10, 25, 32, 92, 173] (Figure 24D). The silica particles exhibited positive charge with the zeta potential of 40 mV (Figure 24C).

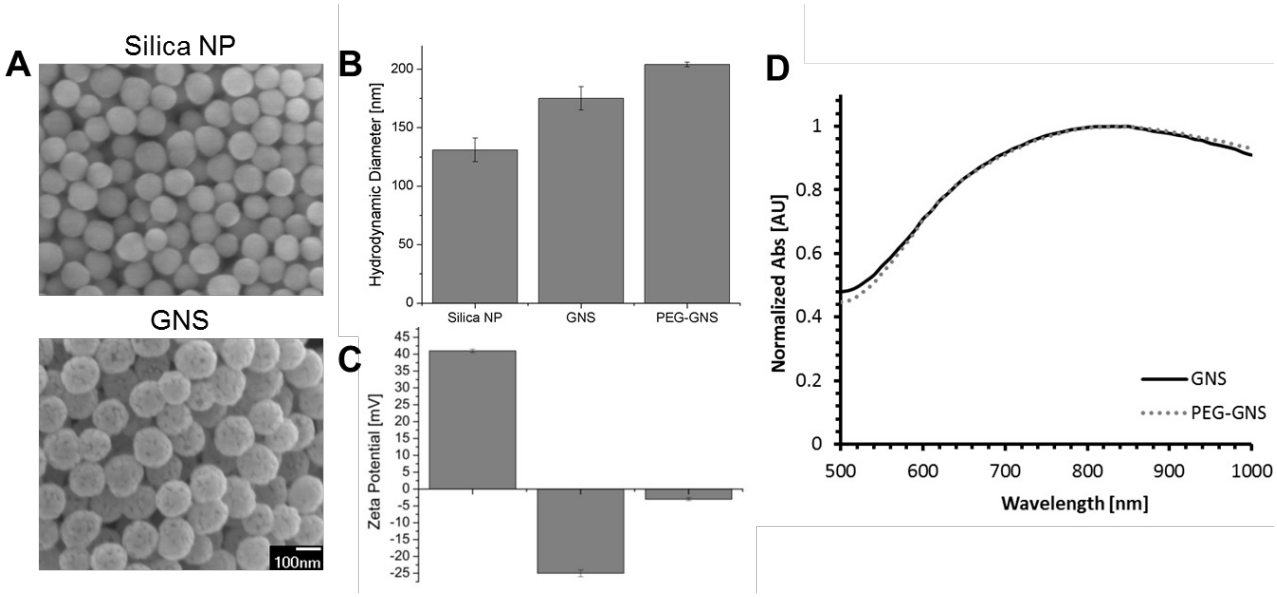

Figure 24. Characterization of silica and gold shell nanoparticles. (A) Scanning electron microscopy (SEM) image of silica nanoparticles (silica NP), and Au nanoshell/silica core nanoparticles (GNS). (B) Hydrodynamic size and (C) Zeta Potential of silica NP, GNS and pegylated GNS (PEG-GNS) measured by dynamic light scattering. (D) UV-Vis absorption spectra of GNS and PEG-GNS in water. The GNS had a SPR peak at 830 nm.

Cellular uptake of nanoparticles and morphological changes of macrophages

Initially, we qualitatively assessed the cellular uptake of the nanoparticles by microscopic analysis (Figure 25). The cellular uptake of all the nanoparticles increased as their concentrations that cells were exposed to increased. Silica nanoparticles were taken up by THP-1 cells at a higher level than other nanoparticles due to their positively charged surfaces. For all types of particles, some nanoparticles were simply associated with the surface of cells and could not be removed by washes. GNS appeared to aggregate while PEG-GNS remained dispersed at the high concentration of nanoparticles. Cells formed large aggregates in the presence of high concentration of GNS (> 3 mg/ml) and silica particles, but not in the presence of PEG-GNS (Figure 25).

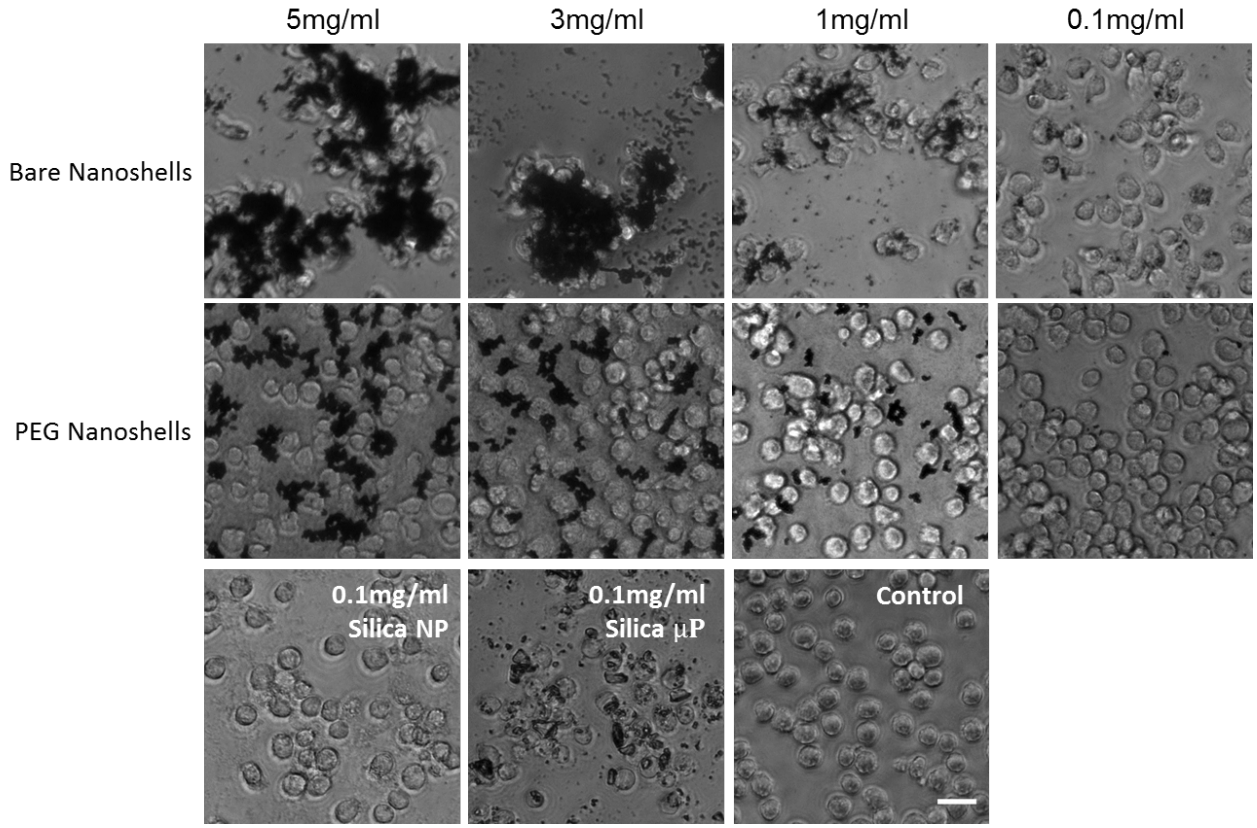

Figure 25. Cellular uptake of nanoparticles at different concentrations of particles. Light microscopy images of cells incubated with GNS, PEG-GNS ranging from 5.0 to 0.1mg/ml. Silica NP and Min-U-Sil 15 silica microparticles (Silica μP) at 0.1mg/ml and cells with no nanoparticles(Control). Scale bar 20μm

Induction of secretion of IL-1β by nanoparticles

Recent studies suggest that particulates such as silica particles and asbestos can activate NALP3 inflammasome and induce the cleavage of pro-IL-1 and subsequent IL-1β secretions[124, 168, 169, 174]. We examined whether GNS and PEG-GNS, or silica NP would trigger NALP3 inflammasomes. Silica microparticles, used in previous studies[169], were used as controls (Figure 25). A human macrophage-like cell line, THP-1, was used. THP-1 cells have been well characterized as a cell line that responds to a variety of well-documented inflammasome-inducers[136-138]. THP-1 cells were first treated with lipopolysaccharide (LPS) to induce pro-IL-1β. Upon the stimulation of inflammasomes, pro-IL-1β is cleaved into IL-1β, which is secreted from cells. The stimulation of inflammasomes can therefore be assessed by the secretion of IL-1βin THP-1 cells.

As shown in Figure 26, PEG-GNS did not induce the secretion of IL-1β at the concentration up to 5 mg/ml. In contrast, GNS yielded a statistically significant level of IL-1β at 3 mg/ml nanoparticles compared to cells without particles, and the level of IL-1β increased as concentrations of particles increased. Silica NP at the same mass concentration as GNS particles induced nearly 5 to 8 fold higher level of IL-1β. In summary, the ability of the same mass concentration of nanoparticles in stimulating the inflammasomes followed the order: SNP > GNS > PEG-GNS nanoparticles.

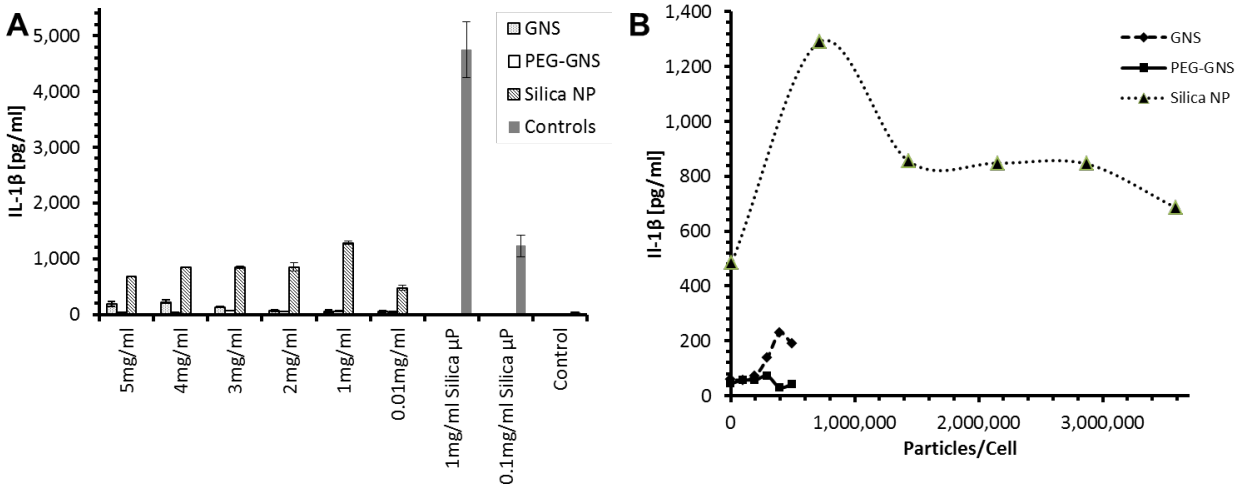

Figure 26. The stimulation of IL-1β production by GNS, PEG-GNS, and silica NP. (A) LPS-treated THP-1 macrophage cells were stimulated with nanoparticles at concentrations ranging from 5 mg/ml to 0.01mg/ml. Silica µP were used as a positive control, and untreated cells were used as a negative control (Control). IL-1β secreted by stimulated macrophages were collected after 24 h and quantified by ELISA. Values are mean ± S.D. (B) IL-1β levels plotted as a function of particles/cell exposed to the macrophages. Experiments are representative of three independent experiments.

Generation of Reactive Oxygen Species (ROS) by nanoparticles

It has recently been clearly demonstrated that ROS induced by silica particles and uric acid releases thioredoxin (TRX)-interacting protein (TXNIP) from TRX, and released TXNIP binds and activates NALP3 inflammasome [168]. We subsequently assessed intracellular ROS levels induced by different nanoparticles by a ROS fluorescent probe, DCF. Cells exposed to a given concentrations of soluble H_2O_2 were used as controls. We monitored the fluorescence change for 2 h (Figure 30). The fluorescence of oxidized DCF leveled off after 1 h for all the particle groups and

soluble H_2O_2 except high concentrations of silica nano- and micro-particles. For clarification, we compared all the groups at 100 min (Figure 27).

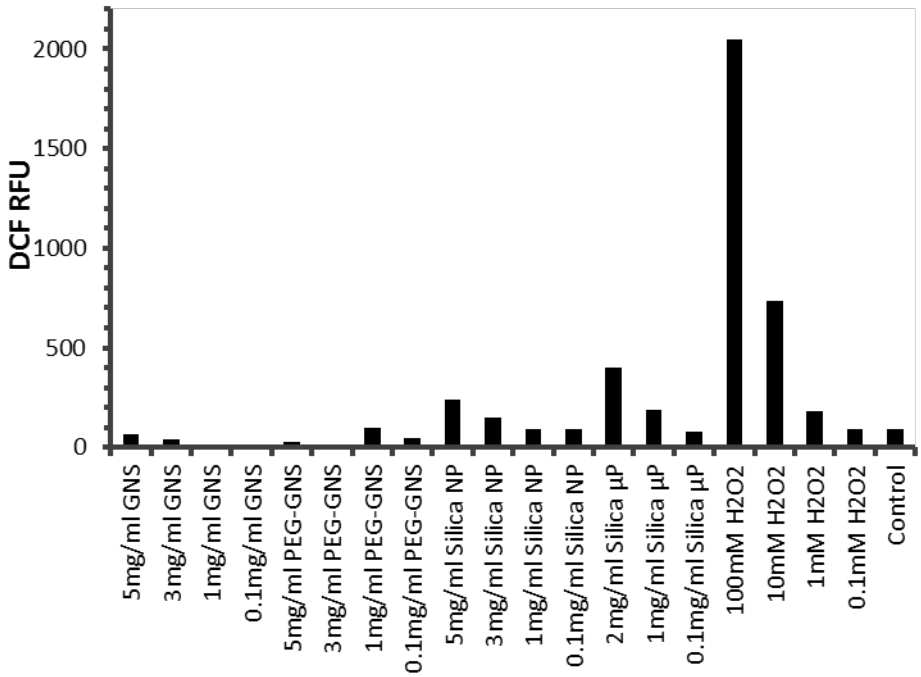

Figure 27. ROS generation by GNS, PEG-GNS, and silica NP. LPS-treated THP-1 macrophage cells were stimulated with nanoparticles at concentrations ranging from 5 mg/ml to 0.1mg/ml. Silica µP and extracellular H_2O_2 were used as a positive control, and untreated cells were used as a negative control (Control). ROS generation was monitored for a duration of 120 min with the ROS specific fluorescent probe DCF. For clarity, the fluorescent intensity at 100min was plotted. The kinetics of fluorescent intensity of DCF is shown in Figure 30.

As expected, intracellular level of H_2O_2 linearly increased as extracellular concentration of H_2O_2 increased. For particle groups, silica NP exhibited significant level of intracellular ROS, which increased as the mass concentration of particles increased. Interestingly, both GNS and PEG-GNS did not yield a significant level of intracellular ROS in comparison with cells without any treatments. Macro-sized silica particles generated a significant level of ROS as demonstrated in previous studies[170].

Scavenger effect and fluorescent quenching of Au nanoparticles

Silica particles induced a significant level of ROS detected by DCF while a low level, even lower than untreated cells, of ROS was detected in cells treated with either GNS or PEG-GNS

nanoparticles. The level of ROS induced by silica particles correlated with that of IL-1β. The signal of DCF of cells treated by GNS and PEG-GNS nanoparticles was lower than untreated cells. As shown in Figure 3, GNS at the concentration greater than 3 mg/ml instigated a lower but significant level of IL-1β.

Two questions were raised: Do GNS or PEG-GNS nanoparticles not generate ROS at all, or is the generated ROS scavenged by them? Do Au nanoparticles quench the fluorescence of the ROS probe, DCF? We first tested whether Au nanoparticles acted as the scavenger of ROS. A known concentration of H_2O_2 was reacted with all Au nanoparticles for 30 min followed by the removal of Au nanoparticles. The residual of H_2O_2 was detected by DCF. As shown in *Figure 28*, only GNS particles exhibited a statistically significant scavenger effect while PEG-GNS did not.

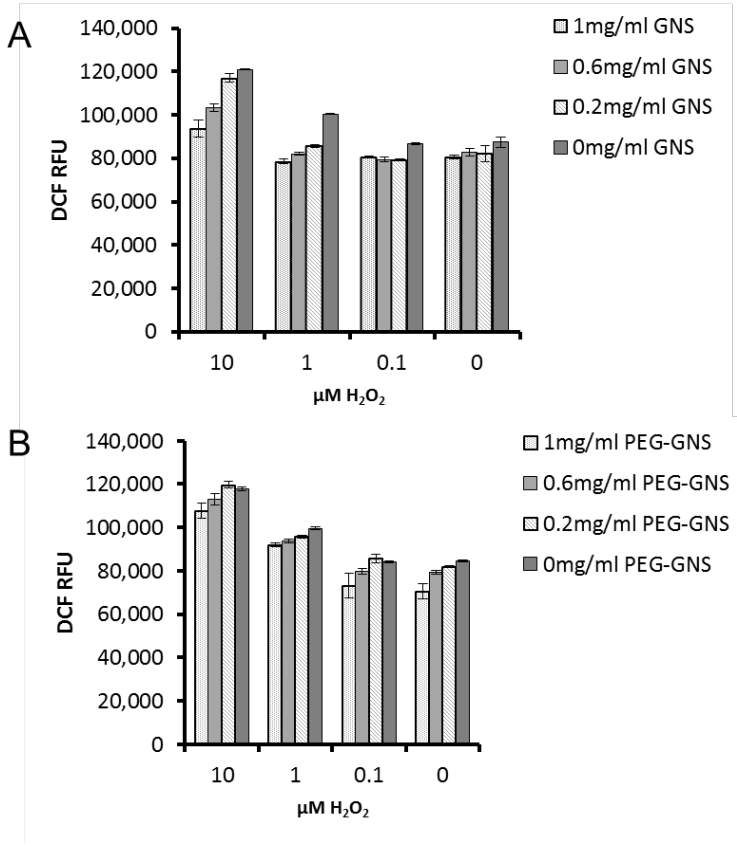

Figure 28. H_2O_2 scavenging effects of GNS (A), PEG-GNS (B) nanoparticles. Nanoparticles are incubated with H_2O_2 solutions of varying concentrations for 15 mins prior to centrifugation and removal of the supernatant to assay for levels using the fluorescent ROS dye DCF. Values are mean ± S.D. Experiments are representative of two independent experiments.

The broad absorption spectrum of Au nanoparticles (Figure 25D) suggested that Au nanoparticles could potentially quench fluorescence of DCF, which was excited at 490 nm and emitted at 536 nm. We tested this possibility by first oxidizing DCF with a given concentration of H_2O_2 and then tested the fluorescence level of DCF in the presence or absence of Au nanoparticles. As shown in Figure 29, both GNS and PEG-GNS quenched the fluorescence of DCF at a concentration dependent manner. In the presence of 1 mg/ml of particles, the fluorescence of DCF was reduced 6 times.

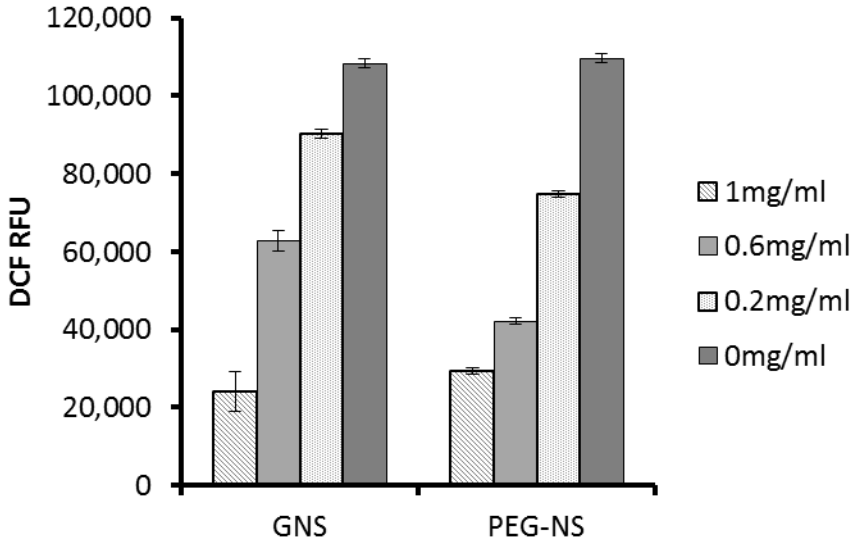

Figure 29. Fluorescent quenching effects of GNS and PEG-GNS. H_2O_2 is reacted with DCF prior to nanoparticle addition and fluorescence at 536nm is measured. Values are mean ± S.D. Experiments are representative of two independent experiments.

F.4 Discussion

GNS or surface modified GNS (i.e. PEG-GNS) are currently utilized in clinical trials for cancer treatment[175]. The components of these particles, silica and gold, are considered to be both biocompatible and nontoxic, and are used in various applications in medicine[167]. In this study, we have assessed the ability of GNS, PEG-GNS and silica nanoparticles to activate the NALP3 inflammasome and induce the production of proinflammatory cytokines IL-1β (Figure 26A). Our results demonstrate that non-pegylated GNS induced significantly higher levels of IL-1β compared

to pegylated ones (Figure 26A); silica nanoparticles yielded about 5 times higher level of IL-1β than non-pegylated GNS at the same mass concentration (Figure 26B).

In recent years, it is established that the ROS induced by particulates, such as silica nano- and micro-particles and crystal uric acid, activates NALP3 inflammasome, which cleaves pro-IL-1β into secretory form of IL-1β. Intracellular ROS was detected by DCF as in this study. For silica particles, the generation of IL-1β was correlated with the level of ROS, which is consistent with previous findings[170]. The correlation of DCF signal, ROS level and IL-1β generation induced by Au nanoparticles became less apparent due to the quenching and scavenging effects of these particles (Figure 28 and 29). Based on our observations (Figure 26, 27 and 29), PEG-GNS unlikely induced a significant level ROS, and the reduced signal of DCF compared to untreated cells was attributed to the quenching effect by particles. The DCF signal in cells treated with them correlated the level of ROS and resultant IL-1β GNS did induce ROS at the high concentration (> 3 mg/ml), but both the scavenging and quenching effects masked the generation of ROS that was undetected by DCF. Additionally, the scavenging effect possibly diminished the activation of NALP3 inflammasome by ROS and thus the level of IL-1β. As a result, GNS was less active in stimulating NALP3 inflammasomes than silica NP.

ROS generation by macrophages in response to particulates is due to the phagocytosis of the particles and the activation of NADPH oxidase[168]. Frustrated phagocytosis, which occurs when the particles are not able to be internalized by cells is also thought to activate the NADPH pathways to generate ROS[176]. While the NADPH pathway has been implicated in the generation of ROS during the frustrated phagocytosis, some evidence suggests that this pathway is not the sole pathway. Mice lacking the gp91phox subunit (NOX2) of the NADPH oxidase complex still respond to silica and MSU crystals as wild type [169]. Zhou and colleagues have recently

demonstrated that mitochondria, in response to the particulates such as silica and MSU crystals, can generate ROS that activates NALP3 inflammasome [177].

The catalytic decomposition of reactive oxygen species such as hydrogen peroxide(H_2O_2) by gold surfaces has been studied by various groups. Much of the earlier work on H_2O_2 decomposition was summarized by Johannes Schwank[178]. Based on the mechanisms proposed by Weiss[179] and Ono[180] and adapted for Au, decomposition of H_2O_2 proceeds through a number of reactions with an array of intermediates. The rate limiting step in the decomposition of H_2O_2 is in the initial electron transfer from the gold to hydrogen peroxide catalyzing the decomposition to a hydroxyl anion and hydroxyl radical(Equation 19). From there a number of reactions can occur and are outlined below:

$$Au + H_2O_2 \rightarrow Au^+ + OH^- + \cdot OH \quad (19)$$

$$H_2O_2 + \cdot OH \rightarrow H_2O + \cdot HO_2 \quad (20)$$

$$\cdot HO_2 \leftrightarrow H^+ + O_2^- \quad (21)$$

$$Au^+ + O_2^- \rightarrow Au + O_2 \quad (22)$$

$$Au + HO_2 \rightarrow Au^+ + HO_2^- \quad (23)$$

$$Au^+ + HO_2 \rightarrow Au + \cdot HO_2 \quad (24)$$

Bulk gold, a noble metal, has been typically regarded as a relatively inactive catalyst. The limited but measureable capability of bulk gold catalytic decomposition of hydrogen peroxide compared to other metals , alloys, and metal oxides has been well established[180, 181]. However nano sized gold owing to its high surface area to volume ratio have been used extensively in various catalysis reactions summarized in the following reviews[182-184]. While nanometer sized colloidal gold grown from reduction of HAuCl4 showed low H_2O_2 decomposition catalytic capability[185], nanoparticle gold supported on a range of materials showed high catalytic activity, mainly on polymers[186] and metal oxides such as TiO_2, ZnO, $SrTiO_3$, $BiVO_4$[187, 188]. Suh and coworkers showed gold deposited on SiO_2 had higher decomposition activity for H_2O_2 than α-Al_2O_3, TiO_2 or

SiO_2[189]. This would suggest that gold nanoshells, with a silica(SiO_2) core support and a gold shell could be active in H_2O_2 decomposition. Decomposition of H_2O_2 and corresponding decomposition of superoxide O_2^- according to equations 20 and 22 above, would provide a reasonable mechanism for reactive oxygen species(ROS) scavenging produced by the cell by gold nanoshells taken up or interacting in with the cell, minimizing the ROS signaling required for NALP3 inflammasome activation.

GNS nanoparticles appeared to form aggregates and aggregation became more severe at the high mass concentrations. Macrophages formed clusters and attempted to engulf the aggregated nanoshells. In contrast, PEG-GNS nanoparticles remained dispersed and formed rather small aggregates (Figure 25). Therefore, the induction of ROS by GNS was likely through the NADPH pathway due to the frustrated phagocytosis of aggregated GNS. GNS nanoparticles are often pegylated for *in vivo* applications to increase circulation time[190, 191]. Our results suggest that PEGylation also reduces the aggregation of particles and thus attenuates the ability of GNS in activating NALP3 inflammasome.

GNS particles injected intravenously for cancer photothermal therapy accumulates in the liver, kidney, spleen, and lungs in addition to the targeted tumor sites [165]. High levels of accumulation in those organs can expose phagocytes, such as macrophages, to an environment containing a high concentration of particles. In such cases, activation of NALP3 inflammasomes likely occurs and leads to a cascade of inflammatory responses in untargeted organs. Chronic inflammation at untargeted sites can compromise the treatment of cancers and cause severe side effects. Peglyation of GNS plays a dual role in the activation of inflammasomes. Peglyation reduces the scavenging effect of GNS nanoparticles and the possibility of forming large aggregates. The balancing of these two effects can be a critical design parameter for minimizing inflammatory responses due to the activation of inflammasomes.

F.5 Conclusions

We have demonstrated here that Au nanoshell/silica core nanoparticles activate inflammasome complex in macrophages, resulting in the release of the proinflammatory cytokine IL-1β. They join a growing list of particulates that act as "danger signal" and trigger the intracellular sensors of the innate immune system. Colloidal stability of particles in a given physiological environment appears to play a critical role. Aggregations of particles can lead to frustrated phagocytosis and ROS generation, which may activate inflammasomes. Surface modification of these particles with PEG successfully minimizes the aggregation and mitigates the activation of inflammasomes. These findings have important implications in designing nanoplasmonics for either imaging or therapy. Though Au nanoshell/silica core nanoparticles were assessed in this study, our finding in correlating the aggregation with the activation of NALP3 inflammasomes has implications in other particulates for drug delivery, imaging and therapy as well.

F.6 Supplementary Information

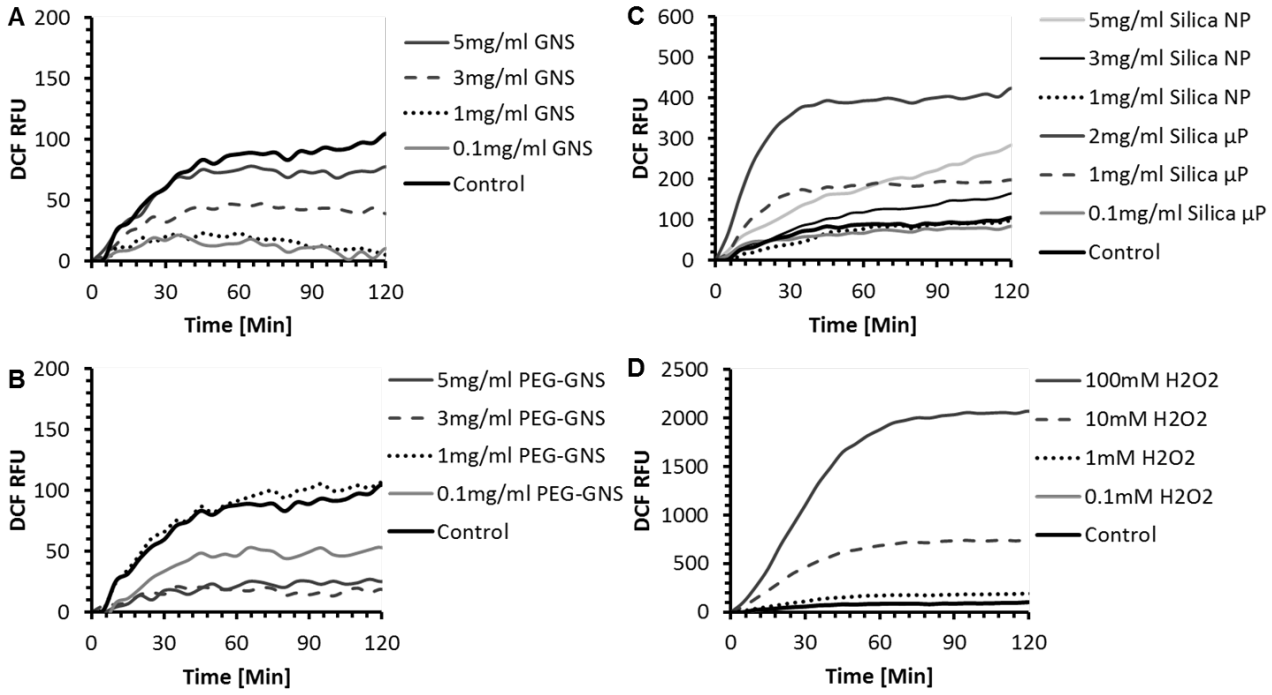

Figure 30. Kinetics of intracellular ROS generation. LPS-treated THP-1 macrophage cells were stimulated with nanoparticles at concentrations ranging from 5 mg/ml to 0.1mg/ml. Silica µP and extracellular H_2O_2 were used as a positive control, and untreated cells were used as a negative control (Control). ROS generation was monitored for a duration of 120 min with the ROS specific fluorescent probe DCF.

G. Conclusions and Future Directions

Gold nanoshells have been shown to be useful in a variety of biomedical applications, and have already reached clinical trial status. This thesis expands on both the fundamental aspects of the nanoshell enabled photothermal therapy induced damage through experimentation and modeling using quantifiable methodologies. Immunological implications of the nanoshell accumulation and cell death associated with the thermal ablation were also addressed, with a focus on the newly discovered inflammasome complex implicated in a variety of innate immune responses to sterile inflammation.

Combined Nanoshell Enabled Photothermal and Immunotherapy

In recent years, increasing research has begun to map out the innate immune response to cell damage and death within the body. Cell death modality has been shown to be an important factor in the induction of the inflammation process and the resulting innate immune responses.[22, 125, 192] While our work *in vitro* did not indicate an immune response to the thermally ablated cells, the tumor microenvironment *in vivo*, along with differing accumulation levels and treatment parameters may induce an immune response that could be utilized to increase tumor clearance and regression as well as the development of an adaptive specific antitumor immune response. This could lead to the eradication of metastases at distant sites from the primary treatment, and the ability to defend against future rechallenges.

Induced Inflammation by Gold Nanoshell Accumulation

Our preliminary exploration of the inflammatory response to gold nanoshells indicates that at high concentrations, sensing of the nanoparticulates can occur by resident macrophages in sites of accumulation which can trigger the activation of the NALP3 inflammasome complex resulting in the generation of proinflammatory cytokines. The can be mediated by surface modification and passivation *in vitro*. It has yet to be determined if an inflammatory response to high levels of

nanoshells *in vivo* occurs, and what the potential implications to successful cancer photothermal therapy.

Gold Nanoshell Catalysis

Our initial observation of H_2O_2 decomposition catalyzed by the gold nanoshells opens up the possibility for the use of gold nanoshells, and silica particles with varying degrees of gold coverage for the catalysis of a range of reactions that gold nanoparticles are currently being used for. Optimizing the H_2O_2 decomposition reaction and determining the reaction kinetics would be the initial step, followed by the examination of other gold catalyzed reactions.

I. References

[1] Oldenburg SJ, Averitt RD, Westcott SL, Halas NJ. Nanoengineering of optical resonances. Chemical Physics Letters. 1998;288:243-7.

[2] Aden AL, Kerker M. Scattering of Electromagnetic Waves from 2 Concentric Spheres. Journal of Applied Physics. 1951;22:1242-6.

[3] Lal S, Clare SE, Halas NJ. Nanoshell-Enabled Photothermal Cancer Therapy: Impending Clinical Impact. Accounts of Chemical Research. 2008;41:1842-51.

[4] Bernardi RJ, Lowery AR, Thompson PA, Blaney SM, West JL. Immunonanoshells for targeted photothermal ablation in medulloblastoma and glioma: an in vitro evaluation using human cell lines. Journal of Neuro-Oncology. 2008;86:165-72.

[5] Gobin AM, Moon JJ, West JL. EphrinA1-targeted nanoshells for photothermal ablation of prostate cancer cells. International Journal of Nanomedicine. 2008;3:351-8.

[6] Loo C, Lin A, Hirsch L, Lee MH, Barton J, Halas N, et al. Nanoshell-enabled photonics-based imaging and therapy of cancer. Technology in Cancer Research & Treatment. 2004;3:33-40.

[7] Loo C, Lowery A, Halas N, West J, Drezek R. Immunotargeted nanoshells for integrated cancer imaging and therapy. Nano Letters. 2005;5:709-11.

[8] Lowery AR, Gobin AM, Day ES, Halas NJ, West JL. Immunonanoshells for targeted photothermal ablation of tumor cells. International Journal of Nanomedicine. 2006;1:149-54.

[9] Gobin AM, Lee MH, Halas NJ, James WD, Drezek RA, West JL. Near-infrared resonant nanoshells for combined optical imaging and photothermal cancer therapy. Nano Letters. 2007;7:1929-34.

[10] Hirsch LR, Stafford RJ, Bankson JA, Sershen SR, Rivera B, Price RE, et al. Nanoshell-mediated near-infrared thermal therapy of tumors under magnetic resonance guidance. Proceedings of the National Academy of Sciences of the United States of America. 2003;100:13549-54.

[11] O'Neal DP, Hirsch LR, Halas NJ, Payne JD, West JL. Photo-thermal tumor ablation in mice using near infrared-absorbing nanoparticles. Cancer Letters. 2004;209:171-6.

[12] Stern JM, Stanfield J, Kabbani W, Hsieh JT, Cadeddu JRA. Selective prostate cancer thermal ablation with laser activated gold nanoshells. Journal of Urology. 2008;179:748-53.

[13] Loo C, Hirsch L, Lee MH, Chang E, West J, Halas N, et al. Gold nanoshell bioconjugates for molecular imaging in living cells. Optics Letters. 2005;30:1012-4.

[14] Tam F, Goodrich GP, Johnson BR, Halas NJ. Plasmonic enhancement of molecular fluorescence. Nano Letters. 2007;7:496-501.

[15] Hirsch LR, Jackson JB, Lee A, Halas NJ, West J. A whole blood immunoassay using gold nanoshells. Analytical Chemistry. 2003;75:2377-81.

[16] Lal S, Grady NK, Kundu J, Levin CS, Lassiter JB, Halas NJ. Tailoring plasmonic substrates for surface enhanced spectroscopies. Chemical Society Reviews. 2008;37:898-911.

[17] Wang H, Brandl DW, Nordlander P, Halas NJ. Plasmonic nanostructures: Artificial molecules. Accounts of Chemical Research. 2007;40:53-62.

[18] Kundu J, Le F, Nordlander P, Halas NJ. Surface enhanced infrared absorption (SEIRA) spectroscopy on nanoshell aggregate substrates. Chemical Physics Letters. 2008;452:115-9.

[19] Zaman RT, Diagaradjane P, Wang JC, Schwartz J, Rajaram N, Gill-Sharp KL, et al. In vivo detection of gold nanoshells in tumors using diffuse optical spectroscopy. Ieee Journal of Selected Topics in Quantum Electronics. 2007;13:1715-20.

[20] Diagaradjane P, Shetty A, Wang JC, Elliott AM, Schwartz J, Shentu S, et al. Modulation of in vivo tumor radiation response via gold nanoshell-mediated vascular-focused hyperthermia: Characterizing an integrated antihypoxic and localized vascular disrupting targeting strategy. Nano Letters. 2008;8:1492-500.

[21] Pham T, Jackson JB, Halas NJ, Lee TR. Preparation and characterization of gold nanoshells coated with self-assembled monolayers. Langmuir. 2002;18:4915-20.
[22] Iyer SS, Pulskens WP, Sadler JJ, Butter LM, Teske GJ, Ulland TK, et al. Necrotic cells trigger a sterile inflammatory response through the Nlrp3 inflammasome. Proceedings of the National Academy of Sciences of the United States of America. 2009;106:20388-93.
[23] Stober W, Fink A, Bohn E. Controlled Growth of Monodisperse Silica Spheres in Micron Size Range. Journal of Colloid and Interface Science. 1968;26:62-9.
[24] Duff DG, Baiker A, Edwards PP. A New Hydrosol of Gold Clusters .1. Formation and Particle-Size Variation. Langmuir. 1993;9:2301-9.
[25] Brinson BE, Lassiter JB, Levin CS, Bardhan R, Mirin N, Halas NJ. Nanoshells Made Easy: Improving Au Layer Growth on Nanoparticle Surfaces. Langmuir. 2008;24:14166-71.
[26] Park S, Park M, Han P, Lee S. Relative contributions of experimental parameters to NIR-absorption spectra of gold nanoshells. Journal of Industrial and Engineering Chemistry. 2007;13:65-70.
[27] Phonthammachai N, Kah JCY, Jun G, Sheppard CJR, Olivo MC, Mhaisalkar SG, et al. Synthesis of contiguous silica-gold core-shell structures: Critical parameters and processes. Langmuir. 2008;24:5109-12.
[28] Du H, Chandaroy P, Hui SW. Grafted poly-(ethylene glycol) on lipid surfaces inhibits protein adsorption and cell adhesion. Biochim Biophys Acta-Biomembr. 1997;1326:236-48.
[29] Howard MD, Jay M, Dziublal TD, Lu XL. PEGylation of nanocarrier drug delivery systems: State of the art. J Biomed Nanotechnol. 2008;4:133-48.
[30] Vonarbourg A, Passirani C, Saulnier P, Benoit JP. Parameters influencing the stealthiness of colloidal drug delivery systems. Biomaterials. 2006;27:4356-73.
[31] Hildebrandt B, Wust P, Ahlers O, Dieing A, Sreenivasa G, Kerner T, et al. The cellular and molecular basis of hyperthermia. Crit Rev Oncol/Hematol. 2002;43:33-56.
[32] Huang XH, Jain PK, El-Sayed IH, El-Sayed MA. Determination of the minimum temperature required for selective photothermal destruction of cancer cells with the use of immunotargeted gold nanoparticles. Photochem Photobiol. 2006;82:412-7.
[33] Dickerson EB, Dreaden EC, Huang XH, El-Sayed IH, Chu HH, Pushpanketh S, et al. Gold nanorod assisted near-infrared plasmonic photothermal therapy (PPTT) of squamous cell carcinoma in mice. Cancer Letters. 2008;269:57-66.
[34] Huff TB, Tong L, Zhao Y, Hansen MN, Cheng JX, Wei A. Hyperthermic effects of gold nanorods on tumor cells. 2007. p. 125-32.
[35] Tong L, Cheng JX. Gold nanorod-mediated photothermolysis induces apoptosis of macrophages via damage of mitochondria. Nanomedicine. 2009;4:265-76.
[36] Au L, Zheng DS, Zhou F, Li ZY, Li XD, Xia YN. A quantitative study on the photothermal effect of immuno gold nanocages targeted to breast cancer cells. Acs Nano. 2008;2:1645-52.
[37] Day ES, Morton JG, West JL. Nanoparticles for Thermal Cancer Therapy. Journal of Biomechanical Engineering-Transactions of the Asme. 2009;131:5.
[38] Huang YF, Sefah K, Bamrungsap S, Chang HT, Tan W. Selective Photothermal Therapy for Mixed Cancer Cells Using Aptamer-Conjugated Nanorods. Langmuir. 2008;24:11860-5.
[39] Jain PK, Huang XH, El-Sayed IH, El-Sayed MA. Noble Metals on the Nanoscale: Optical and Photothermal Properties and Some Applications in Imaging, Sensing, Biology, and Medicine. Accounts of Chemical Research. 2008;41:1578-86.
[40] Kah JCY, Wan RCY, Wong KY, Mhaisalkar S, Sheppard CJR, Olivo M. Combinatorial treatment of photothermal therapy using gold nanoshells with conventional photodynamic therapy to improve treatment efficacy: An in vitro study. Lasers Surg Med. 2008;40:584-9.

[41] Bernardi RJ, Lowery AR, Thompson PA, Blaney SM, West JL. Immunonanoshells for targeted photothermal ablation in medulloblastoma and glioma. Proceedings of the American Association for Cancer Research Annual Meeting. 2007;48:537.
[42] Loo C, Lin A, Hirsch L, Lee MH, Barton J, Halas NJ, et al. Nanoshell-enabled photonics-based imaging and therapy of cancer. Technology in Cancer Research & Treatment. 2004;3:33-40.
[43] Stern JM, Stanfield J, Lotan Y, Park S, Hsieh JT, Cadeddu JA. Efficacy of laser-activated gold nanoshells in ablating prostate cancer cells in Vitro. Journal of Endourology. 2007;21:939-43.
[44] Fu K, Sun J, Bickford LR, Lin AWH, Halas NJ, Yu TK, et al. Measurement of immunotargeted plasmonic nanoparticles' cellular binding: a key factor in optimizing diagnostic efficacy. Nanotechnology. 2008;19.
[45] Elliott A, Schwartz J, Wang J, Shetty A, Hazle J, Stafford JR. Analytical Solution to Heat Equation With Magnetic Resonance Experimental Verification for Nanoshell Enhanced Thermal Therapy. Lasers Surg Med. 2008;40:660-5.
[46] Liu CH, Mi CC, Li BQ. Transient Temperature Response of Pulsed-Laser-Induced Heating for Nanoshell-Based Hyperthermia Treatment. Ieee Transactions on Nanotechnology. 2009;8:697-706.
[47] Vanagas T, Gulbinas A, Pundzius J, Barauskas G. Radiofrequency ablation of liver tumors (I): biological background. Med Lith. 2010;46:13-7.
[48] Fajardo LF, Egbert B, Marmor J, Hahn GM. EFFECTS OF HYPERTHERMIA IN A MALIGNANT-TUMOR. Cancer. 1980;45:613-23.
[49] Nikfarjam M, Muralidharan V, Christophi C. Mechanisms of focal heat destruction of liver tumors. J Surg Res. 2005;127:208-23.
[50] Lepock JR. INVOLVEMENT OF MEMBRANES IN CELLULAR-RESPONSES TO HYPERTHERMIA. Radiat Res. 1982;92:433-8.
[51] Roti JLR. Cellular responses to hyperthermia (40-46 degrees C): Cell killing and molecular events. Int J Hyperthermia. 2008;24:3-15.
[52] Defer N, Kitzis A, Kruh J, Brahms S, Brahms J. EFFECT OF NON-HISTONE PROTEINS ON THERMAL TRANSITION OF CHROMATIN AND OF DNA. Nucleic Acids Res. 1977;4:2293-306.
[53] Ohnishi T, Mori E, Takahashi A. DNA double-strand breaks: Their production, recognition, and repair in eukaryotes. Mutat Res-Fundam Mol Mech Mutagen. 2009;669:8-12.
[54] Roti JLR, Pandita RK, Mueller JD, Novak P, Moros EG, Laszlo A. Severe, short-duration (0-3 min) heat shocks (50-52 degrees C) inhibit the repair of DNA damage. Int J Hyperthermia. 2010;26:67-78.
[55] Takahashi A, Matsumoto H, Nagayama K, Kitano M, Hirose S, Tanaka H, et al. Evidence for the involvement of double-strand breaks in heat-induced cell killing. Cancer Research. 2004;64:8839-45.
[56] Melcher A, Gough M, Todryk S, Vile R. Apoptosis or necrosis for tumor immunotherapy: what's in a name? Journal of Molecular Medicine-Jmm. 1999;77:824-33.
[57] Garg AD, Nowis D, Golab J, Vandenabeele P, Krysko DV, Agostinis P. Immunogenic cell death, DAMPs and anticancer therapeutics: An emerging amalgamation. Biochim Biophys Acta-Rev Cancer. 2010;1805:53-71.
[58] Harmon BV, Corder AM, Collins RJ, Gobe GC, Allen J, Allan DJ, et al. CELL-DEATH INDUCED IN A MURINE MASTOCYTOMA BY 42-47-DEGREES-C HEATING INVITRO - EVIDENCE THAT THE FORM OF DEATH CHANGES FROM APOPTOSIS TO NECROSIS ABOVE A CRITICAL HEAT LOAD. Int J Radiat Biol. 1990;58:845-58.
[59] O'Neill KL, Fairbairn DW, Smith MJ, Poe BS. Critical parameters influencing hyperthermia-induced apoptosis in human lymphoid cell lines. Apoptosis. 1998;3:369-75.

[60] Gong JP, Traganos F, Darzynkiewicz Z. A SELECTIVE PROCEDURE FOR DNA EXTRACTION FROM APOPTOTIC CELLS APPLICABLE FOR GEL-ELECTROPHORESIS AND FLOW-CYTOMETRY. Anal Biochem. 1994;218:314-9.
[61] Schmid I, Krall WJ, Uittenbogaart CH, Braun J, Giorgi JV. DEAD CELL DISCRIMINATION WITH 7-AMINO-ACTINOMYCIN-D IN COMBINATION WITH DUAL COLOR IMMUNOFLUORESCENCE IN SINGLE LASER FLOW-CYTOMETRY. Cytometry. 1992;13:204-8.
[62] Vermes I, Haanen C, Steffensnakken H, Reutelingsperger C. A NOVEL ASSAY FOR APOPTOSIS - FLOW CYTOMETRIC DETECTION OF PHOSPHATIDYLSERINE EXPRESSION ON EARLY APOPTOTIC CELLS USING FLUORESCEIN-LABELED ANNEXIN-V. Journal of Immunological Methods. 1995;184:39-51.
[63] Rossriveros P, Leith JT. RESPONSE OF 9L TUMOR-CELLS TO HYPERTHERMIA AND X-IRRADIATION. Radiation Research. 1979;78:296-311.
[64] Bussolati O, Belletti S, Uggeri J, Gatti R, Orlandini G, Dallasta V, et al. CHARACTERIZATION OF APOPTOTIC PHENOMENA INDUCED BY TREATMENT WITH L-ASPARAGINASE IN NIH3T3 CELLS. Exp Cell Res. 1995;220:283-91.
[65] Kampinga HH, Laszlo A. DNA double strand breaks do not play a role in heat-induced cell killing. Cancer Research. 2005;65:10632-3.
[66] Wu W, Zhang C, Chen ZH, Zhang GL, Yang J. Differences in heating methods may account for variation in reported effects on gamma H2AX focus formation. Mutat Res Genet Toxicol Environ Mutagen. 2009;676:48-53.
[67] Prokop A, Davidson JM. Nanovehicular intracellular delivery systems. J Pharm Sci. 2008;97:3518-90.
[68] Kah JCY, Olivo M, Chow TH, Song KS, Koh KZY, Mhaisalkar S, et al. Control of optical contrast using gold nanoshells for optical coherence tomography imaging of mouse xenograft tumor model in vivo. Journal of Biomedical Optics. 2009;14.
[69] Terentyuk GS, Maslyakova GN, Suleymanova LV, Khlebtsov NG, Khlebtsov BN, Akchurin GG, et al. Laser-induced tissue hyperthermia mediated by gold nanoparticles: toward cancer phototherapy. Journal of Biomedical Optics. 2009;14:9.
[70] Huff TB, Tong L, Zhao Y, Hansen MN, Cheng JX, Wei A. Hyperthermic effects of gold nanorods on tumor cells. Nanomedicine. 2007;2:125-32.
[71] Chen JY, Wang DL, Xi JF, Au L, Siekkinen A, Warsen A, et al. Immuno gold nanocages with tailored optical properties for targeted photothermal destruction of cancer cells. Nano Letters. 2007;7:1318-22.
[72] Baffou G, Quidant R, Girard C. Heat generation in plasmonic nanostructures: Influence of morphology. Applied Physics Letters. 2009;94:3.
[73] Pilot Study of AuroLase(tm) Therapy in Refractory and/or Recurrent Tumors of the Head and Neck. 2011.
[74] Kennedy LC, Bickford LR, Lewinski NA, Coughlin AJ, Hu Y, Day ES, et al. A New Era for Cancer Treatment: Gold-Nanoparticle-Mediated Thermal Therapies. Small. 2011;7:169-83.
[75] Harmon BV, Corder AM, Collins RJ, Gobe GC, Allen J, Allan DJ, et al. Cell death induced in a murine mastocytoma by 42-47 degrees C heating in vitro: evidence that the form of death changes from apoptosis to necrosis above a critical heat load. Int J Radiat Biol. 1990;58:845-58.
[76] Yonezawa M, Otsuka T, Matsui N, Tsuji H, Kato KH, Moriyama A, et al. Hyperthermia induces apoptosis in malignant fibrous histiocytoma cells in vitro. International Journal of Cancer. 1996;66:347-51.

[77] Kono H, Rock KL. How dying cells alert the immune system to danger. Nature Reviews Immunology. 2008;8:279-89.
[78] Lepock JR. Involvement of membranes in cellular responses to hyperthermia. Radiat Res. 1982;92:433-8.
[79] Lepock JR. Cellular effects of hyperthermia: relevance to the minimum dose for thermal damage. Int J Hyperthermia. 2003;19:252-66.
[80] He XM, Wolkers WF, Crowe JH, Swanlund DJ, Bischof JC. In situ thermal denaturation of proteins in dunning AT-1 prostate cancer cells: Implication for hyperthermic cell injury. Ann Biomed Eng. 2004;32:1384-98.
[81] Bischof JC, He XM. Thermal stability of proteins. AnnNY AcadSci. 2005;1066:12-33.
[82] McCabe KM, Hernandez M. Molecular Thermometry. Pediatr Res. 2010;67:469-75.
[83] Hurwitz E, Stancovski I, Sela M, Yarden Y. Suppression and promotion of tumor growth by monoclonal-antibodies to ERBB-2 differentially correlate with cellular uptake. Proceedings of the National Academy of Sciences of the United States of America. 1995;92:3353-7.
[84] Liu SY, Liang ZS, Gao F, Luo SF, Lu GQ. In vitro photothermal study of gold nanoshells functionalized with small targeting peptides to liver cancer cells. Journal of Materials Science-Materials in Medicine. 2010;21:665-74.
[85] Huang XH, Kang B, Qian W, Mackey MA, Chen PC, Oyelere AK, et al. Comparative study of photothermolysis of cancer cells with nuclear-targeted or cytoplasm-targeted gold nanospheres: continuous wave or pulsed lasers. Journal of Biomedical Optics. 2010;15.
[86] Rabin Y. Is intracellular hyperthermia superior to extracellular hyperthermia in the thermal sense? Int J Hyperthermia. 2002;18:194-202.
[87] Letfullin RR, Iversen CB, George TF. Modeling nanophotothermal therapy: kinetics of thermal ablation of healthy and cancerous cell organelles and gold nanoparticles. Nanomedicine-Nanotechnology Biology and Medicine. 2011;7:137-45.
[88] Liu CH, Mi CC, Li BQ. Energy absorption of gold nanoshells in hyperthermia therapy. IEEE Trans Nanobiosci. 2008;7:206-14.
[89] Pitsillides CM, Joe EK, Wei XB, Anderson RR, Lin CP. Selective cell targeting with light-absorbing microparticles and nanoparticles. Biophysical Journal. 2003;84:4023-32.
[90] Pustovalov VK. Theoretical study of heating of spherical nanoparticle in media by short laser pulses. Chem Phys. 2005;308:103-8.
[91] Sassaroli E, Li KCP, O'Neill BE. Numerical investigation of heating of a gold nanoparticle and the surrounding microenvironment by nanosecond laser pulses for nanomedicine applications. Phys Med Biol. 2009;54:5541-60.
[92] Oldenburg SJ, Jackson JB, Westcott SL, Halas NJ. Infrared extinction properties of gold nanoshells. Applied Physics Letters. 1999;75:2897-9.
[93] Bohren CF, Huffman DR. Absorption and scattering of light by small particles. New York: Wiley; 1983.
[94] Buonanno G, Carotenuto A. The effective thermal conductivity of packed beds of spheres for a finite contact area. Numerical Heat Transfer Part a-Applications. 2000;37:343-57.
[95] Polesek-Karczewska S. Effective thermal conductivity of packed beds of spheres in transient heat transfer. Heat and Mass Transfer. 2003;39:375-80.
[96] Cheong SK, Krishnan S, Cho SH. Modeling of plasmonic heating from individual gold nanoshells for near-infrared laser-induced thermal therapy. Med Phys. 2009;36:4664-71.
[97] Longo DL. Harrison's Hematology and Oncology. 1 ed. United States: McGraw-Hill; 2010.
[98] Day ES, Thompson PA, Zhang LN, Lewinski NA, Ahmed N, Drezek RA, et al. Nanoshell-mediated photothermal therapy improves survival in a murine glioma model. Journal of Neuro-Oncology. 2011;104:55-63.

[99] Li ML, Wang JC, Schwartz JA, Gill-Sharp KL, Stoica G, Wang LHV. In-vivo photoacoustic microscopy of nanoshell extravasation from solid tumor vasculature. Journal of Biomedical Optics. 2009;14:3.
[100] Chen Y, Munteanu AC, Huang YF, Phillips J, Zhu Z, Mavros M, et al. Mapping Receptor Density on Live Cells by Using Fluorescence Correlation Spectroscopy. Chem-Eur J. 2009;15:5327-36.
[101] Tong L, Zhao Y, Huff TB, Hansen MN, Wei A, Cheng JX. Gold nanorods mediate tumor cell death by compromising membrane integrity. Advanced Materials. 2007;19:3136-41.
[102] VanderWaal R, Malyapa RS, Higashikubo R, Roti JLR. A comparison of the modes and kinetics of heat-induced cell killing in HeLa and L5178Y cells. Radiat Res. 1997;148:455-62.
[103] Zhang HG, Mehta K, Cohen P, Guha C. Hyperthermia on immune regulation: A temperature's story. Cancer Letters. 2008;271:191-204.
[104] Giuliano JS, Lahni PM, Wong HR, Wheeler DS. Extracellular Heat Shock Proteins: Alarmins for the Host Immune System. The Open Inflammation Journal. 2011;4:49-60.
[105] Rylander MN, Feng Y, Bass J, Diller KR. Heat shock protein expression and injury optimization for laser therapy design. Lasers Surg Med. 2007;39:731-46.
[106] Basu S, Binder RJ, Suto R, Anderson KM, Srivastava PK. Necrotic but not apoptotic cell death releases heat shock proteins, which deliver a partial maturation signal to dendritic cells and activate the NF-kappa B pathway. International Immunology. 2000;12:1539-46.
[107] Brusa D, Migliore E, Garetto S, Simone M, Matera L. Immunogenicity of 56 degrees C and UVC-Treated Prostate Cancer Is Associated With Release of HSP70 and HMGBI From Necrotic Cells. Prostate. 2009;69:1343-52.
[108] Hilger I, Rapp A, Greulich KO, Kaiser WA. Assessment of DNA damage in target tumor cells after thermoablation in mice. Radiology. 2005;237:500-6.
[109] Sperling RA, Gil PR, Zhang F, Zanella M, Parak WJ. Biological applications of gold nanoparticles. Chemical Society Reviews. 2008;37:1896-908.
[110] Apetoh L, Ghiringhelli F, Tesniere A, Criollo A, Ortiz C, Lidereau R, et al. The interaction between HMGB1 and TLR4 dictates the outcome of anticancer chemotherapy and radiotherapy. Immunological Reviews. 2007;220:47-59.
[111] Rouhiainen A, Tumova S, Valmu L, Kalkkinen N, Rauvala H. Pivotal advance: Analysis of proinflammatory activity of highly purified eukaryotic recombinant HMGB1 (amphoterin). J Leukoc Biol. 2007;81:49-58.
[112] Jiang DH, Liang JR, Fan J, Yu S, Chen SP, Luo Y, et al. Regulation of lung injury and repair by Toll-like receptors and hyaluronan. Nature Medicine. 2005;11:1173-9.
[113] Babelova A, Moreth K, Tsalastra-Greul W, Zeng-Brouwers J, Eickelberg O, Young MF, et al. Biglycan, a Danger Signal That Activates the NLRP3 Inflammasome via Toll-like and P2X Receptors. Journal of Biological Chemistry. 2009;284:24035-48.
[114] Schaefer L, Babelova A, Kiss E, Hausser HJ, Baliova M, Krzyzankova M, et al. The matrix component biglycan is proinflammatory and signals through Toll-like receptors 4 and 2 in macrophages. Journal of Clinical Investigation. 2005;115:2223-33.
[115] Kol A, Lichtman AH, Finberg RW, Libby P, Kurt-Jones EA. Cutting edge: Heat shock protein (HSP) 60 activates the innate immune response: CD14 is an essential receptor for HSP60 activation of mononuclear cells. Journal of Immunology. 2000;164:13-7.
[116] Quintana FJ, Cohen IR. Heat shock proteins as endogenous adjuvants in sterile and septic inflammation. Journal of Immunology. 2005;175:2777-82.
[117] Schroder K, Tschopp J. The Inflammasomes. Cell. 2010;140:821-32.

[118] Imaeda AB, Watanabe A, Sohail MA, Mahmood S, Mohamadnejad M, Sutterwala FS, et al. Acetaminophen-induced hepatotoxicity in mice is dependent on Tlr9 and the Nalp3 inflammasome. Journal of Clinical Investigation. 2009;119:305-14.
[119] Latz E. The inflammasomes: mechanisms of activation and function. Curr Opin Immunol. 2010;22:28-33.
[120] Aymeric L, Apetoh L, Ghiringhelli F, Tesniere A, Martins I, Kroemer G, et al. Tumor Cell Death and ATP Release Prime Dendritic Cells and Efficient Anticancer Immunity. Cancer Research. 2010;70:855-8.
[121] Ferrari D, Chiozzi P, Falzoni S, DalSusino M, Melchiorri L, Baricordi OR, et al. Extracellular ATP triggers IL-1 beta release by activating the purinergic P2Z receptor of human macrophages. Journal of Immunology. 1997;159:1451-8.
[122] Chakfe Y, Seguin R, Antel JP, Morissette C, Malo D, Henderson D, et al. ADP and AMP induce interleukin-1 beta release from microglial cells through activation of ATP-primed P2X(7) receptor channels. Journal of Neuroscience. 2002;22:3061-9.
[123] Shi Y. Caught red-handed: uric acid is an agent of inflammation. Journal of Clinical Investigation. 2010;120:1809-11.
[124] Martinon F, Petrilli V, Mayor A, Tardivel A, Tschopp J. Gout-associated uric acid crystals activate the NALP3 inflammasome. Nature. 2006;440:237-41.
[125] Shi Y, Evans JE, Rock KL. Molecular identification of a danger signal that alerts the immune system to dying cells. Nature. 2003;425:516-21.
[126] Martinon F. Mechanisms of uric acid crystal-mediated autoinflammation. Immunological Reviews. 2010;233:218-32.
[127] Franchi L, Eigenbrod T, Munoz-Planillo R, Nunez G. The inflammasome: a caspase-1-activation platform that regulates immune responses and disease pathogenesis. Nature Immunology. 2009;10:241-7.
[128] Gabay C, Lamacchia C, Palmer G. IL-1 pathways in inflammation and human diseases. Nature Reviews Rheumatology. 2010;6:232-41.
[129] McDonald B, Pittman K, Menezes GB, Hirota SA, Slaba I, Waterhouse CCM, et al. Intravascular Danger Signals Guide Neutrophils to Sites of Sterile Inflammation. Science. 2010;330:362-6.
[130] Ghiringhelli F, Apetoh L, Tesniere A, Aymeric L, Ma YT, Ortiz C, et al. Activation of the NLRP3 inflammasome in dendritic cells induces IL-1 beta-dependent adaptive immunity against tumors. Nature Medicine. 2009;15:1170-9.
[131] Acosta-Rodriguez EV, Napolitani G, Lanzavecchia A, Sallusto F. Interleukins 1 beta and 6 but not transforming growth factor-beta are essential for the differentiation of interleukin 17-producing human T helper cells. Nature Immunology. 2007;8:942-9.
[132] Dinarello CA. Biologic basis for interleukin-1 in disease. Blood. 1996;87:2095-147.
[133] Bartholomae WC, Rininsland FH, Eisenberg JC, Boehm BO, Lehmann PV, Tary-Lehmann M. T cell immunity induced by live, necrotic, and apoptotic tumor cells. Journal of Immunology. 2004;173:1012-22.
[134] van der Most RG, Currie AJ, Robinson BWS, Lake RA. Decoding dangerous death: how cytotoxic chemotherapy invokes inflammation, immunity or nothing at all. Cell Death Differ. 2008;15:13-20.
[135] Gasse P, Riteau N, Charron S, Girre S, Fick L, Petrilli V, et al. Uric Acid Is a Danger Signal Activating NALP3 Inflammasome in Lung Injury Inflammation and Fibrosis. American Journal of Respiratory and Critical Care Medicine. 2009;179:903-13.
[136] Perregaux D, Gabel CA. Interleukin-1-Beta Maturation and Release in Response to ATP and Nigericin - Evidence that Potassium-Depletion Mediated by These Agents is a Necessary and Common Feature of Their Activity. Journal of Biological Chemistry. 1994;269:15195-203.

[137] Nour AM, Yeung YG, Santambrogio L, Boyden ED, Stanley ER, Brojatsch J. Anthrax Lethal Toxin Triggers the Formation of a Membrane-Associated Inflammasome Complex in Murine Macrophages. Infection and Immunity. 2009;77:1262-71.
[138] Thomas LM, Salter RD. Activation of Macrophages by P2X(7)-Induced Microvesicles from Myeloid Cells Is Mediated by Phospholipids and Is Partially Dependent on TLR4. Journal of Immunology. 2010;185:3740-9.
[139] Ferrari D, Pizzirani C, Adinolfi E, Lemoli RM, Curti A, Idzko M, et al. The P2X(7) receptor: A key player in IL-1 processing and release. Journal of Immunology. 2006;176:3877-83.
[140] Bours MJL, Swennen ELR, Di Virgilio F, Cronstein BN, Dagnelie PC. Adenosine 5 '-triphosphate and adenosine as endogenous signaling molecules in immunity and inflammation. Pharmacology & Therapeutics. 2006;112:358-404.
[141] Schildkopf P, Frey B, Mantel F, Ott OJ, Weiss EM, Sieber R, et al. Application of hyperthermia in addition to ionizing irradiation fosters necrotic cell death and HMGB1 release of colorectal tumor cells. Biochemical and Biophysical Research Communications. 2010;391:1014-20.
[142] Rovere-Querini P, Capobianco A, Scaffidi P, Valentinis B, Catalanotti F, Giazzon M, et al. HMGB1 is an endogenous immune adjuvant released by necrotic cells. Embo Reports. 2004;5:825-30.
[143] Ghanem G, Loir B, Morandini R, Sales F, Lienard D, Eggermont A, et al. On the release and half-life of S100B protein in the peripheral blood of melanoma patients. International Journal of Cancer. 2001;94:586-90.
[144] Ellis EF, Willoughby KA, Sparks SA, Chen T. S100B protein is released from rat neonatal neurons, astrocytes, and microglia by in vitro trauma and anti-S100 increases trauma-induced delayed neuronal injury and negates the protective effect of exogenous S100B on neurons. Journal of Neurochemistry. 2007;101:1463-70.
[145] Ishii KJ, Suzuki K, Coban C, Takeshita F, Itoh Y, Matoba H, et al. Genomic DNA released by dying cells induces the maturation of APCs. Journal of Immunology. 2001;167:2602-7.
[146] Cavassani KA, Ishii M, Wen H, Schaller MA, Lincoln PM, Lukacs NW, et al. TLR3 is an endogenous sensor of tissue necrosis during acute inflammatory events. Journal of Experimental Medicine. 2008;205:2609-21.
[147] Vanden Berghe T, Kalai M, Denecker G, Meeus A, Saelens X, Vandenabeele P. Necrosis is associated with IL-6 production but apoptosis is not. Cellular Signalling. 2006;18:328-35.
[148] Chen TY, Guo J, Han CF, Yang MKJ, Cao XT. Heat Shock Protein 70, Released from Heat-Stressed Tumor Cells, Initiates Antitumor Immunity by Inducing Tumor Cell Chemokine Production and Activating Dendritic Cells via TLR4 Pathway. Journal of Immunology. 2009;182:1449-59.
[149] Torigoe T, Tamura Y, Sato N. Heat shock proteins and immunity: Application of hyperthermia for immunomodulation. Int J Hyperthermia. 2009;25:610-6.
[150] Chen GY, Nunez G. Sterile inflammation: sensing and reacting to damage. Nature Reviews Immunology. 2010;10:826-37.
[151] Milani V, Noessner E, Ghose S, Kuppner M, Ahrens B, Scharner A, et al. Heat shock protein 70: role in antigen presentation, and immune stimulation. Int J Hyperthermia. 2002;18:563-75.
[152] Tsan MF, Gao B. Heat shock proteins and immune system. J Leukoc Biol. 2009;85:905-10.
[153] Peter C, Wesselborg S, Herrmann M, Lauber K. Dangerous attraction: phagocyte recruitment and danger signals of apoptotic and necrotic cells. Apoptosis. 2010;15:1007-28.

[154] Ito A, Honda H, Kobayashi T. Cancer immunotherapy based on intracellular hyperthermia using magnetite nanoparticles: a novel concept of "heat-controlled necrosis" with heat shock protein expression. Cancer Immunology Immunotherapy. 2006;55:320-8.
[155] Liu G-J, Moriyasu F, Hirokawa T, Rexiati M, Yamada M, Imai Y. Expression of Heat Shock Protein 70 in Rabbit Liver After Contrast-Enhanced Ultrasound and Radiofrequency Ablation. Ultrasound in Medicine and Biology. 2010;36:78-85.
[156] Feng YS, Fuentes D, Hawkins A, Bass J, Rylander MN, Elliott A, et al. Nanoshell-mediated laser surgery simulation for prostate cancer treatment. Eng Comput. 2009;25:3-13.
[157] Knudsen S, Schardt A, Buhl T, Boeckmann L, Schon MP, Neumann C, et al. Enhanced T-cell activation by immature dendritic cells loaded with HSP70-expressing heat-killed melanoma cells. Experimental Dermatology. 2010;19:108-16.
[158] Liu K, Iyoda T, Saternus M, Kimura Y, Inaba K, Steinman RM. Immune tolerance after delivery of dying cells to dendritic cells in situ. Journal of Experimental Medicine. 2002;196:1091-7.
[159] Maeda H, Wu J, Sawa T, Matsumura Y, Hori K. Tumor vascular permeability and the EPR effect in macromolecular therapeutics: a review. Journal of Controlled Release. 2000;65:271-84.
[160] Iyer AK, Khaled G, Fang J, Maeda H. Exploiting the enhanced permeability and retention effect for tumor targeting. Drug Discovery Today. 2006;11:812-8.
[161] Senger DR, Galli SJ, Dvorak AM, Perruzzi CA, Harvey VS, Dvorak HF. Tumor cells secrete a vascular permeability factor that promotes accumulation of ascites fluid. Science. 1983;219:983-5.
[162] Padera TP, Kadambi A, di Tomaso E, Carreira CM, Brown EB, Boucher Y, et al. Lymphatic Metastasis in the Absence of Functional Intratumor Lymphatics. Science. 2002;296:1883-6.
[163] Jain RK. Transport of molecules in the tumor interstitium: A review. Cancer Research. 1987;47:3039-51.
[164] Danhier F, Feron O, Préat V. To exploit the tumor microenvironment: Passive and active tumor targeting of nanocarriers for anti-cancer drug delivery. Journal of Controlled Release. 2010;148:135-46.
[165] James WD, Hirsch LR, West JL, O'Neal PD, Payne JD. Application of INAA to the build-up and clearance of gold nanoshells in clinical studies in mice. Journal of Radioanalytical and Nuclear Chemistry. 2007;271:455-9.
[166] Park M, Lynch I, Ramirez-Garcia S, Dawson KA, de la Fonteyne L, Gremmer E, et al. In vitro evaluation of cytotoxic and inflammatory properties of silica nanoparticles of different sizes in murine RAW 264.7 macrophages. J Nanopart Res. 2011;13:6775-87.
[167] Erickson TA, Tunnell JW. Gold Nanoshells in Biomedical Applications. Nanotechnologies for the Life Sciences: Wiley-VCH Verlag GmbH & Co. KGaA; 2007.
[168] Dostert C, Petrilli V, Van Bruggen R, Steele C, Mossman BT, Tschopp J. Innate immune activation through Nalp3 inflammasome sensing of asbestos and silica. Science. 2008;320:674-7.
[169] Hornung V, Bauernfeind F, Halle A, Samstad EO, Kono H, Rock KL, et al. Silica crystals and aluminum salts activate the NALP3 inflammasome through phagosomal destabilization. Nature Immunology. 2008;9:847-56.
[170] Morishige T, Yoshioka Y, Inakura H, Tanabe A, Yao XL, Narimatsu S, et al. The effect of surface modification of amorphous silica particles on NLRP3 inflammasome mediated IL-1 beta production, ROS production and endosomal rupture. Biomaterials. 2010;31:6833-42.
[171] Nguyen HT, Tran KK, Sun B, Shen H. Activation of inflammasomes by tumor cell death mediated by gold nanoshells. Biomaterials. 2012;33:2197-205.

[172] Arnida, Malugin A, Ghandehari H. Cellular uptake and toxicity of gold nanoparticles in prostate cancer cells: a comparative study of rods and spheres. Journal of Applied Toxicology. 2010;30:212-7.
[173] Harris N, Ford MJ, Cortie MB. Optimization of plasmonic heating by gold nanospheres and nanoshells. Journal of Physical Chemistry B. 2006;110:10701-7.
[174] Lunov O, Syrovets T, Loos C, Nienhaus GU, Mailander V, Landfester K, et al. Amino-Functionalized Polystyrene Nanoparticles Activate the NLRP3 Inflammasome in Human Macrophages. Acs Nano. 2011;5:9648-57.
[175] Pilot Study of AuroLase(tm) Therapy in Refractory and/or Recurrent Tumors of the Head and Neck. 2011.
[176] O'Neill LAJ. Immunology - How frustration leads to inflammation. Science. 2008;320:619-20.
[177] Zhou R, Yazdi AS, Menu P, Tschopp J. A role for mitochondria in NLRP3 inflammasome activation. Nature. 2011;469:221-5.
[178] Schwank J. Catalytic gold. Gold Bulletin. 1983;16:103-10.
[179] Weiss J. THE FREE RADICAL MECHANISM IN THE REACTIONS OF HYDROGEN PEROXIDE. Advances in Catalysis. 1952;4:343-65.
[180] Ono Y, Matsumura T, Kitajima N, Fukuzumi S. FORMATION OF SUPEROXIDE ION DURING DECOMPOSITION OF HYDROGEN-PEROXIDE ON SUPPORTED METALS. Journal of Physical Chemistry. 1977;81:1307-11.
[181] McKee DW. CATALYTIC DECOMPOSITION OF HYDROGEN PEROXIDE BY METALS AND ALLOYS OF PLATINUM GROUP. J Catal. 1969;14:355-&.
[182] Thompson DT. Using gold nanoparticles for catalysis. Nano Today. 2007;2:40-3.
[183] Haruta M. When Gold Is Not Noble: Catalysis by Nanoparticles. The Chemical Record. 2003;3:75-87.
[184] Haruta M, Daté M. Advances in the catalysis of Au nanoparticles. Applied Catalysis A: General. 2001;222:427-37.
[185] Turkevich J. Colloidal gold. Part II. Gold Bulletin. 1985;18:125-31.
[186] Dey KK, Panda BR, Paul A, Basu S, Chattopadhyay A. Catalytic gold nanoparticle driven pH specific chemical locomotion. Journal of Colloid and Interface Science. 2010;348:335-41.
[187] Naya S-i, Teranishi M, Kimura K, Tada H. A strong support-effect on the catalytic activity of gold nanoparticles for hydrogen peroxide decomposition. Chemical Communications. 2011;47:3230-2.
[188] Kiyonaga T, Jin Q, Kobayashi H, Tada H. Size-Dependence of Catalytic Activity of Gold Nanoparticles Loaded on Titanium (IV) Dioxide for Hydrogen Peroxide Decomposition. ChemPhysChem. 2009;10:2935-8.
[189] Suh M, Bagus PS, Pak S, Rosynek MP, Lunsford JH. Reactions of hydroxyl radicals on titania, silica, alumina, and gold surfaces. Journal of Physical Chemistry B. 2000;104:2736-42.
[190] Moghimi SM, Szebeni J. Stealth liposomes and long circulating nanoparticles: critical issues in pharmacokinetics, opsonization and protein-binding properties. Prog Lipid Res. 2003;42:463-78.
[191] Storm G, Belliot SO, Daemen T, Lasic DD. SURFACE MODIFICATION OF NANOPARTICLES TO OPPOSE UPTAKE BY THE MONONUCLEAR PHAGOCYTE SYSTEM. Adv Drug Deliv Rev. 1995;17:31-48.
[192] Chen CJ, Kono H, Golenbock D, Reed G, Akira S, Rock KL. Identification of a key pathway required for the sterile inflammatory response triggered by dying cells. Nature Medicine. 2007;13:851-6.

I Appendix A

I.1 Synthesis of Gold Nanoshells with Varying Geometries

Based on Mie theory, nanoshell surface plasmon resonance can be tuned by variation of the core to shell ratio, as well as the overall size of the nanoshell itself. By varying the silica core size synthesized, nanoshells with varying core to shell ratios were obtained, with corresponding changes in the resonance peak. Silica particles were synthesized using a modified Stober method described in *Chapter 2*. By varying the ratio of NH_4OH while keeping TEOS and EtOH constant, the silica size can be varied.

In *Figure 31* below, the characterization of the nanoshell geometries synthesized is summarized. 8 gold nanoshell batches were produced which are labeled GNS1-8.

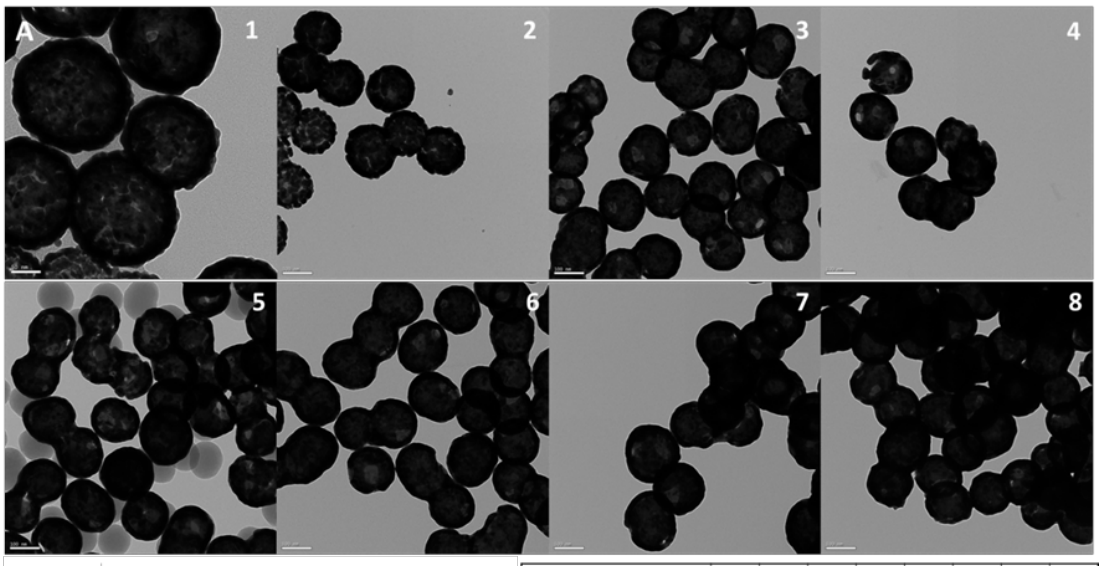

C

	GNS1	GNS2	GNS3	GNS4	GNS5	GNS6	GNS7	GNS8
Silica Diameter	124.2	124.2	119.3	123.6	117.4	120.6	134.9	120.6
Silica Std. Dev.	6.8	6.8	3.3	5.6	5.3	3.5	6.3	3.5
Nanoshell Diameter [nm]	169.0	170.7	159.7	160.9	164.7	159.8	166.5	156.6
Nanoshell Std. Dev.	12.9	8.0	12.8	9.2	14.3	9.7	15.8	7.0
Shell Thickness	22.4	23.3	20.2	18.7	23.7	19.6	15.8	18.0
Core:Shell Ratio	2.8	2.7	3.0	3.3	2.5	3.1	4.3	3.4
SPR Peak [nm]	820	750	810	930	850	790	940	820

Figure 31. Gold nanoshell synthesis of varying geometries. A) TEM images of complete nanoshell formation for 8 silica NP samples, corresponding to the GNS1-8 designation. GNS1 100,000X magnification, GNS2-8 50,000X magnification. B) Absorption spectra of GNS samples 1-8 in water. C) Size and geometry of GNS from TEM image measurements.

GNS1 consists of gold nanoshells synthesized and aged for over 1 year. GNS1 nanoshells were used in all experiments in previous sections, while all subsequent batches (GNS2-8)were used immediately after synthesis for the experiments in the following sections. In addition, gold nanoshells were synthesized with vary degrees of gold reduction on the surface until complete shell formation was obtained, utilizing the same silica nanoparticle cores as the GNS2 batch of nanoshells. *Figure 32* summarizes the characterization of the nanoparticles with varying degrees of gold. By varying the amount of colloidal gold coated silica particles added to a gold reducing solution, varying degrees of gold reduction were achieved while keeping the total amount of gold between the samples the same.

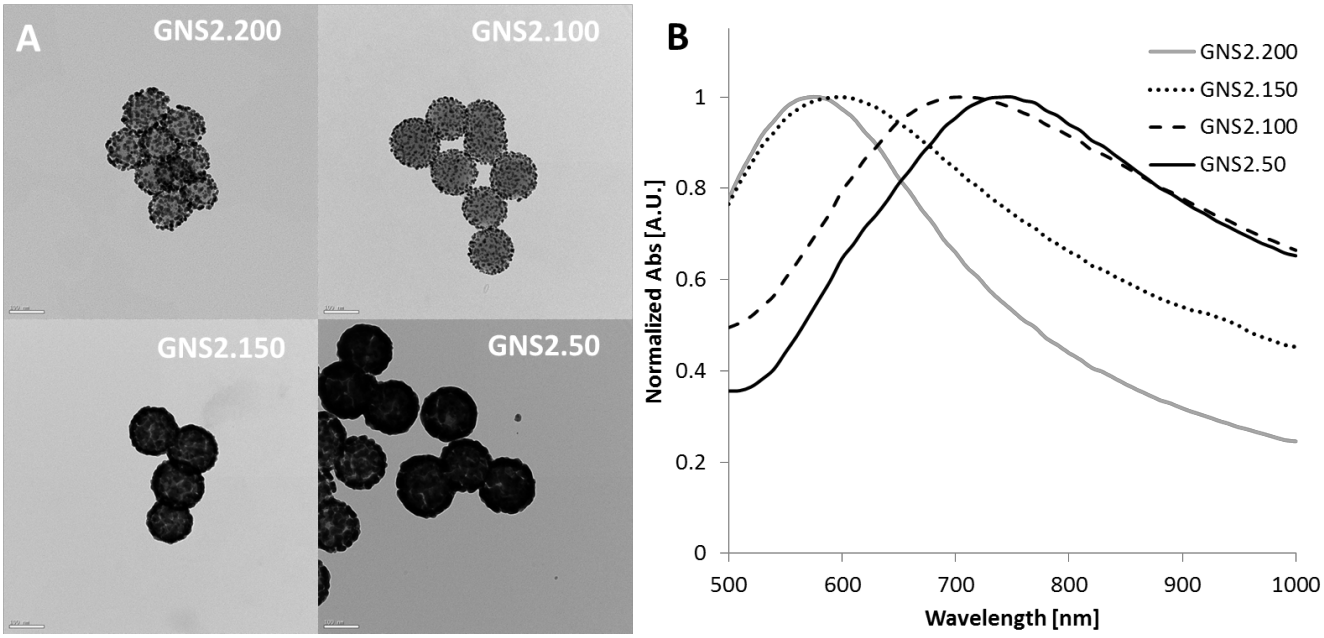

Figure 32. Gold nanoshell synthesis with varying degrees of gold reduction. Completed gold nanoshells were labeled GNS2. A) TEM images of nanoparticles with different amount of colloidal gold particles added to the gold reducing solution at 50,000X magnification. B) Normalized absorption spectra of samples in water.

I.2 Scavenger effect and fluorescent quenching of newly synthesized gold nanoshells

H_2O_2 scavenging was performed on aged and newly synthesized GNS using the procedure described in *Chapter 6*. Comparisons between aged gold nanoshells(GNS1) and freshly synthesized gold nanoshells showed a repeatedly observable difference in the interaction with the

fluorescent ROS detection system consisting of HRP and H_2DCF in PBS buffer. For control samples without H_2O_2 consisting of only buffer and newly synthesized gold nanoshells, supernatant aliquots obtained after centrifugation and removal of nanoshells, when combined with the HRP/H_2DCF detection solution, exhibited a higher background fluorescence than the controls without gold nanoshells, while aged gold nanoshells did not exhibit this increase in fluorescence(*Figure 33A,D*). The increase in background fluorescence is GNS concentration dependent as well (*Figure 33B*). Newly synthesized gold nanoshells with varying geometries also increase background fluorescence that appears to not be specifically related to plasmon resonance peaks and size (*Figure 33C*).

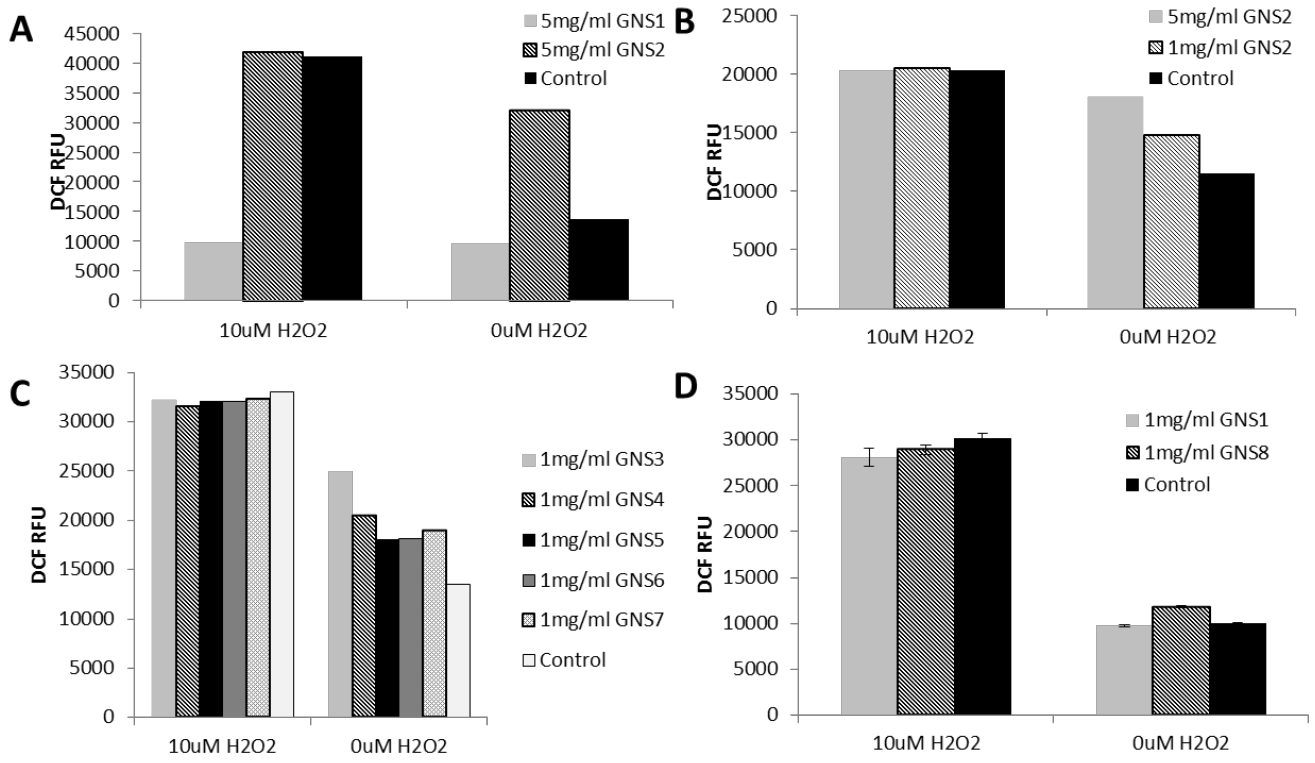

Figure 33. H_2O_2 scavenging effects of aged and newly synthesized GNS. Nanoshells are incubated with H_2O_2 solutions of varying concentrations for 15 mins prior to centrifugation and removal of the supernatant to assay for levels using the fluorescent ROS dye DCF. (A) Aged gold nanoshells(GNS1) compared to newly synthesized GNS2 (B) Concentration dependent scavenging by newly synthesized GNS2. (C) Scavenging by newly synthesized GNS3-7. (D) Aged gold nanoshells(GNS1) compared to newly synthesized GNS8.

The consistent results for the newly synthesize gold nanoshells indicates that some interaction with the buffer solution is occurring that can either increase the interaction with the HRP resulting in oxidation of the H_2DCF to DCF, or indirectly increase the fluorescent signal of the DCF. The exact mechanism of this interaction is not known, but it is thought to involve adsorption or desorption of ions in the PBS solution during incubation at 37^{o}C. The surface of gold nanoshells is covered in Cl^- and CO_3^{2-} ions in the gold reducing solution that come from the reduction of the $AuCl_4^-$ ion onto the gold shell, freeing the Cl^- ions, or from the dissociation of the K_2CO_3 added as a buffer. During aging of the nanoshells, atmospheric CO_2 can dissolve in the aqueous solution and form carbonic acid which may lead to the desorption of carbonate ions from the surface of the nanoshells that will buffer the solution. A decrease in carbonate ions on the surface of the particles can allow for the adsorption of ions found in the PBS buffer.

I.3 Effect of Buffer conditions on Background DCF Fluorescence

To explore the contribution of the buffer to the background signal, DPBS was compared to PBS for determination of buffer effects. DPBS does not contain calcium or magnesium ions. The overall fluorescence in both the samples containing H_2O_2 and controls is lower overall in DPBS, while the effect of newly synthesized GNS2 for both sample sets is similar(*Figure 34A*).

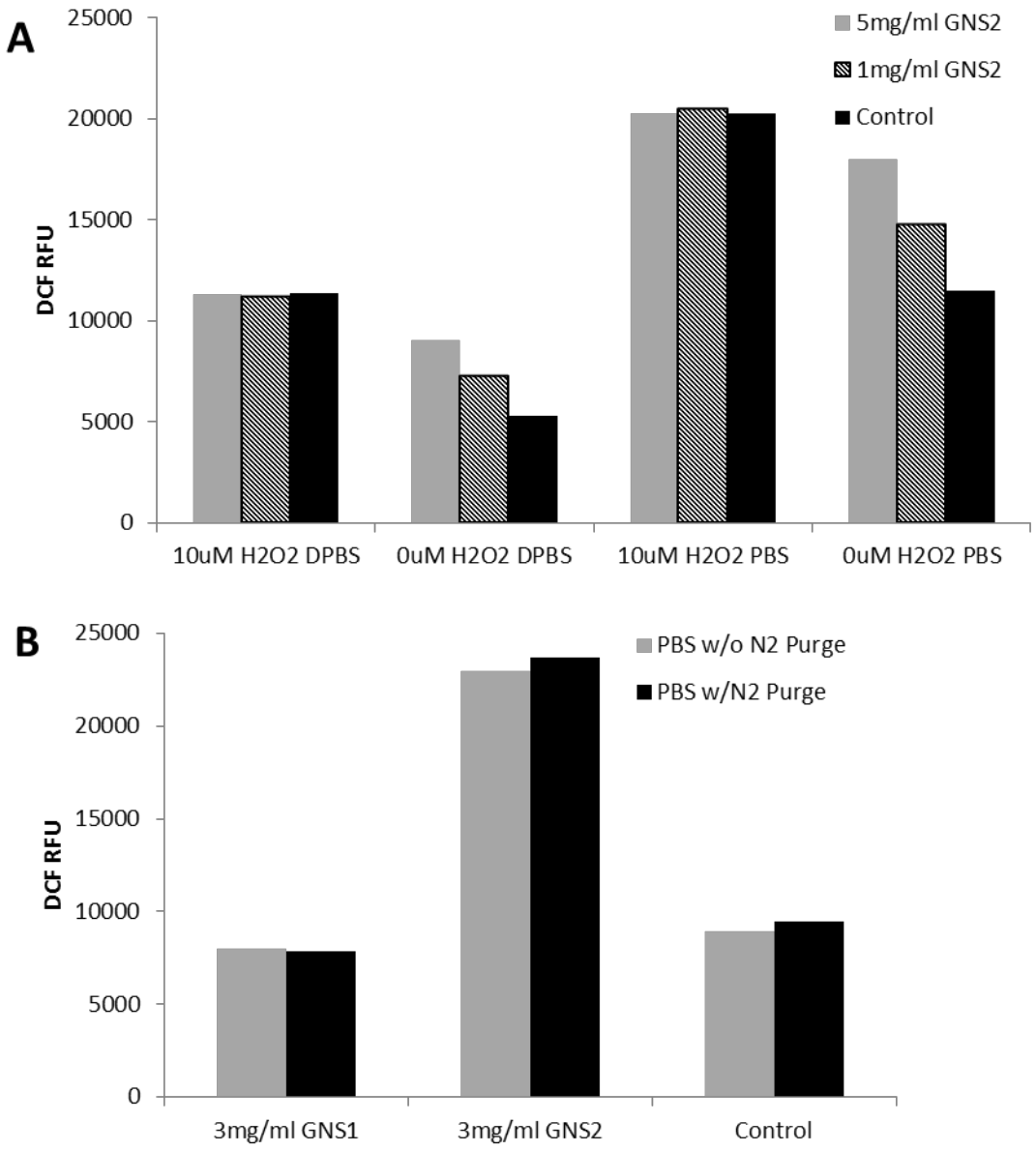

Figure 34. Buffer effects on DCF background signal. Nanoshells are incubated with H_2O_2 solutions of varying concentrations for 15 mins prior to centrifugation and removal of the supernatant to assay for levels using the fluorescent ROS dye DCF. (A) Nanoshells are dispersed in DPBS and PBS (B) PBS is purged for 15 mins with N_2 to remove residual oxygen prior to incubation.

Considering that the interaction of the newly synthesized gold nanoshells would occur in the samples containing hydrogen peroxide as well as the solutions only containing buffer, H2O2 scavenging by gold nanoshells would be masked by the increased background. To account for this, the scavenging data in *Figure 33* was replotted accounting for this by subtracting the corresponding background levels from the control samples incubated with nanoshells (*Figure 35*).

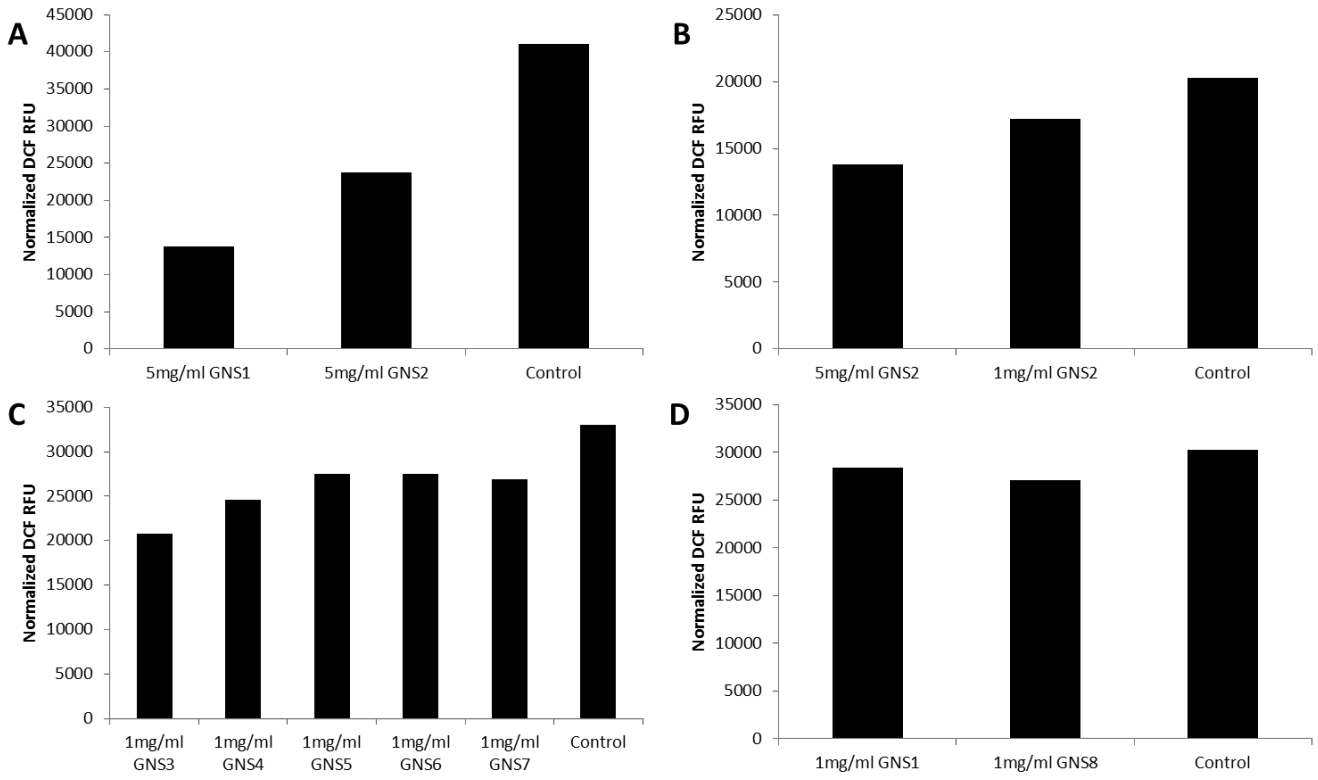

Figure 35. Normalized H_2O_2 scavenging effects of aged and newly synthesized GNS. Nanoshells are incubated with H_2O_2 solutions of varying concentrations for 15 mins prior to centrifugation and removal of the supernatant to assay for ROS levels using the fluorescent ROS dye DCF. Fluorescence is normalized to background controls without H_2O_2. (A) Aged gold nanoshells(GNS1) compared to newly synthesized GNS2 (B) Concentration dependent scavenging by newly synthesized GNS2. (C) Scavenging by newly synthesized GNS3-7. (D) Aged gold nanoshells(GNS1) compared to newly synthesized GNS8.

I.4 Quenching of DCF signal by gold nanoshells

The absorption spectra of the newly synthesized gold nanoshells still overlaps significantly with the emission spectra of the fluorescent DCF, which would lead to significant quenching of the signal (*Figure 36*).

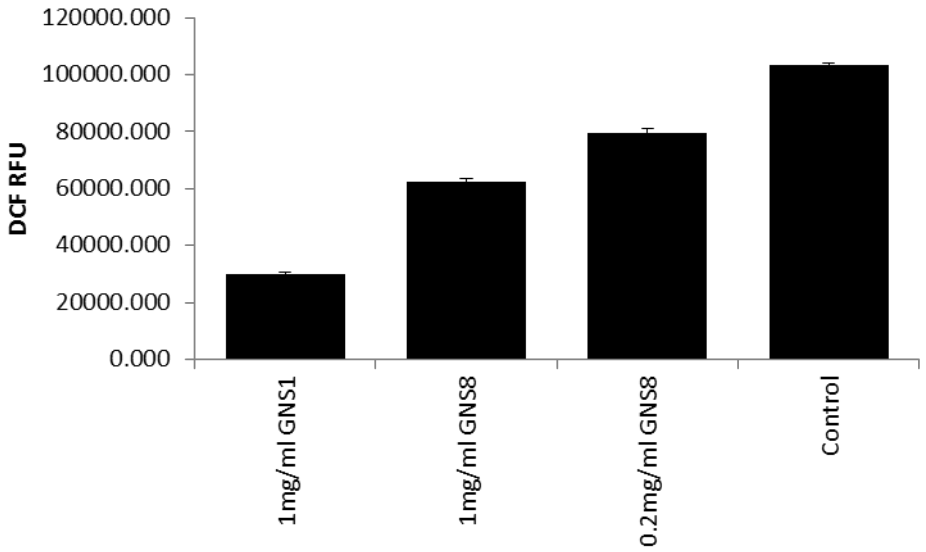

Figure 36. Fluorescent quenching effects of aged GNS1 and newly synthesized GNS8. H_2O_2 is reacted with DCF prior to nanoparticle addition and fluorescence at 536nm is measured. Values are mean ± S.D.

I.5 Comparison of Aged and Newly Synthesized GNS in inducing Inflammasome Activation

Newly synthesized gold nanoshells with the ability to activate inflammasome complexes in macrophages was assessed. LPS stimulated THP-1 cells were incubated for 4 hours with GNS1 and GNS8 particles prior to imaging. Gold nanoshell aggregation and association with macrophages differed greatly for the aged and newly synthesized nanoshells in terms of apparent quantity for the same mass concentration (*Figure 37*).

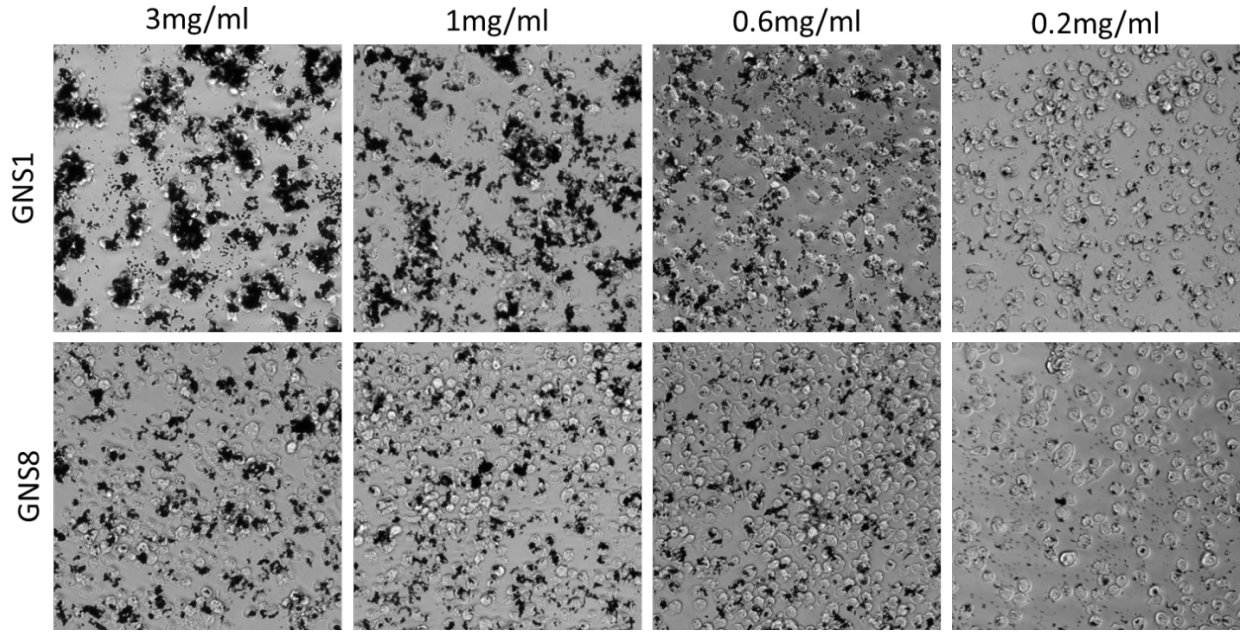

Figure 37. Cellular uptake of aged and newly synthesized GNS at different concentrations of particles. Light microscopy images of cells incubated with GNS1 and GNS8 ranging from 3.0 to 0.2mg/ml.

The ability of the newly synthesized gold nanoshells to generate intracellular ROS(*Figure 38*) and activate inflammasomes(*Figure 39*) is independent of ROS scavenging. Quenching of the fluorescent signal by the GNS may explain the low intracellular ROS generation by the newly synthesized GNS8.

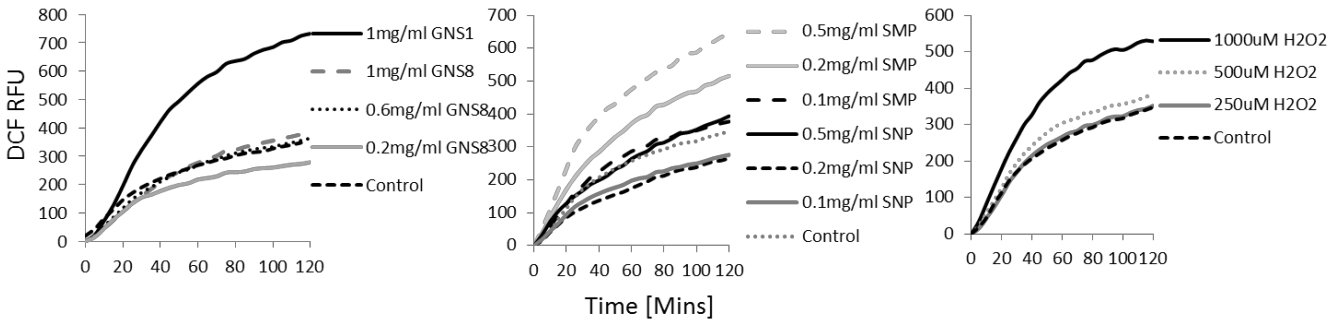

Figure 38. Intracellular ROS generation in THP-1 cells by aged and newly synthesized GNS. LPS-treated THP-1 macrophage cells were stimulated with nanoparticles at concentrations ranging from 1 mg/ml to 0.2mg/ml. Silica μP and extracellular H_2O_2 were used as a positive control, and untreated cells were used as a negative control (Control). ROS generation was monitored for a duration of 120 min with the ROS specific fluorescent probe DCF.

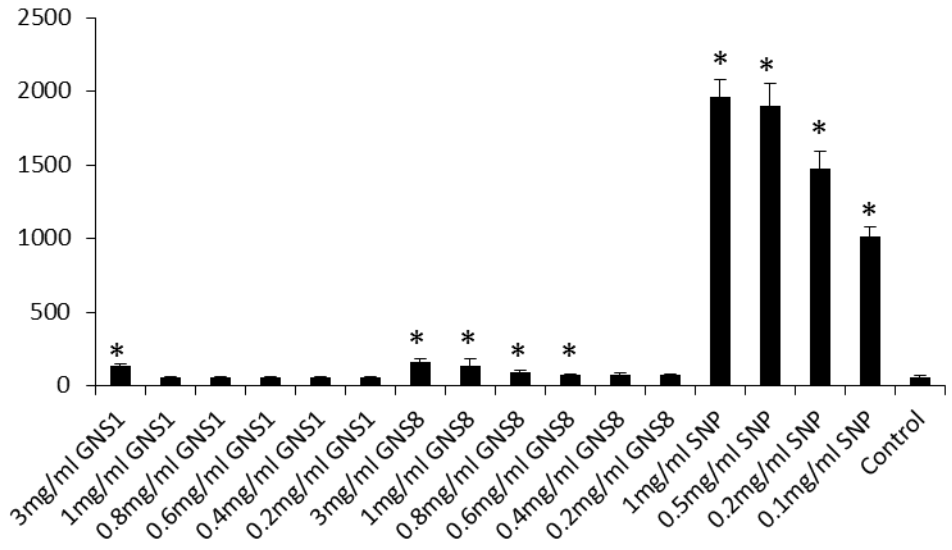

Figure 39. The stimulation of IL-1β production by aged and newly synthesized GNS. LPS-treated THP-1 macrophage cells were stimulated with nanoparticles at concentrations ranging from 3 mg/ml to 0.2mg/ml. Silica μP were used as a positive control, and untreated cells were used as a negative control (Control). IL-1β secreted by stimulated macrophages were collected after 24 h and quantified by ELISA. Values are mean ± S.D

Based on the cell microscopy images, the number of newly synthesized nanoshells that are interacting with the cells is lower than the aged nanoshells, however higher IL-1β levels are observed(*Figure 39*). This could be due to a number of reasons. The newly synthesized gold nanoshells may have a slightly different surface chemistry compared to the aged particles which may lead to higher macrophage stimulation and inflammasome activation. A decrease in ROS scavenging ability may also explain also explain an increased inflammasome activation response. The current observations and data indicate a significant difference in gold nanoshell properties between the aged and newly synthesized particles that we aren't able to characterize at this time.

I.6 Pegylation of nanoshells to limit surface interaction

It is clear that freshly synthesized gold nanoshells have a more reactive surface than aged nanoshell surfaces. Generally, pegylation of the surface is utilized to minimize interactions between the nanoparticle surface and its surroundings due to steric hindrance and water ordering at the PEG corona. In an attempt to minimize surface interactions of freshly synthesized gold

nanoshells, a number of pegylation parameters were employed to coat the nanoshell surface and are summarized below in *Table 5.*

	PEG-GNS1	PEG-GNS2	PEG-GNS3	PEG-GNS4	PEG-GNS5
PEG Concentration [uM]	5	0.5	5	20	50
PEG/GNS	36697	3670	36697	146787	366968
Excess PEG	67.5	6.7	67.5	269.8	674.6
Hydrodynamic Diameter [nm]	181.3	204.4	220.1	202.2	291.7
PDI	0.1	0.2	0.2	0.2	0.4
Zeta Potential[mV]	-4.8	-3.7	-5.6	-4.1	-7.0
Estimated PEG length [nm]	12.2	23.7	31.5	22.6	67.4

Table 5. PEG-GNS characterization. Gold nanoshells functionalized with varying concentrations of PEG. PEGylation was characterized by hydrodynamic diameter, PDI, and zeta potential using dynamic light scattering. Estimated PEG coverage was based on the flory radius determined for 5000MW PEG. Estimated PEG length was determined from comparison of hydrodynamic diameter to bare gold nanoshell diameter.

An increase in the hydrodynamic diameter and corresponding decrease in the zeta potential indicates that pegylation of the nanoshell surface occurred. Differences in hydrodynamic diameter and zeta potential could indicate a difference in the degree of pegylation on the surface, and the conformation of the PEG chains from a mushroom to a brush structure. The length would indicate a brush structure for all the PEG-GNS samples.

I.7 Effect of Pegylation on nanoshell uptake

Aged gold nanoshells showed a tendency to aggregate to a greater extent than freshly synthesized gold nanoshells(Figure 37), however pegylation also led to a decrease in aggregation(Figure 25). For freshly synthesized gold nanoshells, pegylation also decreased the extent of aggregation that occurs in media (Figure 40), but not to as significant of an extent as for the aged nanoshells. This would indicate that the surface is not fully protected from interaction with the media solution in the case of freshly synthesized gold nanoshells.

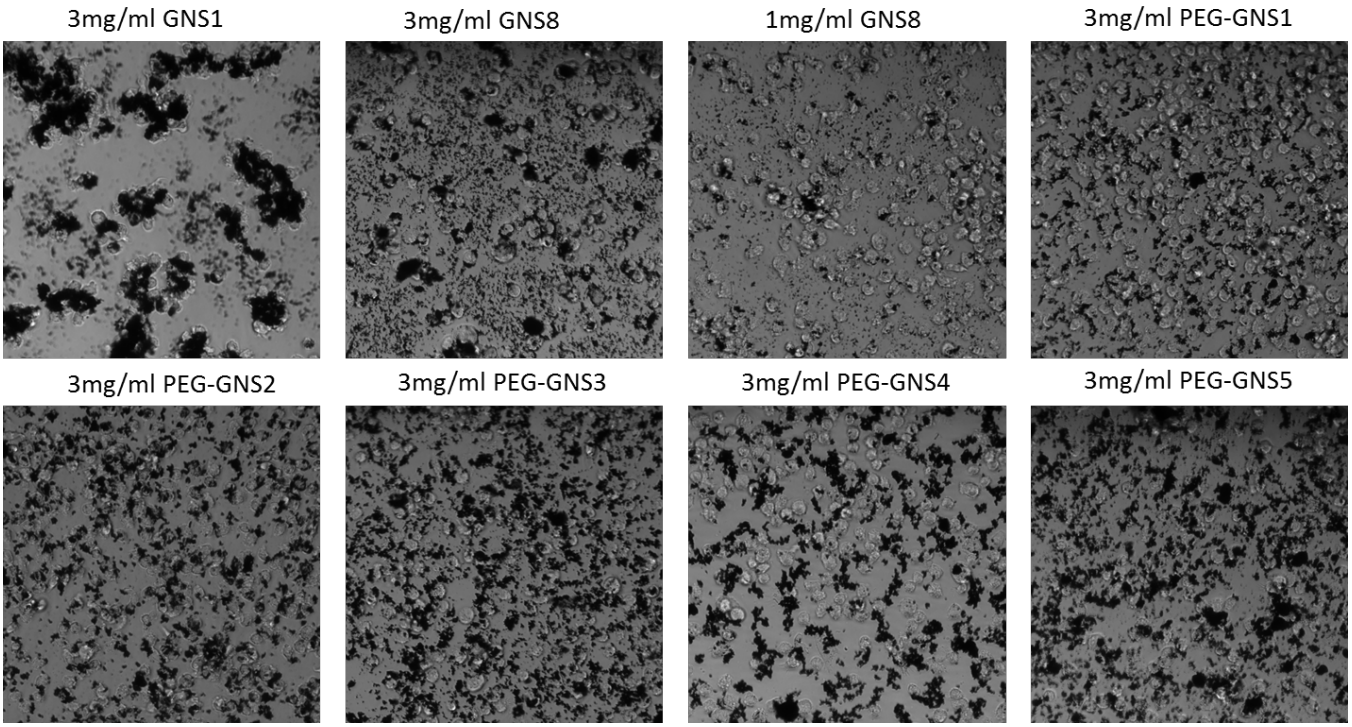

Figure 40. Cellular uptake of aged and newly synthesized GNS and pegylated GNS. Pegylation does not significantly decrease aggregation of th efreshly synthesized nanoshells.Light microscopy images of cells incubated with GNS1 and GNS8 ranging from 3.0 to 1.0mg/ml.

I.8 Comparison of Newly Synthesized PEG-GNS in Limiting Inflammasome Activation

Pegylation decreases nanoshell induced inflammasome activation by decreasing aggregation and uptake of the nanoshells in the case of aged nanoshells. For freshly synthesized gold nanoshells, the role of pegylation may extend beyond this, by also shielding the more reactive surface from interacting with the macrophage cells. As seen in *Figure 40*, the pegylated nanoshells do not appear to significantly decrease the amount of aggregated and settled nanoshells, but the macrophage cells do not cluster around the aggregated clusters the same way as the bare nanoshells. This would indicate potentially indicate a decrease in surface interaction due to the pegylation. Intracellular ROS production, a key indicator of inflammasome activation is again measured(*Figure 41*).

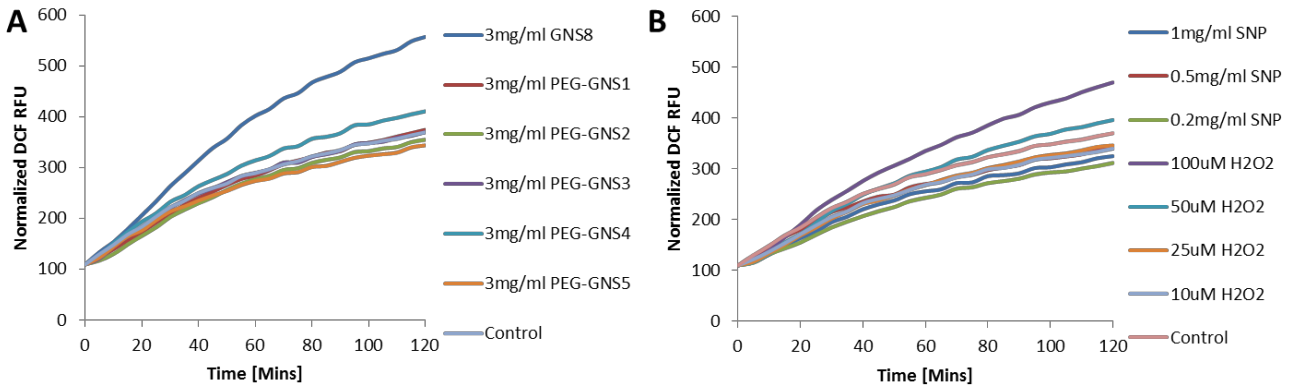

Figure 41. Intracellular ROS generation in THP-1 cells by newly synthesized GNS with varying degrees of pegylation. LPS-treated THP-1 macrophage cells were stimulated with nanoparticles at concentrations ranging from 1 mg/ml to 0.2mg/ml. Silica NP and extracellular H_2O_2 were used as a positive control, and untreated cells were used as a negative control (Control). ROS generation was monitored for a duration of 120 min with the ROS specific fluorescent probe DCF.

Secreted IL-1β was quantified for both the bare and pegylated nanoshells (*Figure 42*).

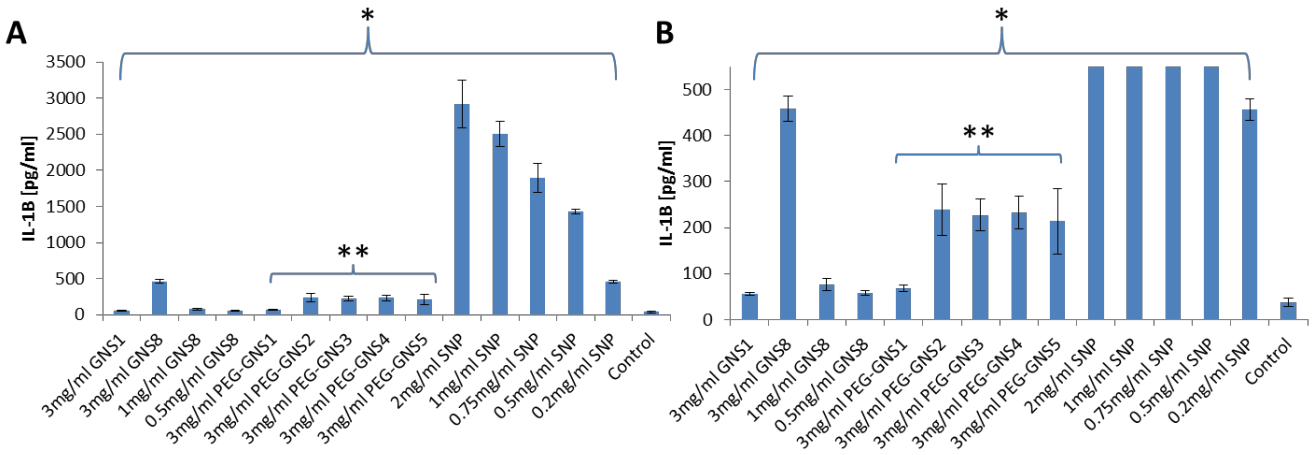

Figure 42. The stimulation of IL-1β production by freshly synthesized GNS, PEG-GNS, and silica NP. (A) LPS-treated THP-1 macrophage cells were stimulated with bare and pegylated GNS. Silica NP were used as a positive control, and untreated cells were used as a negative control (Control). IL-1β secreted by stimulated macrophages were collected after 24 h and quantified by ELISA. Values are mean ± S.D (*P < 0.05 versus value for media control, **P < 0.05 versus value for GNS8). (B) IL-1β levels replotted on smaller axis to show detail . Experiments are representative of three independent experiments.

Pegylation of the freshly synthesized gold nanoshells decreased the inflammasome activation significantly, but did not completely eliminate inflammasome activation as was the case for the aged GNS(Figure 26). One indicator that the pegylation is insufficient in preventing interaction at the nanoshells surface is inability to decrease the buffer solution interaction that occurs during nanoshell scavenging. The freshly synthesized GNS have some interaction with the PBS buffer

solution that causes the background DCF signal to increase. If pegylation of the nanoshell surface were to shield it from interaction with the solution, then the increase in background signal would not be present(*Figure 43*).

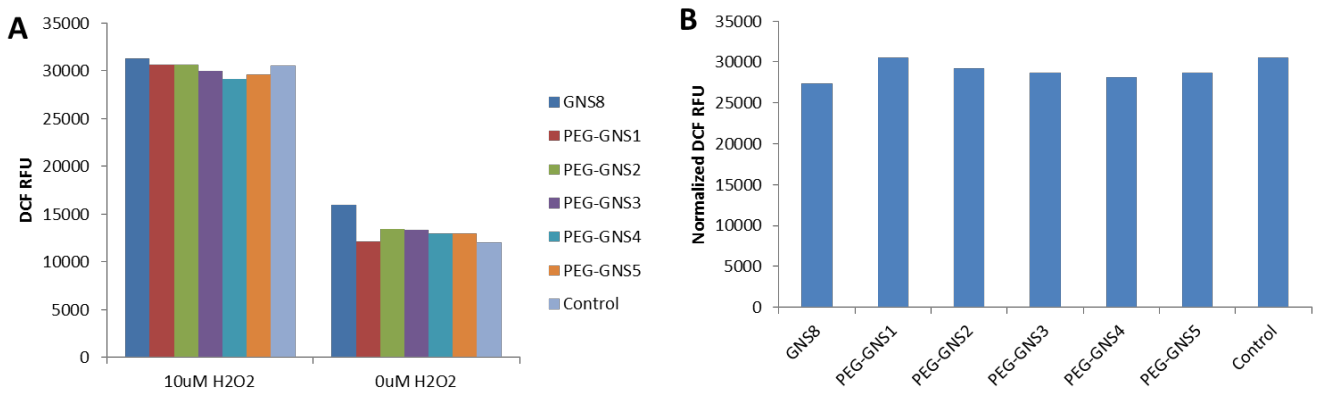

Figure 43. Scavenging effects of freshly synthesized GNS and PEG-GNS (B) Values are normalized to PBS samples without H2O2 containing nanoparticles.

While there is a decrease in the pegylated samples, it does not completely remove the nanoshell surface effects. Either insufficient surface coverage of PEG or a strong surface chemistry on the freshly synthesized still allows for some interaction to occur between the gold nanoshell surface and the surrounding solution. The consequences of this effect on freshly synthesized GNS is still not properly understood, and leaves open the possibility for addition exploration in the field on the minute differences between gold nanoshell surfaces and the storage implications for medical use.

VITA

Hai Nguyen was born in Portland, Oregon. He has lived in the Pacific Northwest his whole life and currently calls Seattle, Washington home. At Oregon State University he earned a Bachelor of Science degree in Chemical Engineering and a Master of Science degree from the University of Washington. In 2012 he earned a Doctor of Philosophy at the University of Washington in Chemical Engineering.